National Centre for Nuclear Research
Department of Nuclear Techniques and Equipment
Radiation Detectors Division

DISSERTATION

The comparative studies of neutron detectors in the crisis of ^{3}He supply

Joanna Iwanowska-Hanke

PhD thesis
completed in National Centre for Nuclear Research
under the supervision of
prof. Marek Moszynski and dr Lukasz Swiderski

Otwock 2015

Narodowe Centrum Badań Jądrowych
Departament Aparatury i Technik Jądrowych
Zakład Fizyki Detektorów

ROZPRAWA DOKTORSKA

Badania porównawcze detektorów neutronów w warunkach kryzysu z ^{3}He

Joanna Iwanowska-Hanke

Praca doktorska
wykonana w Narodowym Centrum Badań Jądrowych
pod kierunkiem
prof. Marka Moszyńskiego oraz dr Łukasza Świderskiego

Otwock 2015

dedicated to my beloved Grandmother

Acknowledgement

First of all I would like to thank professor Marek Moszynski for both scientific and personal support. For six years working in his group, I have got an incredible dose of trust and help. Professor always shares his experience with the whole group, giving young people the opportunity to gain so the necessary knowledge. I am very lucky having the opportunity to work with somebody who is the world expert in the field of scintillation detectors.

I would also like to thank my supervisor, dr Lukasz Swiderski, who has given me the basis of neutron detection from the first days I spent in the laboratory. His ideas and suggestions helped me in better understanding both nuclear physics and statistics. I would like also thank you for being not only a supervisor, but also a good friend.

Big thanks to the whole group from the Radiation Detectors Division (TJ3), and the Electronics and Detection Systems Division (TJ4). Special thanks goes to Pawel Sibczynski, who helped me in measurements during the times when I could not made them myself, as well as huge support in gaining contacts with French laboratory through the Polonium project. I am also indebted to Tomasz Szczesniak for his support in photomultipliers, and for sharing the experience in timing measurements.

I am especially thankful for help given me in the field of software by Tomasz Krakowski and Lukasz Kazmierczak, as well as for Michal Gierlik, who was the head of the activation analysis group working in Accelerators and Detectors project.

A part of the thesis would not exists without the cooperation with Scionix company. I am deeply indebted to Paul Schotanus for the samples of liquid and plastic scintillators, as well as for the discussions during the conferences, schools and workshops.

I would also like to thank Kentaro Fukuda from the Tokuyama corporation for the LiCAF samples, and for being open to cooperation in development of new LiCAF scintillators.

Big thanks also to our collaborators from CEA Saclay, especially to Mathieu Hamel, who is an incredible talented chemists, being able to produce almost any organic scintillator we want.

My thanks belongs also to my husband who always supported me in my any decision, and

helped me in everyday life, giving the opportunity to write this thesis, and lead many projects and ideas to a happy ending.

My greatest thanks goes to my grandmother who always believes in me, and through which I had an opportunity to attend the university, and defend my mater thesis in physics. She gives me faith that dreams come true, therefore this thesis is dedicated to her.

Abstract

The aim of the thesis is to examine and compare the properties of a wide variety of neutron detectors, as well as their potential assessment to replace helium proportional counters. ^{3}He counters are widely used, efficient neutron detectors, with simultaneous low gamma-ray sensitivity, thermal and time stability, and resistance to high doses of ionizing radiation. ^{3}He isotope is the product of the tritium decay, which stockpiles comes from the Cold War. Since the nuclear program in the USA and Russia was closed, the tritium supply is still being reduced, which is associated with the reduction of the ^{3}He, and its increasing prices ("^{3}He crisis"). This resulted the necessity to search the alternative detection techniques, based either on isotopes with large neutron capture cross-section (^{6}Li, ^{10}B, or Gd isotopes), or on light elements, on which neutrons can be scattered (^{1}H, ^{4}He). There was a return to the study on the detectors known for years (e.g. liquid scintillators, which were developed in the sixties of the twentieth century), as well as to the research of new technologies for neutron detection. There are a number of alternative solutions, currently available on the market, both in the commercial phases, and during the laboratory studies.

The aim of the thesis was achieved through a detailed analysis of scintillation properties, such as the amount of light pulse decay time, or the ability to distinguish between gamma-rays from the neutrons. Moreover, detection efficiency studies of selected detectors were also performed. Detection efficiency, and thereby, the speed of the inspection at the borders, is of great importance in ensuring a fluent movement of cargo and passengers. A very important factor, in the choice of a suitable detector, is the ability of discrimination of events from large fluxes of gamma-rays, which can mask the nuclear materials emitting neutrons. According to the American standards criteria (ANSI), the detector used at the borders should generate less

than one false alarm coming from a large flux of gamma-rays per million quanta crossing through the detector. The tests of neutron detectors presented in the thesis, also include this parameter.

In the first part of the thesis, basic properties of neutrons were presented. Neutrons, as electrically neutral particles, do not ionize the medium in a direct way. The selection of detection method depends strongly on the neutron energy, since the cross section for interaction with neutrons in most materials, is correlated with the energy. The first chapter presents the concept of the cross section, as well as the definition of neutron energy ranges, which are important from the point of view of this thesis. The next part of the thesis is the description of the types of neutron interactions with matter. The dissertation also describes neutron sources, dividing them into isotopic ones and accelerators (neutron generators). Introduction to experimental techniques is preceded by the overview of the neutron detectors available on the market. They are divided into two groups: fast neutron detectors based on elastic scattering, and slow neutron detectors based on ^{6}Li(n,α) reaction. The second part of the thesis presents the experimental techniques used in the study of neutron detectors. The method for light yield measurement is presented, as well as the scintillation mechanism in organic materials, which is crucial in neutron/gamma discrimination, is described. Moreover, the decay time for various types of radiation was presented. The detailed study the measurement of light yield as a function of neutron energy, based on the time-of-flight technique, is also described.

The last two chapters is the summary of the experimental results performed with both fast and slow neutron detectors. In the case of fast neutron detectors, a variety of organic scintillators, both in solid and liquid state, were compared. The results indicate the realistic possibility of using large-volumes liquid scintillators as replacements of ^{3}He counters. They reveal high efficiency for neutron detection, however, their sensitivity to gamma-rays requires the shielding of additional passive materials with high mass number, reducing large fluxes of gamma radiation. On the other hand, toxicity and flammability of xylene-based scintillators reduce their wide usage in harsh environments. Additional loading with ^{10}B atoms increase their efficiency to neutron detection in low-energy region. Therefore, in the case of neutron detection at the borders, where neutron fluxes are very small, the most realistic solution for replacement of ^{3}He counters is a high-volume EJ309B5 scintillator. This boron loaded liquid material, based on mineral oils and the solvent with high molar mass

(the manufacturer does not provide any details about the solvent), is less toxic, and has significantly higher flash-point than xylene. An interesting solution are plastic scintillators with with neutron/gamma discrimination properties, which production, until 2012, seemed to be impossible. Plastics have slightly worse neutron/gamma discrimination performance, than organic liquids, however, they may be a non-toxic, and inflammable alternative to liquid scintillators.

In the case of slow neutron detectors, most of available solutions based on ^{6}Li(n,α) reaction can be used as small, hand-held detectors. In this case, the most interesting alternative are LiI(Eu) and CLYC, which, in addition to the capability of neutron counting, also have the ability of gamma-ray spectrometry. Unfortunately, the difficulties in developing large single crystals do not allow to build radiation portal monitors. Alternative solutions are lithium glasses and LiCAF rubber-type scintillators, which can be produced as large samples. However, they do not have the ability to gamma-ray spectrometry, which can be used only as neutron counters. The only detector that meet ANSI standards is the scintillation screen ZnS(Ag)/^{6}LiF, which have very good neutron/gamma discrimination performance, and due to the possibility of combining detectors in large systems, it has also high neutron detection efficiency.

Streszczenie

Celem rozprawy doktorskiej jest przebadanie i porównanie własności szeregu różnych detektorów neutronów, a także ocena ich potencjalnych możliwości w celu zastąpienia helowych liczników proporcjonalnych. Liczniki z ^{3}He są szeroko stosowanymi detektorami o wysokiej wydajności na detekcję neutronów termicznych, z jednoczesną niską czułością na promieniowanie gamma, stabilnością czasową i temperaturową, oraz odpornością na wysokie dawki promieniowania jonizującego. Izotop ^{3}He jest produktem rozpadu trytu, który pochodzi z zapasów jądrowych z okresu zimnej wojny. Odkąd program jądrowy w USA i Rosji został zamknięty, redukowane są stale zapasy trytu, co wiąże się z zmniejszoną podażą ^{3}He, oraz rosnącymi jego cenami (tzw. „kryzys helowy"). Spowodowało to konieczność poszukiwań alternatywnych technik detekcji neutronów, opartych na innych izotopach posiadających wysoki przekrój czynny na wychwyt neutronu (^{6}Li, ^{10}B, izotopy Gd) lub na lekkich pierwiastkach na których neutrony ulegałyby rozproszeniu (^{1}H, ^{4}He). Powrócono do badań nad detektorami znanymi od lat (np. ciekłe scyntylatory, opracowane już w latach sześćdziesiątych XX wieku), jak również rozpoczęto badania nad nowymi technologiami w detekcji neutronów. Obecnie istnieje na rynku szereg alternatywnych rozwiązań, będących zarówno w fazach komercyjnych, jak i w trakcie opracowań laboratoryjnych.

Cel pracy został osiągnięty poprzez szczegółową analizę własności scyntylacyjnych, takich jak ilość światła, czas zaniku impulsu, czy zdolność rozróżniania promieniowania gamma od neutronowego. Przebadano również własności wydajnościowe wybranych detektorów. Wydajność detekcji, a co się z tym wiąże - szybkość inspekcji ładunków na przejściach granicznych ma ogromne znaczenie w zapewnieniu płynności przepływu towarów i osób. Bardzo ważnym kryterium w przypadku wyboru odpowiedniego detektora jest zdol-

ność dyskryminacji zdarzeń pochodzących od silnych strumieni promieniowania gamma, które mogą maskować materiały jądrowe emitujące neutrony. Według kryteriów amerykańskich standardów (ANSI), detektor stosowany na przejściach granicznych powinien generować mniej, niż jeden fałszywy alarm pochodzący z silnego promieniowania gamma, na milion kwantów przelatujących przez detektor. W testach detektorów przedstawionych w rozprawie uwzględniono także ten parametr.

W pierwszej części rozprawy ukazane zostały podstawowe własności neutronów, które jako obojętnie elektrycznie cząstki, bardzo słabo oddziałują z elektronami, nie wywołując bezpośredniej jonizacji ośrodka. Wybór metody detekcji promieniowania neutronowego silnie zależy od jego energii, ponieważ przekrój czynny na oddziaływanie z neutronami w większości materiałów jest skorelowany z energią neutronów. W pierwszym rozdziale przedstawiono pojęcie przekroju czynnego, a także zdefiniowano zakresy energetyczne neutronów, które są istotne z punktu widzenia niniejszej rozprawy. Kolejna część pracy to opis typów oddziaływań promieniowania neutronowego z materią. W rozprawie opisano także źródła neutronów, dzieląc je na źródła izotopowe, oraz akceleratory (generatory neutronów). Wprowadzenie do technik eksperymentalnych poprzedza przegląd detektorów neutronowych dostępnych obecnie na rynku. Podzielono je na dwie grupy: detektory neutronów prędkich opartych o zjawisko elastycznego rozpraszania na lekkich jądrach, oraz detektory neutronów powolnych opartych o reakcję ^{6}Li(n,α).

W części drugiej przedstawione zostały techniki eksperymentalne zastosowane w badaniach detektorów neutronowych. Opisano metodę pomiaru ilości światła w scyntylatorach, jak również przedstawiono mechanizm scyntylacji w materiałach organicznych, który decyduje o zdolności dyskryminacji zdarzeń pochodzących od neutronów oraz promieniowania gamma. Omówiono zasadę pomiaru czasu zaniku impulsów świetlnych pochodzących od różnego rodzaju promieniowania, a także metodę pomiaru krzywej ilości światła, jako funkcji energii neutronów dla scyntylatorów organicznych, w oparciu o informację o czasie przelotu neutronu.

Dwa ostatnie rozdziały to podsumowanie wyników eksperymentów wykonanych z detektorami neutronów prędkich oraz powolnych. W przypadku detektorów neutronów prędkich, porównano szereg scyntylatorów organicznych, zarówno występujących w fazie stałej, jak i ciekłej. Wyniki wskazują na realistyczną możliwość wykorzystania scyntylatorów

ciekłych o dużych objętościach, jako zamienników detektorów helowych. Wykazują się one dużą wydajnością detekcji promieniowania neutronowego, jednakże ich znaczna czułość na promieniowanie gamma wymaga pod dodatkowego ich osłaniania materiałami pasywnymi o wysokiej liczbie masowej, redukującymi silne strumienie gamm. Jednakże ich toksyczności i stosunkowo niski punkt zapłonu scyntylatorów na bazie ksylenu ogranicza ich szerokie zastosowanie w trudnych warunkach atmosferycznych. Dodatkowe doładowanie organicznych cieczy w atomy ^{10}B zwiększa wydajność tych scyntylatorów na detekcję neutronów w zakresie niskich energii. Dlatego też w przypadku detekcji neutronów na przejściach granicznych, gdzie ich strumienie są bardzo niewielkie, najbardziej realną alternatywą dla detektorów opartych o ^{3}He wydaje się scyntylator EJ309B5 - doładowany ^{10}B organiczny materiał na bazie mineralnych olejów i rozpuszczalnika o wysokiej masie molowej (producent nie podaje konkretnej nazwy rozpuszczalnika), który charakteryzuje się mniejszą toksycznością, niż ksylen oraz znacznie wyższą temperaturą zapłonu. Interesującym rozwiązaniem są scyntylatory plastikowe ze zdolnością dyskryminacji neutron/gamma, których wykonanie wydawało się niemożliwe do roku 2012. Posiadają one nieznacznie gorszą zdolność dyskryminacji neutron/gamma, niż organiczne ciecze, jednakże mogą być dla nich nietoksyczną i niepalną alternatywą.

W przypadku detektorów neutronów powolnych, większość dostępnych rozwiązań opartych na reakcji ^{6}Li(n,α) może pełnić rolę jedynie niewielkich, podręcznych detektorów. W tym przypadku najbardziej interesującą alternatywą jest LiI(Eu) oraz CLYC, które oprócz zdolności zliczania zdarzeń od neutronów powolnych, posiadają także możliwości wykonywania spektrometrii gamma. Niestety, trudności w tworzeniu dużych monokryształów tego typu nie pozwalają na budowanie stacjonarnych monitorów promieniowania. Alternatywnymi rozwiązaniami są szkła litowe oraz scyntylatory typu LiCAF rubber, które mogą być tworzone w postaci większych detektorów, jednak nie posiadają one zdolności do spektrometrii gamma, przez co mogą służyć jedynie jako liczniki neutronów. Jedynym rozwiązaniem spełniających wymogi standardów ANSI jest ekran scyntylacyjny ZnS(Ag)/^{6}LiF, który posiada bardzo dobrą zdolność dyskryminacji neutron/gamma, oraz dzięki możliwości łączenia kilku detektorów w większe systemy, charakteryzuje się wysoką wydajnością detekcji.

Contents

Chapter 1

Introduction

1.1 Detection of nuclear materials in homeland security

The passive detection of neutron radiation in homeland security applications is an integral part of the global effort to prevent the proliferation of complete weapons of mass destruction (WMD), and special nuclear materials (SNM) for weapon construction, defined by the Nuclear Regulatory Commission of the United States as highly enriched uranium (HEU) and plutonium [1]. In most cases, gamma-ray passive detectors, as well as various X-ray transmission methods, are sufficient for standard cargo and passenger control. Plutonium and uranium produce gamma-ray signatures, while plutonium emits also large flux of neutron radiation (^{240}Pu produces about 10^6 n/(s·kg) from spontaneous fission [2]). Of these threats, HEU is the most difficult to detect, because gamma-rays are of low energy (can be easily shielded), and the rate of neutrons from spontaneous fission is low (only about 1 n/(s·kg) of material [2]). Detection of WMD and SNM through their gamma-ray signatures are limited by several factors, such as high level and variability of natural background, the presence of naturally occurring radioactive materials (NORM [3]), as well as individuals with radionuclide burdens from medical treatments, and the influence of cargo on the background observed by gamma-ray detectors. In this case neutron detection becomes an important issue, because of low natural neutron background in the normal conditions, and different shielding characteristics in comparison to gamma-rays. While gamma-rays from SNM may penetrate tens of centimeters of material under favorable circumstance, the neutrons with the energy

of about 1 MeV may penetrate through meters of the same materials without any absorption.

Neutrons, as uncharged particles, do not ionize the detector's medium in a direct way. The energy of a neutron is transferred through the indirect processes, and the result of this interaction - the ionizing radiation, such as gamma-rays, or charged particles - occur in following processes:

- elastic scattering on light nuclei, in which the neutron transfers a part of its energy to the recoil nucleus,
- nuclear reactions, such as (n,p), (n,α),
- induced fission reactions,
- induced radioactivity of nuclei (neutron activation).

Neutron detection is an active area of research, and a number of novel technologies are being investigated. The choice of the detection method depends on the neutron energy, because the cross-section for interaction with neutrons is strongly correlated with their energy. In the case of fast neutrons, the predominant interactions are the elastic scattering and activation, whereas for slow neutrons the most significant processes are nuclear reactions (e.g. neutron capture). Moreover, the detector medium should be insensitive to gamma-rays, or the discrimination of events from gamma-rays and neutrons should be possible.

The most common detector used in Radiation Portal Monitors (RPMs) for searching of illicit trafficking of SNM through the neutron signatures, is the ^{3}He-filled proportional counter enclosed in a polyethylene moderator. RPMs consist of large area ^{3}He counters, usually of two tubes, 2 meters long per module [4]. The great advantage of this type of detector is a large cross-section for ^{3}He(n,p) reaction over a wide range of neutron energy (the cross-section for 0.025 eV neutron energy is 5330 barns), as well as negligible sensitivity to gamma-rays, which is a problem only in a very large radiation field of about 1 R/h [5]. ^{3}He counters are simple in design, and are characterized by a stability over a wide range of environmental conditions, not being degraded over years of operation.

Moreover, ^{3}He detectors are applied in basic research projects in nuclear and condensed matter physics (e.g. position sensitive detectors in the Spallation Neutron Source), as well

as the ^{3}He isotope itself is used in medical applications (magnetic resonance lung imaging), and in cryogenics (^{3}He refrigerators can achieve the temperature of 0.2 K). The natural abundance of ^{3}He on Earth is very small (about $1.4\times10^{-4}\%$) therefore, the main supply of this isotope comes from the radioactive decay of tritium, where it is separated during the tritium cleaning process. The major supply of the tritium is derived from the refurbishment and dismantlement of the nuclear stockpile. Two main suppliers of ^{3}He from the nuclear stockpiles are the United States and Russia. Tritium is also produced in the CANDU heavy water reactors in Canada, and is extracted by the Ontario Power Generation in Toronto [5]. The production of ^{3}He from the tritium decay has been decreased as the nuclear program was closed, and the nuclear weapons stockpile has been reduced. However, the demand for ^{3}He has increased, especially since the attack in September 11, 2001. The data presented in 2010 show that the average demand of ^{3}He in the United States was approximately 65 m^3 per year, whereas the supply was dramatically lower - about 20 m^3 per year [6]. The shortage of ^{3}He entailed an increase in the price of this isotope - from about $ 200 per liter up to $ 3000 per liter [7], and have been the ground for searching the alternative technologies for neutron detection, either based on the isotopes with high cross-section for nuclear reactions with neutrons (^{6}Li, ^{10}B, or gadolinium isotopes), or based on light nuclei, on which neutrons can be scattered (^{1}H, ^{2}H, ^{4}He).

There are several solutions that can be commercially used as large area neutron detectors for homeland security applications:

– *proportional counters based on boron trifluoride (BF_3)* - gaseous detectors with a slightly lower neutron sensitivity than ^{3}He-based counter (lower cross section for ^{10}B(n,p) reaction than for ^{3}He(n,p) one) and similar gamma-ray discrimination capabilities. However, BF_3 is a toxic gas.

– *Boron-coated straw detectors* - they have neutron/gamma discrimination characteristics comparable to ^{3}He detectors, but lower sensitivity to neutrons. They are available only in the United States [8].

– *^{6}LiF/ZnS(Ag)-based detectors*. This detector is sensitive to neutrons, and have slightly worse neutron/gamma separation than ^{3}He proportional counters. This system is the only one that is commercially available for homeland security applications under the

name of *Neuport* [9].

– *Liquid scintillators*- based on organic liquids utilizing the phenomenon of neutron elastic scattering. They have good neutron detection efficiency, but worse neutron/gamma discrimination properties than ^{3}He counter. They are toxic, and usually flammable.

1.2 The aim of the work

In addition to above mentioned, commercially available solutions, there are also other alternatives to ^{3}He counter, which are in various stages of the laboratory studies. The aim of the doctoral dissertation is to examine and compare the performance of the neutron detectors, and assessment their potential application as replacements of ^{3}He detectors. The thesis presents the properties of ^{3}He counters, as well as the results of the measurements of alternative neutron detectors, both commercially available, and in the phase of laboratory studies. The thesis is based on manuscripts published in years 2010-2014, in which the properties of various detectors, both in gaseous (^{3}He counters), and solid (stilbene single crystals, composites, ^{6}LiF/ZnS(Ag), and LiCAF) or liquid state (liquid scintillators) are presented.

The thesis is based on following papers:

I Liquid scintillators and Composites in Fast Neutron Detection

J. Iwanowska, L. Swiderski, M. Moszynski
J. of Instr. vol. 7 No C04004 (2011)

II Neutron/Gamma Discrimination Properties of Composite Scintillation detectors

J. Iwanowska, L. Swiderski, M. Moszynski, P. Sibczynski, T. Szczesniak et al.
J. of Instr. vol. 6 No 7 (2011) P07007

III Thermal neutron detection with Ce^{3+} doped $LiCaAlF_6$ single crystals

J. Iwanowska, L. Swiderski, M. Moszynski et al.
Nucl. Instr. Meth. A vol. 652 No 1 (2011) 319-322

IV The BC-704 Scintillation Screen with Light Readout by Wavelength Shifting Fibers as a Highly Efficient Neutron Detector

J. Iwanowska, L. Swiderski, M. Moszynski, D. Wolski et al.

IEEE Nuclear Science Symposium Conference Record (NSS/MIC) (2011)

V Comparison of various plastic scintillators with pulse shape discrimination (PSD) capabilities based on polystyrene (PS)

J. Iwanowska, M. Moszynski, L. Swiderski, P. Sibczynski, T. Krakowski et al.

Nuclear Science Symposium Conference Record (NSS/MIC) 2013

VI Comparative study of large samples (2'' $\times$ 2'') plastic scintillators and EJ309 liquid with pulse shape discrimination (PSD) capabilities

J. Iwanowska-Hanke, M. Moszynski, L. Swiderski, P. Sibczynski, T. Szczesniak,

T. Krakowski et al.

J. of Instr. vol. 9 No P06014 (2014)

VII The time-of-flight method for characterization of neutron response of organic liquid scintillators

J. Iwanowska, L. Swiderski, T. Krakowski, M. Moszynski, T. Szczesniak, et al.

Nucl. Instr. Meth. A 2015

Moreover, some data reported in other papers, with a contribution of the Author were used in the thesis, as follow:

VIII Further Study of Boron-10 Loaded Liquid Scintillators for Detection of Fast and Thermal Neutrons

L. Swiderski, M. Moszynski, D. Wolski, T. Batsch, J. Iwanowska, A. Nassalski,

A. Syntfeld-Kazuch, T. Szczesniak et al.

IEEE Trans. Nucl. Sci. vol. 57 No 1 (2010) 375

IX Comparison of neutron detection efficiency using a He-3 counter and a Boron-10 loaded liquid scintillator EJ309B5

L. Swiderski, M. Moszynski, D. Wolski, J. Iwanowska, T. Szczesniak, J. Szabelski et al.

IEEE Trans. Nucl. Sci. vol. 57 No 5 (2010) 2857

X Suppression of gamma-ray sensitivity of liquid scintillators for neutron detection

L. Swiderski, M. Moszynski, D. Wolski, J. Iwanowska, T. Szczesniak, et al.

Nucl. Instr. Meth. A vol. 652 No 1 (2011) 330

1.3 Thesis structure

The thesis consists of three main parts. The first part presents the aim of the thesis, which is the study on alternatives to ^{3}He proportional counter neutron detectors. These detectors have been widely used in wide area of nuclear physics, where the monitoring of neutrons is of importance, as well as in homeland security applications, where the detection of neutrons is crucial to prevent illicit trafficking of special nuclear materials. Due to a significant decrease in the amount of ^{3}He in the world market, the prices of the counters have increased rapidly. Therefore, the scientific community is seeking for alternative technologies that could replace the ^{3}He detectors. The second part of the thesis is the presentation of the basic properties of neutron radiation, as well as the description of the neutron sources. Moreover, the theoretical introduction to an overview of the various neutron detectors available in the market, as well as in the development phase is given. The third part is the description of the experimental methods that were applied in our laboratory to test the neutron detectors, the results of a study on these detectors, and finally – the discussion on the results, and conclusions.

Particularly, in the second chapter, the basic properties of neutron radiation, and the interaction of neutrons with matter is presented. The interactions were divided into reactions with fast and slow neutrons. Also, the definition of a cross section is described, which is a very important quantity to qualify the material as an efficient neutron detector.

The third chapter covers the description of neutron sources used in the experiments that are described in the sixth and seventh chapters. The properties of a ^{252}Cf source, which emits

neutrons by spontaneous fission process is presented, as well as several (α,n) sources, such as a ^{238}PuBe are characterized. This chapter contains also the principle of operation of neutron generators, both based on solid target, and on Inertial Confinement Concept. The DT neutron generator was used in the experiment of calibration of organic liquid scintillators, which is described in the sixth chapter.

The fourth chapter contains the general overview of neutron detectors that are tested in the sixth and seventh chapters. The basic properties of fast neutron detectors that utilize elastic neutron scattering on hydrogen and carbon are presented. They are divided into few groups: single crystals and composites based on these crystals, liquid, and plastic scintillators. Afterwards, the principle of operation of ^{3}He proportional counter is described. In the next part of the chapter, slow neutron detectors based on ^{6}Li(n,α) reaction are shown.

The fifth chapter contains the description of the experimental techniques that were used for the characterization of neutron detectors purpose. The method for light output measurements with organic scintillators is presented. This chapter contains also the information about the scintillation mechanisms in organic scintillators, which lead to the differences in the scintillation light pulse for various particles that deposit the same energy in organic scintillator. The pulse shape discrimination (PSD) technique for separation of gamma-rays from neutrons in organic scintillators is also described. The PSD is a key technique for the detection of neutron in the presence of gamma-ray background in organic scintillators, described in the literature for over than 50 years. The PSD performance of organic scintillators is the most important parameter when their gamma-ray sensitivity is considered. In the tests of the organic scintillators, an analogue PSD based on zero-crossing technique was applied. In this chapter, the measurement method of decay time constants for organic scintillators is described. This information is crucial in all PSD algorithms to improve the neutron/gamma discrimination. The last section of the fifth chapter contains the description of the experimental method for calibration of organic scintillators based on time-of-flight technique and the DT neutron generator. Most organic scintillators show a nonlinear response to heavy particles, therefore it is necessary to find the relation between the light output and the energy of recoil protons. The information about the response function of organic scintillators is very important, if one needs to know the light output for the particular neutron energy.

The results of the study on neutron detectors are presented in the sixth and the seventh

chapters. The neutron/gamma discrimination with organic scintillators, as well as decay time constants measurements that were performed in our laboratory for various liquid and plastic scintillators are presented. The discussion on suppression of gamma-rays for low-flashpoint EJ309 liquid scintillator is also shown. Additionally, the time-of-flight method for characterization of light output curves for organic scintillators, based on the DT generator, is presented, and the results obtained for several liquid scintillators are discussed. The comparative study of the efficiency of ^{3}He proportional counter and ^{10}B-loaded liquid scintillator is performed. Novel generation of organic scintillators for neutron detection, such as composites based on organic crystalline grains, as well as plastics with PSD properties are shown. The seventh chapter contains the results of the study on slow neutron detectors, both in the laboratory phase of development, as well as commercially available.

The last chapter contains the general conclusions and summary of the thesis.

Chapter 2

Interaction of neutrons with matter

2.1 Discovery of the neutron

The first information about a neutral, subatomic particle, can be traced to as early as 1920. The discoverer of the atomic nucleus and the proton, Ernest Rutherford, in his Bakerian Lecture hypothesized over a hybrid particle consisting of a negatively charged electron bound tightly to a positively charged proton, like a hydrogen atom, but with the electron located basically inside the nucleus. The basis for this consideration was the disparity between the atomic number, and the atomic mass [10]. In 1930, German physicists Walther Bothe and Herbert Becker observed a very penetrating, uncharged radiation, occurring while bombarding light targets (such as beryllium, boron, or lithium) by high energy alpha particles from ^{226}Ra [11, 12]. The study of *"beryllium radiation"* was continued in 1932 by Irene and Frederic Joliot-Curie. They noticed that this radiation, falling on the paraffin, ejects high energy protons that gave a signal in ionization and Wilson's chambers, and concluded that this was gamma-radiation as a result of a Compton scattering. However, theoretical calculations gave a very small cross section for this process. Despite this inconsistency, the results were announced in the article from January 28, 1932 [13]. The suspicious results of French physicists were reviewed at the University of Cambridge by James Chadwick. While testing the scattering of the *"beryllium radiation"* on various materials, he deduced that the radiation must consist of uncharged particles with the mass almost that of a proton [14]. In his experiment, a polonium alpha-emitter source was placed behind a beryllium target (see figure 2.1).

Inside the detector, an alpha-particle hits a beryllium, and a neutron was produced in the *(α,n)* reaction (see chapter 3, section 3.2). Neutrons were detected when they knocked out protons from paraffin. By observing the speed of protons, Chadwick was able to calculate the mass of the neutron to be roughly the same as the proton. The new particles were called as **neutrons** (from the Latin *"neutral"* and the Greek ending – *"on"*) [15].

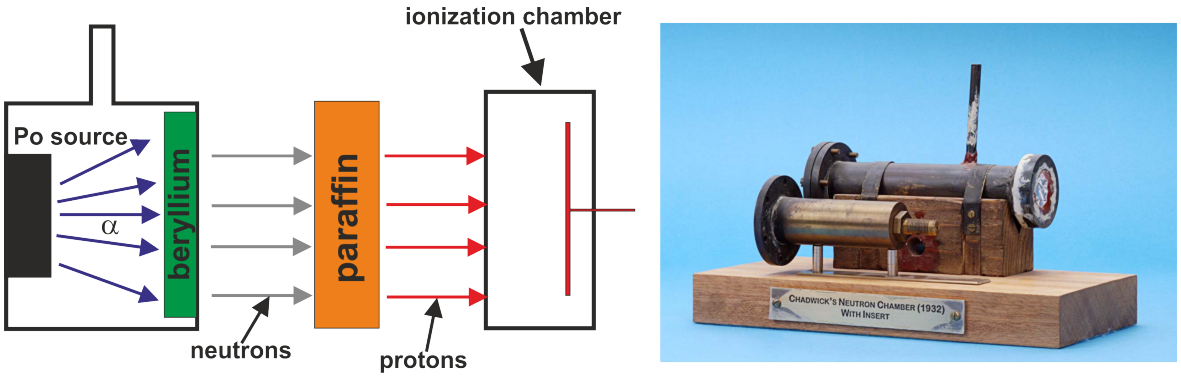

Figure 2.1: *The ionization chamber used by James Chadwick to discover the neutron.*

The existence of the neutron solved the problem of incorrect model of the atomic nucleus as composed of protons and, so-called, "nuclear electrons". Werner Heisenberg [16–18] and Dmitrij Ivanenko [19, 20] independently hypothesized that neutrons, together with protons, are components of the nucleus. Another question was how uncharged neutrons and positively charged protons are bound together despite the existence of a repulsive Coulomb force. In 1935 Hideki Yukawa hypothesised that must exist a force that bind protons and neutrons together [21]. He called it as a "strong force", because it had to be much stronger than the electromagnetic repulsion of positively charged protons.

2.2 The properties of the neutron

The neutron is an uncharged subatomic particle, a component of almost every atomic nucleus (except ^{1}H that consists of a proton only). Its mass is marginally higher than that of the proton, but almost 2000 times higher than that of the electron [22]. The neutron is a fermion with spin equal to $^{1}/_{2}$. According to the experiment presented in [23], it has a positively charged core with the radius of 0.3 fm, surrounded by the negative charge with the radius of 0.3-2.0 fm from the neutron core. Basic properties of the neutron are collected in

table 2.1.

The number of neutrons in the nucleus determines the isotope of an element. For example, the abundant ^{12}C isotope has 6 neutrons and 6 protons, while the radioactive isotope ^{13}C has 7 neutrons and 6 protons. Neutrons that are not bound in the nuclei (*free neutrons*) are unstable; they undergo beta decay to become a proton, emitting an electron and an electron antineutrino [24].

Table 2.1: *Fundamental properties of the neutron*

property	symbol	value	reference
mass	m	$1.674927351(74) \times 10^{-27}$ kg	[25]
mass-energy equivalent	mc^2	$939.565379(21)$ MeV	[26]
lifetime	τ	$880.1(11)$ s	[26]
magnetic moment	μ	$-1.9130427(5)\ \mu_N$	[26]
charge	q	$(-0.4 \pm 1.1) \times 10^{-21}\ e$	[26]

2.3 The cross section concept

The behavior of neutrons passing through matter is significantly different from the charged projectiles (electrons, ions), and photons. The dominant mechanism for energy loss, in the case of charged particles, is the interaction with electrons in the target via the Coulomb forces [27]. Because neutrons have no electric charge, they do not interact electromagnetically with matter. They penetrate the atomic electron cloud, and interact with the target nucleus via the scattering, or nuclear forces, resulting in recoil protons, alpha particles or other nuclei. The neutron detectors utilize the conversion of uncharged incident neutrons into secondary charged particles that ionize the detector medium, and can be further detected directly. There is a variety of possible neutron interactions with target nuclei, depending on the neutron energy. The neutron energy ranges will be described in the section 2.4. Moreover, the interactions differ from one isotope to another of the same element (e.g. hydrogen and deuterium). Therefore, the concept of a **cross section** is used to express the likelihood of interaction between the neutron (and other particles) and the target [28]. If the neutron travels through any material, it will have a certain probability to interact with the material

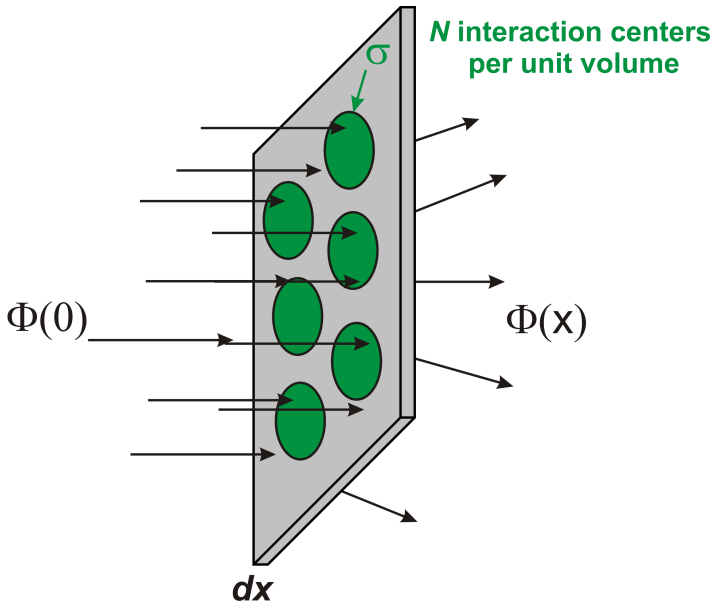

Figure 2.2: *A drawing illustrating the definition of the cross section.*

nuclei. To explain the cross section concept, we consider a very thin slice *(dx)* of matter with the *N* target nuclei per unit volume, each of which has an area of σ (see figure 2.2). The cross section, having a unit of an area, is measured in **barns** (1 barn = 10^{-28} m^2 = 10^{-24} cm^2). The flux of the neutron beam (per time and area unit) that travels through the target without any interaction is equal to $\Phi(x)$. The probability that the neutrons will interact with the target nucleus is equal to the ratio of the "active surface" (covered by the reactive centers) $N\sigma$ and the total surface of the target *S* [29].

$$d\Phi(x) = -\frac{\sigma \Phi N S dx}{S}. \tag{2.1}$$

A minus sign in the equation 2.1 indicates a decrease in the neutron flux at the distance *dx* caused by the interaction with the target.

$$\frac{d\Phi}{\Phi} = -\sigma N dx. \tag{2.2}$$

Solving a differential equation 2.2 and taking into account boundary conditions (for $x = 0$, $\Phi(x) = \Phi(0)$) we obtain

$$\Phi(x) = \Phi(0) e^{-\sigma N x}. \tag{2.3}$$

Equation 2.3 is true only for single event scattering. In materials with high density of scattering centers, or in broad beam geometry, multiple scattering causes some neutrons to be reflected back into the beam. The magnitude of this effect depends on the thickness of the

beam, as well as on the thickness of the target material. Therefore, for multiple scattering, equation 2.3 must be modified to

$$\Phi(x) = \Phi(0)B(\mu x)e^{-\sigma N x}. \tag{2.4}$$

where B(μ x) is the **build-up** factor.

The cross section can be estimated for all possible interaction processes together, in which case they are called **total cross sections**, or for specific processes, such as elastic or inelastic scattering; of the latter, amongst neutron cross sections the absorption cross sections are of particular interest [27] (**partial cross section**).

$$\sigma_{tot} = \sigma_{elastic} + \sigma_{capture} + ... \tag{2.5}$$

The interactions of neutrons with matter from the detection point of view are described in the section 2.4.

The mean path that neutron travels before the first interaction with the target material is expressed as **the mean free path** λ [28]

$$\lambda =< x >= \frac{\int_0^\infty x e^{-\sigma N x} dx}{\int_0^\infty e^{-\sigma N x} dx} = \frac{1}{N\sigma}. \tag{2.6}$$

If the target contains two types of interaction centers, A and B, λ is expressed as

$$\lambda = \frac{1}{N_A\sigma_A + N_B\sigma_B}. \tag{2.7}$$

The cross sections exhibit a strong energy dependence, which is illustrated in figure 2.3 showing the energy dependence of the neutron capture cross section for ^{113}Cd. Moreover, many neutron interactions are characterized by resonances, i.e. the cross section for a certain type of interaction shows a pronounced peak at a particular energy. At the resonance, the cross section is usually orders of magnitude larger than for slightly higher, or lower energy. Resonance peaks are associated with the quantum physics nature of nuclear forces, and they occur if the incoming particle transfers exactly the energy of a discrete state of the compound nucleus [31]. The width of the peaks is a ratio of the Planck's constant $\hbar$ and the lifetime of the resonance state of the system τ [32]

$$\Gamma = \frac{\hbar}{\tau}. \tag{2.8}$$

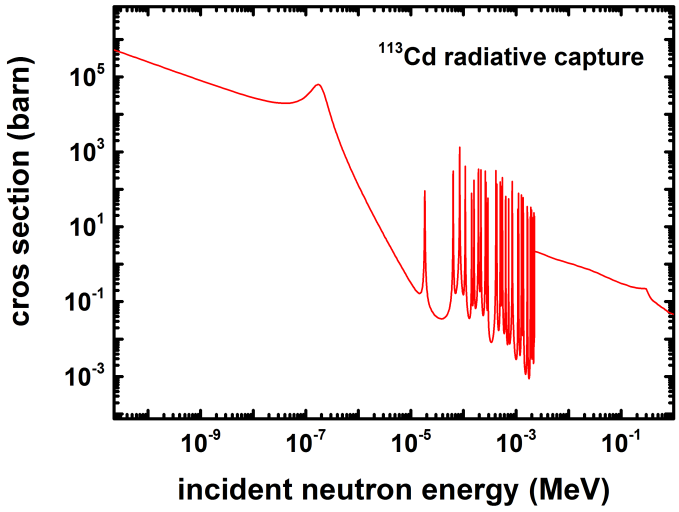

Figure 2.3: *The cross section plot of a neutron capture on ^{113}Cd (from [30]).*

2.4 Neutron energy

Table 2.2: *Neutron energy ranges (from [33])*

nomenclature		energy
slow neutrons	- cold and ultracold	< 0.025 eV
	- thermal [1]	0.025 eV
	- epithermal	0.0025 eV - 0.4 eV
	- cadmium range [2]	0.4 eV - 0.6 eV
	- epicadmium	0.6 eV - 10 eV
	- resonance	10 eV - 300 eV
	- intermediate	300 eV - 10 keV
fast neutrons		10 keV - 20 MeV
relativistic neutrons		> 20 MeV

There are many definitions of neutron energy ranges in the literature that differ slightly one from another. The simplified nomenclature of neutron energies, used for the purposes of

[1] 0.025 eV is the most probable kinetic energy for neutrons at room temperature (Maxwellian distribution).

[2] The nomenclature *"cadmium neutrons"* is related to the neutron absorption cross section of ^{113}Cd. The cross section is very large for energies below 0.5 eV (see figure 2.3) and decreases rapidly for energies above this value. Therefore, the energy of 0.5 eV is referred as *"cadmium cutoff"*.

this thesis is presented in the table 2.2. This thesis relates to the detection of neutrons in the energy range up to approximately 14 MeV, which is limited by the available neutron sources. The neutron sources used for the characterization of neutron detectors will be discussed in chapter 3.

2.5 Types of interactions used for neutron detection

A neutron, depending on the kinetic energy, can undergo many types of interactions with nuclei of a target material. Figure 2.4 presents the graph of neutron interactions with targets divided into two main groups: direct and compound nuclear reactions.

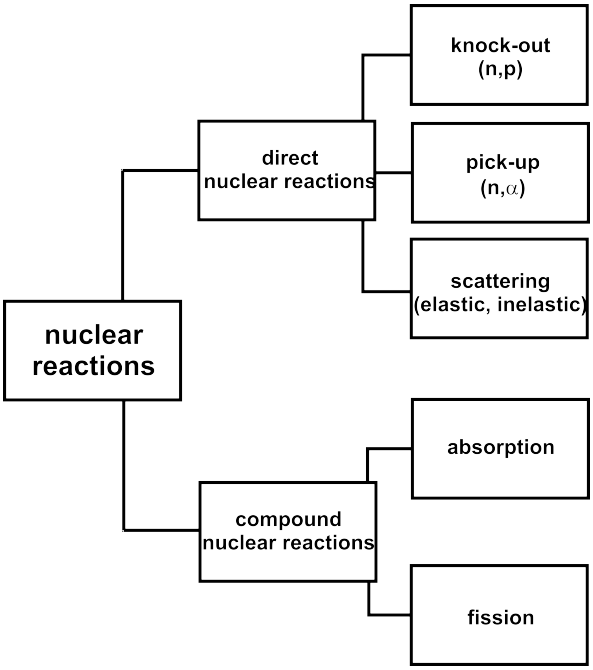

Figure 2.4: *Types of neutron interactions with matter.*

In the case of fast neutrons, the dominant interactions are elastic and inelastic scattering processes. High energy neutrons can transfer an appreciable amount of energy in one collision. Elastic scattering leads to the energy transfer from the neutron to the recoil nucleus. In the case of inelastic scattering, the recoil nucleus is left in an excited state, and decays by emission of gamma-rays, or another form of radiation.

Low energy neutrons interact mostly through absorption and fission processes, because their kinetic energy is too low to be transferred to the target nucleus via the scattering pro-

cesses. The interactions that slow neutrons may undergo are reactions, in which either secondary radiation, or charged particles are created. Because of low energy of the incoming neutron, these reactions must have positive Q-value, to be energetically possible.

Knock-out and pick-up reactions occur for both high and low energy neutrons, depending on the target type. They are considered to be the processes, in which at least one nucleus collides with another object (such as neutron, photon, or another nucleus). At the final stage, two or more products are created. In the initial collision, the projectile and the target must approach close enough to overcome the strong forces. Charged projectiles (e.g. protons, alpha particles) must be accelerated to high energies, because they must overcome the electrostatic repulsion of the target nucleus, or if the target is a neutral atom, the projectiles must penetrate the electron cloud to approach the nucleus. Neutrons have no electric charge and can initiate a nuclear reaction at very low energies.

2.5.1 Elastic scattering

Elastic scattering is the most common method for fast neutron detection. The main principle of this interaction is the transfer of the neutron kinetic energy to the light nucleus (mostly hydrogen) resulting in a recoil nucleus. Afterwards, the recoil nucleus loses the energy in the detector medium. The Q-value for elastic scattering is zero, therefore the total kinetic energy of the reaction product is the same as kinetic energy of the incident neutron. The detectors based on elastic scattering of neutrons on protons are defined as **proton recoil detectors**.

For incoming neutrons with nonrelativistic energy ($E_n < 20$ MeV), conservation of momentum and energy in the laboratory coordinate system gives the following relation for the energy of the recoil nucleus (E_r)

$$E_r = \frac{4A}{(1+A)^2}(cos^2\psi)E_n \tag{2.9}$$

where ψ is the angle between the direction of the incoming neutron and the direction of the recoil nucleus, and *A* is the atomic number. The derivation of the formula 2.9 is given in appendix A. In the case of head-on collision, where the angle $\psi = 0$, the energy transfer from the incoming neutron to the recoil nucleus is maximal

$$E_r|_{max} = \frac{4A}{(1+A)^2}E_n. \tag{2.10}$$

Table 2.3 presents the maximum fraction of the neutron energy that can be transferred to a recoil nucleus in a single collision for various materials that are commonly used in neutron detectors. Detectors containing substances with low atomic number have higher efficiency for neutron detection and are able to detect lower energy neutrons, than those containing substances with higher atomic number.

Table 2.3: *The maximum energy transfer in neutron elastic scattering for various isotopes*

target nucleus	A	$\frac{E_r}{E_n}\|_{max} = \frac{4A}{(1+A)^2}$
^{1}H	1	1.00
^{2}H	2	$^{8}/_{9} \approx 0.89$
^{3}He	3	$^{3}/_{4} = 0.75$
^{4}He	4	$^{16}/_{25}$ = 0.64
^{12}C	12	$^{48}/_{169} \approx 0.28$
^{16}O	16	$^{69}/_{289} \approx 0.22$

The energy loss for a single elastic collision, averaged of the scattering angle, can be expressed by *the average logarithmic energy decrement*

$$\xi = ln\frac{E_n}{E'_n} = 1 + \frac{(A-1)^2}{2A} ln\frac{A-1}{A+1} \tag{2.11}$$

where E_n is the energy of an incoming neutron and E'_n is the energy of a scattered neutron. The detailed derivation of the formula 2.11 can be found in [34, 35]. The value ξ monotonically decreases with increasing atomic number and for hydrogen is equal to 1, whereas for heavier elements converges to $2/A$.

Scintillation detection efficiency

The efficiency of the detector based on recoil nuclei can be calculated using the scattering cross section σ_s. In the simplest case, if the detector contains hydrogen atoms only, the intrinsic efficiency of the detector can be calculated from the equation

$$\epsilon = 1 - exp(-N\sigma_s d) \tag{2.12}$$

where *N* is the concentration of target nuclei in the volume unit (number density), σ_s is the scattering cross section, and *d* is the pathlength of the incident neutron through the detector

[27]. However, organic scintillator contains not only hydrogen, but carbon as well, therefore elastic scattering on carbon must also be taken into account. Hence, the equation 2.12 takes the form of

$$\epsilon = \frac{N_H \sigma_H}{N_H \sigma_H + N_C \sigma_C} 1 - exp[-(N_H \sigma_H + N_C \sigma_C)d]. \tag{2.13}$$

In this case, multiple scattering is neglected.

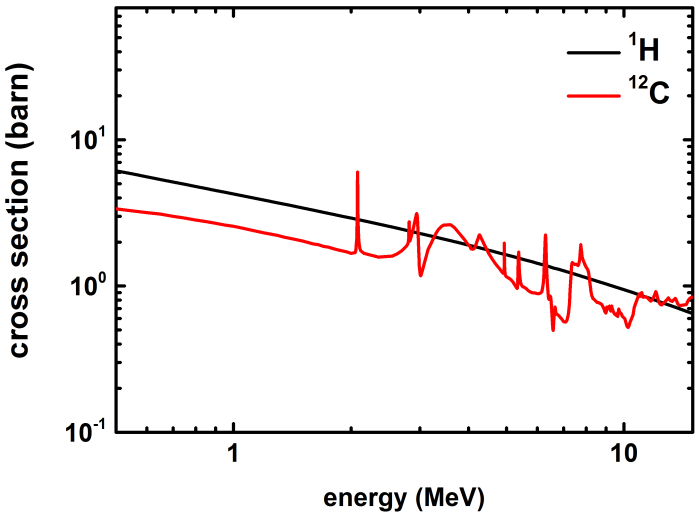

Figure 2.5: *Elastic scattering cross section as a function of neutron energy for* ^1H *and* ^{12}C *(from [30]).*

Plots of scattering cross sections for hydrogen and carbon are presented in figure 2.5. For energies below 2 MeV, the scattering on carbon has lower influence on the detection efficiency, because of two times smaller cross section than that for hydrogen. For energies above 2 MeV we observe resonances; therefore, the elastic scattering on carbon become to be important in calculations of detector's efficiency.

2.5.2 The (n,p) reaction

The (n,p) reaction is an example of a knock-out reaction, in which a neutron enters a nucleus, and a proton leaves the nucleus simultaneously. There are several (n,p) reactions induced by slow neutrons, from which the most important for neutron detection is the reaction on ^{3}He:

$$^3\mathrm{He} + \mathrm{n} \rightarrow {}^3\mathrm{H} + \mathrm{p}. \tag{2.14}$$

The Q-value of this reaction is 0.764 MeV. The kinetic energy of the incoming neutron is small in comparison to the reaction Q-value. Therefore, it is impossible to obtain any information about the neutron energy. Additionally, the incoming linear momentum is almost zero, so the alpha particle and the triton have also a net momentum of zero. They are emitted in the opposite directions sharing the Q-value in the same manner between them as follows

$$E_{^3\mathrm{H}} = 0.191 \text{ MeV}, \tag{2.15}$$

$$E_{\mathrm{p}} = 0.573 \text{ MeV}. \tag{2.16}$$

The cross section plot for ^{3}He(n,p) reaction as a function of neutron energy is presented in figure 2.6. The cross section for this reaction for neutrons with the energy of 0.025 eV is 5330 barns - significantly higher than for other nuclear reactions used for neutron detection, and decreases rapidly with the increasing neutron energy.

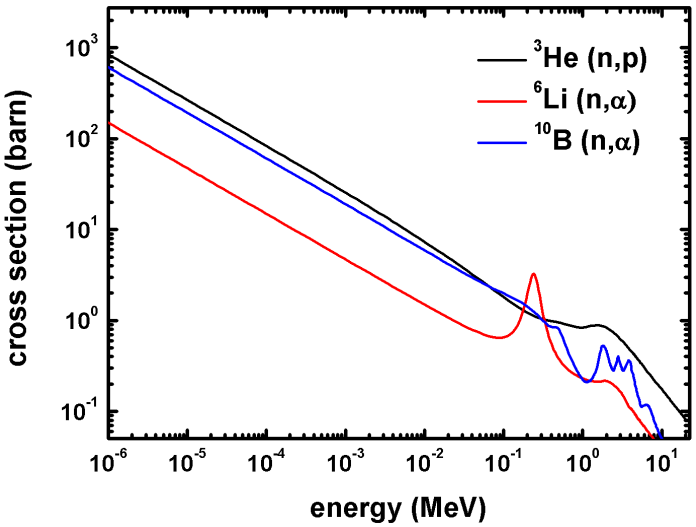

Figure 2.6: *Cross section as a function of incident neutron energy for ^{3}He(n,p), ^{6}Li(n,α) and ^{10}B(n,α) reactions (from [30]).*

^{3}He is manufactured as a tritium decay product from nuclear arsenals of the Cold War as follows

$$^3\mathrm{H}(t_{1/2} = 12.3 \text{ y}) \rightarrow {}^3\mathrm{He} + \beta. \tag{2.17}$$

Since the nuclear program was closed, the tritium supply is still being reduced that leads to the increase of the ^{3}He price. Therefore, a replacement technology for neutron detection is required in the very near future.

Other (n,p) reactions performed with fast neutrons have negative Q-value, therefore there exists a threshold, above which the reaction can occur. The interaction that can be used for fast neutron detection, especially in the case of detection of SNM by photofission, is the ^{19}F(n,p)^{19}O reaction [36]. The neutron interacts with ^{19}F leads to ^{19}O that subsequently undergo β^- and gamma decays with half-life of 26.9 s. The threshold for this reaction is 4.25 MeV [37].

2.5.3 The (n,α) reaction

The most popular pick-up reactions for the conversion of slow neutrons into directly detectable particles that are used in neutron detectors are the (n,α) reactions on ^{10}B and ^{6}Li. The (n,α) reaction on ^{10}B has two branches:

$$^{10}\mathrm{B} + n \rightarrow \begin{cases} ^{7}\mathrm{Li} + {}^{4}\mathrm{He} + 480 - keV\,\text{gamma-ray(excited state)} \\ ^{7}\mathrm{Li} + {}^{4}\mathrm{He}\ \text{(ground state)} \end{cases} \tag{2.18}$$

where the reaction product may be either in the ground, or in the first excited state. From all ^{10}B(n,α) reactions induced by low energy neutrons, about 94% lead to the excited state, and just 6% directly to the ground state. In these two branches, the Q-values are very large: 2.31 MeV and 2.79 MeV, respectively, comparing to the energy of the incoming neutron. The energies of ^{7}Li and alpha particle, are respectively

$$E_{^{7}\mathrm{Li}} = 0.84\ \text{MeV},\ E_{^{4}\mathrm{He}} = 1.47\ \text{MeV (excited state)} \tag{2.19}$$

$$E_{^{7}\mathrm{Li}} = 1.02\ \text{MeV},\ E_{^{4}\mathrm{He}} = 1.77\ \text{MeV (ground state)} \tag{2.20}$$

The cross section for ^{10}B(n,α) reaction is 3840 barns for thermal neutrons (the energy of 0.025 eV), and drops rapidly with increasing neutron energy (see figure 2.6). ^{10}B, which the natural abundance is approximately 20%, is used in *Boron Neutron Capture Therapy* (BNCT) as an experimental treatment of brain tumors and head and neck cancer [38]. The patient is injected with a radiopharmaceutical containing ^{10}B, and is irradiated by a flux of slow neutrons that are captured in the cancer tissue. Alpha particles and ^{7}Li ions from the (n,α) reaction have an average path length of about 12 μm and high LET [3]. Therefore, the

[3]LET (Linear Energy Transfer) - the amount of energy deposited in a given distance by a charged particle moving through the matter. Heavy charged particles are classified as high LET, and electrons - as low LET.

radiobiological effect occurs mostly in cancer tissue, affecting much less on healthy organs. Due to the fact, that the cross section for ^{10}B(n,α) reaction is very high for thermal neutron energies, the neutron sources for BNCT are limited to the nuclear reactors.

Another reaction that is used for slow neutron detection is the (n,α) reaction on ^{6}Li

$$^{6}\mathrm{Li} + \mathrm{n} \rightarrow {}^{4}\mathrm{He} + {}^{3}\mathrm{H}. \tag{2.21}$$

The energy of 4.78 MeV released in reaction 2.21 is divided between the alpha particle and the triton that are oppositely directed in the center-of-mass system

$$E_{^{4}\mathrm{He}} = 2.05 \text{ MeV}, \tag{2.22}$$

$$E_{^{3}\mathrm{H}} = 2.73 \text{ MeV}. \tag{2.23}$$

The cross section plot of (n,α) reaction on ^{6}Li is presented in figure 2.6. The cross section for thermal neutrons is 940 barns, much smaller than for ^{3}He(n,p) reaction. The cross section of ^{6}Li(n,α) reaction has a resonance at the energy of about 250 keV. An advantage of this reaction is a high Q-value resulting in great energy given to the reaction products. The second benefit is the wide availability of ^{6}Li isotope – as a recycling product of lithium-ion batteries.

The (n,α) reaction can also be used for fast neutron detection. For example, ^{19}F(n,α)^{16}N with the energy threshold of 1.61 MeV, undergoing beta decay with a half-life of 11.1 s can be used to detect neutrons emitted during the photofission process. The isotopes that can be used for detection of SNM via the activation method are presented in [37].

The radioactivity induced by neutrons from photofission must have short decay times in the range of tenths to tens of seconds. Moreover, prompt fission signatures must be detected after the events that created them (e.g. after the flash from linear accelerator), without a concern for the overload generated by the primary radiation, and finally, the decay products must be easily detectable.

2.5.4 Radiative capture process

The most significant absorption process in the case of neutron detection is the radiative capture of neutrons on gadolinium isotopes. Gadolinium has the highest cross section for

thermal neutron capture found in any stable isotope - about 255 000 barns for ^{157}Gd (abundance of 15.65%) and 61 000 barns for ^{155}Gd (abundance of 14.8%). Considering a batch of natural gadolinium, approximately 80% of all the capture events occur in ^{157}Gd and 18% - in ^{155}Gd. The other five isotopes of gadolinium give only 2% of the neutron capture probability [39]. The binding energies of the neutron in the capture products are: 8.5 MeV for ^{156}Gd and 7.9 MeV for ^{158}Gd. The capture products are in the excited state, and de-excites by emitting a transition cascade. Most of the cascades lead to low-lying states, where internal conversion occurs. Therefore, the neutron capture by gadolinium gives gamma-rays and conversion electrons.

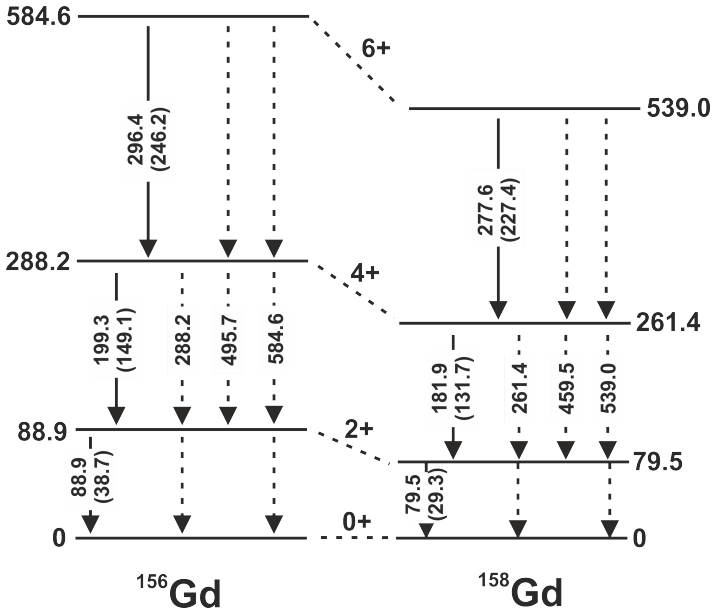

Figure 2.7: *Low-lying level structure of ^{156}Gd and ^{158}Gd (from [40]).*

Figure 2.7 presents low lying level structure of two isotopes of gadolinium: ^{156}Gd and ^{158}Gd. The structure of these levels is quite similar for both of them. Gamma-ray energies (in keV) of individual transitions, as well as energies of coincidence sum peaks are presented. Energies of K-shell conversion electrons are given in parentheses. The $2^+ \rightarrow 0^+$ transition undergoes internal conversion 70% of the time, whereas the $4^+ \rightarrow 2^+$ transition is converted approximately 17% of the time. The most significant product of neutron capture on gadolinium is a 71-keV conversion electron that is emitted in 39% of the capture reactions. The range of those electrons in typical gadolinium foils is few tents of μm, therefore the scintillator with such thickness is enough to convert the incident neutrons into secondary electrons. Therefore, gadolinium-based films are frequently used for neutron imaging as position-sensitive detec-

tors. Liquid scintillators may also contain gadolinium in solution, typically at about 0.5% to 1.5% concentration [27]. However, an important factor in the case of liquid scintillators is the efficient discrimination of the neutron capture reaction products from the gamma-ray background.

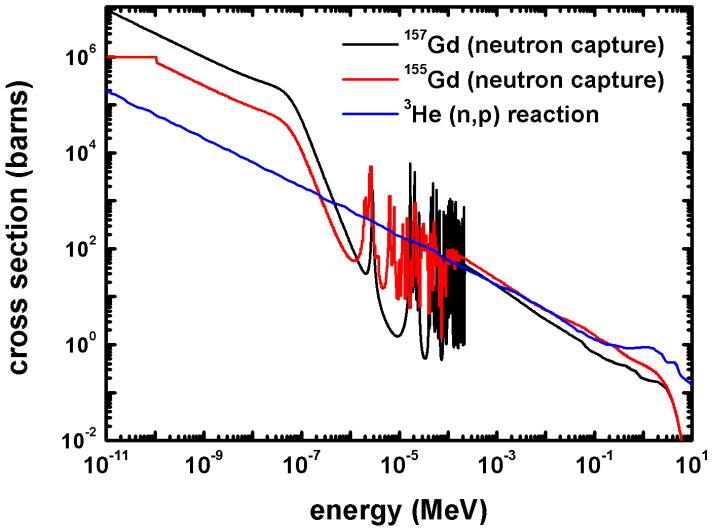

Figure 2.8: *The cross section plots for neutron capture on ^{155}Gd and ^{157}Gd. The cross section for $^{3}He(n,p)$ reaction is presented as a comparison (from [30]).*

Table 2.4: *Internal conversion electrons (ICE) emitted during the de-excitation of ^{158}Gd and ^{156}Gd [41]*

ICE from ^{158}Gd (keV)	yield per neutron	ICE from ^{156}Gd (keV)	yield per neutron
29	0.0982	39	0.0419
71	0.268	81	0.0497
78	0.0617	88	0.0116
131	0.0341	149	0.0084
173	0.0146	191	0.003
180	0.0031	198	0.0006
228	0.004	246	0.0002
total yield	0.4837	total yield	0.1154

Neutron capture cross section for ^{155}Gd and ^{157}Gd as a function of neutron energy is shown in figure 2.8. It is seen that for energy up to 0.5 eV, the capture cross section for gadolinium is much higher than for the cross section for ^{3}He(n,p) reaction. Therefore,

gadolinium-based detectors are suitable for detection of neutrons with energies below 0.5 eV.

Chapter 3

Neutron sources

Due to the fact that neutrons can be emitted from the nuclear states, which have the excitation energy greater than the binding energy of a neutron, and these states are not populated in the natural radioactive decays, natural neutron emitters are rare, and have very short lifetimes. The isotope with the longest lifetime, which emits neutron after the beta decay with the lifetime of 55s is ^{87}Br. In this case, neutron emission is from the excited states of ^{87}Kr [42]. Practically, the natural neutron emitters that can be used in the laboratory conditions do not exist. Laboratory sources, instead, are based on either spontaneous fission, or - induced by the heavier particles - nuclear reactions. Moreover, in the case of neutron sources the important issues are: the energy and rate of the neutrons, the size of the source itself, the cost of purchase and maintaining, and finally the government regulations related to the transport and storage of the source.

3.1 Nuclear fission

The spontaneous fission (SF) of the transuranic nuclei (with the mass number greater than 230), in which heavy nucleus splits into lighter parts and free neutrons are emitted, is a natural source of neutron radiation. About 100 radionuclides are known to decay by the SF with the emission of neutrons. The ^{252}Cf is widely used, commercially available example of the SF neutron source, also used for the purpose of this thesis. It decays with a half-life of 2.65 years primarily by alpha emission-with approximately 97% probability - whereas 3% of

^{252}Cf decay occurs by the SF. The neutron yield emitted from the ^{252}Cf is 2.34$\times 10^{12}$ n/(s·g), whereas alpha particles are emitted in the yield of 1.9 $\times 10^{13}$ α/(s·g). When ^{252}Cf is used as a neutron source, it is encapsulated in a few-millimeter thick container, so only neutrons and gamma-rays emerge from the source. The intensity of neutrons from ^{252}Cf spontaneous fission has a maximum between 0.5 and 1 MeV (see figure 3.1).

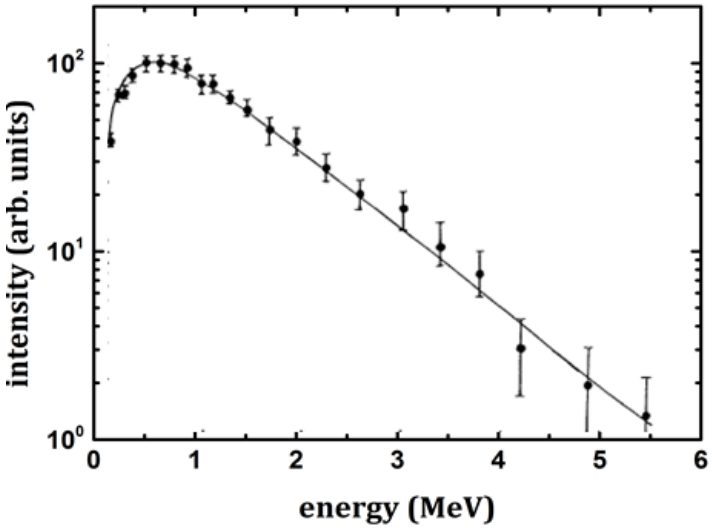

Figure 3.1: *The neutron energy spectrum from the spontaneous fission of ^{252}Cf [43].*

Table 3.1: *The properties of californium isotopes in the sources marked as ^{252}Cf; half-life ($t_{1/2}$), spontaneous fission branching fraction (χ_{SF}) and average number of neutrons emitted per one fission process ($\overline{n}_{SF}$) (data from [44]).*

Isotope	$t_{1/2}$ (years)	χ_{SF}	$\overline{n}_{SF}$
^{252}Cf	2.645(6)	3.092(8) $\times 10^{-2}$	3.757
^{251}Cf	898(44)	~ 0	
^{250}Cf	13.08(9)	7.7(3)$\times 10^{-4}$	3.50(9)
^{249}Cf	351(2)	5.0(4)$\times 10^{-7}$	

The source, marked by the manufacturers as the ^{252}Cf, contain admixtures of other isotopes. The isotopic composition of the majority of the sources is: ^{252}Cf: 80-90%, ^{250}Cf: 5-15%, ^{251}Cf: 2-4%, ^{249}Cf: 2-6%, trace amount of other californium isotopes, and ^{248}Cm [45]. These isotopes emit not only neutrons and alpha particles, but also gamma-rays; i.e. ^{252}Cf isotope emits 10 gamma-ray quanta per one fission [46]. Among the isotopes contained in the source of californium, except ^{252}Cf, also ^{250}Cf source is of importance. However the fis-

sion occurs only for 0.00077(3) of all decays, the content of ^{250}Cf isotope is relatively large. Therefore, for old californium source (over than 10 years), the majority of the neutrons is emitted not from the ^{252}Cf, but from ^{250}Cf isotope [47].

3.2 The (α,n) sources

It is worth noting that the reaction used by Chadwick to produce neutron radiation, described in the chapter 2, section 2.1 remains an important method of producing a neutron source, particularly when a relatively small and easily transportable source is required. Because the number of heavy radionuclides (especially from uranium and thorium decay chain) undergo alpha decay, it is possible to produce a neutron source by mixing an alpha emitter with the target material, e.g. beryllium. The nuclear reaction, which occurs between alpha particle and the beryllium nucleus, terminates with the emission of unstable ^{13}C, which decays as follows

$$^{4}\mathrm{He} + ^{9}\mathrm{Be} \rightarrow {}^{13}\mathrm{C}^{*} \rightarrow \begin{cases} {}^{12}\mathrm{C}^{*} + \mathrm{n} \\ {}^{8}\mathrm{Be} + \alpha + \mathrm{n} \\ 3\alpha + \mathrm{n} \end{cases} \tag{3.1}$$

Decay channel of ^{13}C depends on its excitation energy. However, the dominant reaction is the transition either to the ground state, or to the excited state with the energy of 4.4 MeV. The important feature for (α,n) neutron sources is a half-life of alpha emitters. They usually have long half-lives (with the exception of ^{210}PoBe). Beyond the emission of alpha- and neutron radiation, these sources also emit gamma-rays; moreover, the majority of the dose outside the shielding is caused by gamma radiation. Therefore, the neutron yield in comparison to total radiation is an important criterion for selection of (α, n) sources (the last column in table 3.2 shows the neutron yield of the source relative to its total radiation output in curies).

The energies of the neutrons emitted from the (α, n) sources vary over the broad spectrum (see the neutron energy spectrum from ^{239}PuBe source in figure 3.2). This fact is a consequence of several factors: the sharing of the liberated energy between the reaction products, the varying directions of emission of neutrons form the nucleus, and the variations in kinetic energies of alpha particles. The energy spectra of the (α,n) neutron sources based on beryl-

Table 3.2: *The neutron sources from the (α,n) reaction [2]*

source	half-life (years)	average alpha energy (MeV)	average neutron energy (MeV)	maximum neutron energy (MeV)	gamma dose (mrem/h) at 1m (10^6 n/s)	Yield in 10^6 n/s
^{210}PoBe	0.38	5.3	4.2	10.9	0.01	2-3
^{226}RaBe	1600	4.8	4.3	10.4	60	0-17
^{238}PuBe	87.74	5.49	4.5	11.0	0.006	2-4
^{238}PuLi	87.74	5.49	0.7	1.5	$\sim$1	0.07
$^{238}PuF_4$	87.74	5.49	1.3	3.2	$\sim$1	0.4
$^{238}PuO_2$	87.74	5.49	2.0	5.8	$\sim$1	0.003
^{239}PuBe	24120	5.15	4.5	10.7	6	1-2
$^{239}PuF_4$	24120	5.15	1.4	2.8	$\sim$ 1	1-2
^{241}AmBe	433.6	5.48	5.0	11.0	6	2-3
^{241}AmLi	433.6	5.48	0.3	1.5	2.5	0.6
^{241}AmB	433.6	5.48	2.8	5.0		
^{241}AmF	433.6	5.48	1.3	2.5		

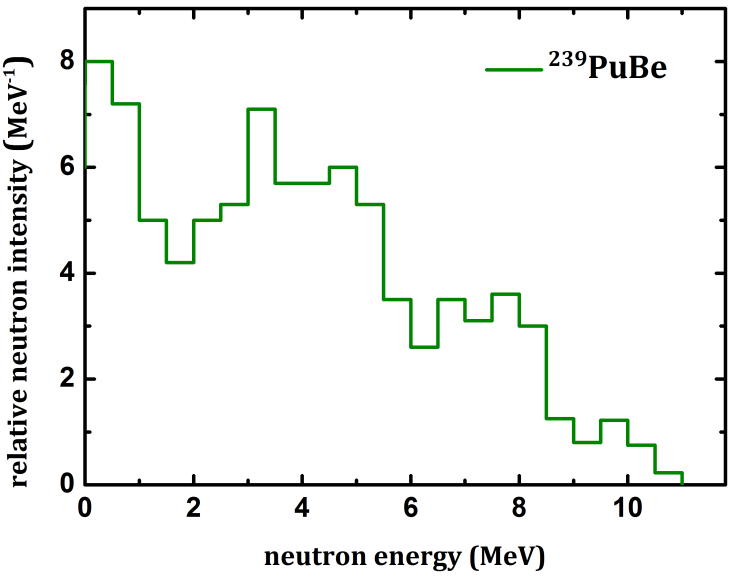

Figure 3.2: *Neutron energy spectrum of ^{239}PuBe containing 80 g of plutonium [48].*

lium are similar, and slight differences are only caused by the variations in primary alpha particle energies. The detailed description of alpha-emitters and target materials that can be used for manufacturing of the (α, n) sources can be found in [2].

3.3 Neutrons from nuclear fusion

Alpha particles originating from transuranic nuclei are the only light nuclei easily available from the isotopes. The other charged particles must be created in the ion source, and accelerated artificially in order to induce the nuclear reaction. In nuclear fusion, an accelerated nucleus collides with the target material creating a new atomic nucleus, and releasing free neutrons. The fusion process has a threshold, being a consequence of the repulsive Coulomb force between the reactants, and occurs when at least one of the nuclei has an appropriate kinetic energy to overcome the Coulomb barrier. If the nuclei reach each other, the strong nuclear forces bind them together forming a new nucleus. The most common reactions used for neutron production are deuterium-tritium (DT) and deuterium-deuterium (DD) fusion.

3.3.1 The DT reaction

Fusion of deuterium and tritium results in the creation of an alpha particle and a neutron. The Q-value of 17.6 MeV is divided between the kinetic energies of the reaction products.

$$^{2}\mathrm{D} + ^{3}\mathrm{T} \rightarrow {}^{4}\mathrm{He} + \mathrm{n} \tag{3.2}$$

The energy of the emitted neutron varies depending on the value of the angle between the incoming deuteron and the neutron in laboratory frame (see Appendix B). However, assuming that the tritium is at rest, and the deuteron has an infinitesimal kinetic energy in comparison to the Q-value, the incoming linear momentum is almost zero. Therefore, the alpha particle and the neutron have also a net momentum of zero, and they are emitted in the opposite directions sharing the Q-value in the same manner between them as follows

$$\mathrm{E}_{\alpha} = 3.5\ \mathrm{MeV}, \tag{3.3}$$

$$\mathrm{E}_{n} = 14.1\ \mathrm{MeV}. \tag{3.4}$$

3.3.2 The DD reaction

In the case of fusion of two deuterium ions, ^{3}He and a neutron are created

$$^{2}\mathrm{D} + ^{2}\mathrm{D} \rightarrow {}^{3}\mathrm{He} + \mathrm{n}. \tag{3.5}$$

Similarly, as in the case of the DT reaction, the energy of the neutron varies with the angle between the deuteron and the neutron (in the laboratory system). In the simplest case, the Q-value is divided between the two products as follows

$$\mathrm{E}_{^3\mathrm{He}} = 0.81 \text{ MeV}, \tag{3.6}$$

$$\mathrm{E}_n = 2.45 \text{ MeV}. \tag{3.7}$$

3.3.3 Neutron generators

Fusion reactions are widely exploited in neutron generators. They are the most common, accelerator-based neutron sources. Since Coulomb barrier between the deuteron and light target nucleus is small, so that deuterons do not have to be accelerated to high speed. Accelerating potential can be of the order of 100-300 keV. In opposition to isotopic sources that emit the neutrons constantly, the generators can simply be powered off when not in use and the neutron emission is stopped [49].

Solid target generator

Solid target generator consists of a compact linear accelerator (neutron tube) that includes an ion source, acceleration stages and a metal target containing tritium, or deuterium. The neutron tube is encapsulated in a metal housing, (the accelerator head) filled with the sulfur hexafluoride – a gas, used as a dielectric medium to insulate the high voltage elements from the operating area. The ions are accelerated by an external power supply to the energy of approximately 100 keV, and hit the target creating the fusion reaction. The solid target neutron generator Genie 16C produced by EADS Sodern was used for calibration of liquid scintillators that will be described in the section 5.4 in chapter 5.

Generator based on Inertial Electrostatic Confinement (IEC) concept (from [50])

The other construction of a neutron generator is based on the IEC concept, in which high voltage is used to induce a glow discharge in a low pressure deuterium gas. A hollow

transparent grid cathode (-) is surrounded by anode (+) at ground potential. The deuterium ions are accelerated and attracted to the cathode, whereas positively charged anode deflect the ions. The presence electric field results in a high ion density inside the grid. The use of a transparent cathode minimizes the ion loss to the grid and allows significant recirculation of energetic ions that are accelerated to the kinetic energy of approximately 15 keV, where fusion collisions can occur. In order to sustain the glow discharge, the operating gas pressure of $\sim$ 1 Pascal is necessary.

Chapter 4

An overview of the tested neutron detectors

Neutron detectors are used not only in homeland security applications, where large volumes with high sensitivity are required, but also in wide range of other fields, such as studies on elastic and inelastic neutron scattering in nuclear physics experiments, neutron-induced fission, or reactions on radioactive nuclei. Fast neutrons generate signals in the detectors mainly via the elastic scattering process, resulting in the recoil nuclei that ionize the medium directly. Therefore, fast neutron detectors usually contain large concentration of hydrogen atoms, because the energy of the neutrons can be transferred the most efficient for atoms that have similar atomic mass, as neutrons. The overview of fast neutron detectors covers the information about organic scintillators, such as single organic crystals, composites, liquid and plastic scintillators. They are composed of aromatic hydrocarbon molecules, and utilize fast neutron elastic scattering on hydrogen and carbon. Organic liquid scintillators, loaded with ^{10}B and utilizing the ^{10}B(n,α) reaction are proposed as detectors sensitive to neutrons of energies ranging from tens of MeV down to thermal. Fast neutrons are detected by registering recoiled protons, whereas slow neutrons are captured by ^{10}B atoms. The main goal of loading them with ^{10}B is the enhancing their total neutron detection efficiency.

Besides ^{3}He proportional counter, slow neutron detectors presented in this dissertation, are based on the ^{6}Li(n,α) reaction. They are usually composed of materials with low atomic number, lowering their sensitivity to high energy gamma-rays, and are highly enriched with

^{6}Li atoms, up to 95% in the scintillation material, which allows high neutron detection efficiency. In order to detect fast neutrons with a ^{6}Li-containing scintillators, the detector must be surrounded with a moderator material, such as polyethylene, or paraffin.

4.1 Fast neutron detectors

The ability to measure the energy of the incoming neutron is a very important distinction in the application of fast neutron detectors. In the case of slow neutron detectors, this information is lost in the conversion processes, because the energy of an incoming neutron is significantly smaller than the reaction Q-value. Nuclear reactions used for slow neutrons detection converts neutrons into detectable charged particles and, in principle can be applied to fast neutron detection, as well. However, the cross section for nuclear reactions decreases rapidly with increasing neutron energy, and detectors that utilize these reaction have extremely low detection efficiency for fast neutrons and are almost never used for this purpose. Nevertheless, there are some applications, in which nuclear reaction on ^{6}Li, or ^{3}He are used for fast neutron detection. These detectors are described in details in [27]. The most common technique that is used for fast neutron detection is based on elastic scattering of neutrons by light nuclei. In elastic scattering process, the Q-value is zero, therefore the total kinetic energy after the interaction is the same as the kinetic energy in the initial stage. The detailed description of elastic scattering process can be found in the section 2.5.1 in chapter 2, and in appendix A.

4.1.1 Proton recoil scintillators

Organic single crystals

Scintillation materials containing hydrogen are quite common, therefore there are many candidates for use as fast neutron detectors. Among all scintillators developed for fast neutron measurements, organics are the most widely exploited either in the time-of-flight method, if appropriate pulsed or tagged neutron sources are available, or by unfolding of pulse height spectra. Pure organic crystals, such as anthracene ($C_{14}H_{10}$), stilbene ($C_{14}H_{12}$)

and *p*-terphenyl ($C_{18}H_{14}$) are the oldest organic materials used for fast neutron detection purposes. They are characterized by a very good scintillation efficiency and pulse shape discrimination (PSD) performance, which will be described in details in the later discussion. On the other hand, it is difficult to obtain them in large sizes, because macrostructures appearing during the growth process, distort their light output. It is also reported that the light output of organic single crystals is anisotropic - it depends on the orientation of an ionizing particle with respect to the crystal axis [51, 52]. These variations can be as much as 20-30%, and are responsible for decreasing the energy resolution of the crystals. The information from 2014 indicates that the group from Lawrence Livermore National Laboratory in the United States has managed to develop the method for growing single stilbene crystals in large sizes [53], and they are now commercially available by Inrad Optics company. Maximal dimension of the cylindrical samples reported in the datasheet is ⌀5.08 cm × 10.16 cm [54]. The samples of large stilbene single crystal are presented in figure 4.1.

Figure 4.1: *Cylindrical samples of stilbene crystal with dimension of ⌀2.54 cm × 2.54 cm (the courtesy of Inrad Optics).*

Composite scintillators

Further development in organic scintillators for neutron detection are composites. They are prepared from small grains of stilbene, or *p*-terphenyl introduced into silicone matrix, which enhance the light diffusion through the scintillator. The details of their preparation, and the optimization of the size of the grains have been reported in [55]. A single crystal boule of

p-terphenyl doped by 1,4-diphenylbutadiene-1,3, or stilbene is grown; afterwards the boule is grinded at a low temperature to obtain specific cell size. As the composite scintillator consists of active and passive components, the crystal grain size plays an important role in the neutron detection efficiency. Various sizes of grains were compared with the range of detected particles, and the results showed that the most optimal value is 1-2 mm [55]. The grain fractions are introduced into the silicone matrix based on Sylgard-527, which acts as a diffuser, enhancing the light diffusion through the scintillator [56]. Measurements made with the refractometer IRF-464, have shown that the refractive index of Sylgard-527 is equal to 1.41, whereas the refractive index of stilbene is 1.64, and *p*-terphenyl is 1.65. The composite is encapsulated in a hermetic housing made of an organic glass, which is resistant to damages. The photograph of the sample of composite scintillator that was tested in our laboratory is presented in figure 4.2.

Figure 4.2: *The photograph of a composite scintillator sample (from II).*

Liquid scintillators

The early extensive work on organic liquid scintillators for neutron detection comes from 1979, and covers the study of NE213 [57]. Liquid scintillators are constituted from a fluorescent emitters dissolved in an aromatic hydrocarbon solvent, such as xylene, toluene, or benzene. Sometimes, they contain additional component (so-called *second fluorophore*) that shifts the emission spectrum of the liquid scintillator to better match the spectral response of the photomultipliers [58]. They are widely available in the market, because it is relatively easy to obtain them in large sizes, which is important in the case of efficient neutron detec-

tion. Liquid scintillators are sold in sealed aluminum containers with quartz glass window. It is necessary for the solution to be packed in the oxygen-free atmosphere, because dissolved oxygen is a quenching agent that reduced the light output of the scintillator [59]. Liquid scintillators can be also loaded with isotopes that have large cross section to nuclear reactions with low-energy neutrons (such as ^{10}B), which results in enhancing detection efficiency. The main disadvantages of liquid scintillators are their toxicity, flammability (except the scintillator with the commercial name EJ309 from Eljen Technology [60]), as well as the fact that they can be leaky in time. Table 4.1 presents the basic parameters of liquid scintillators tested in our laboratory. The scintillators manufactured by Eljen Technology starting with the letter *E*, whereas the scintillators from Saint Gobain (formerly Bicron) starting with the letters *BC*.

Table 4.1: *Basic parameters of liquid scintillators tested in our laboratory (VIII).*

scintillator	**^{10}B loaded (weight%)**	**density (g/cm^3)**	**flash point (°C)**	**H:C ratio**
BC501A	no	0.87	24	1.21
EJ301	no	0.87	26	1.21
EJ309	no	0.96	144	1.25
BC532A	4.4%	0.92	-8	1.74
BC532A2	2%	0.92	-8	??
EJ339A2	2.5%	0.92	-8	1.49
EJ309B5	4.6%	0.96	144	1.31

Figure 4.3: *The photograph of liquid scintillator cells (the courtesy of Eljen Technology).*

Plastics

A good level of PSD, similar to this obtained with liquid scintillators must also work in plastics, because crystallographic structure is not necessary for PSD capabilities [61]. However, for 50 years PSD in plastic scintillators has been reported to be absent, or significantly inferior to that in stilbene, or liquid scintillators, leading to an opinion that plastics are unsuitable for neutron detection via PSD technique [62]. The motivation for the studies on plastics with PSD was provided by several groups of scientists [V, VI], [63], from which the most intense work was done by Natalia Zaitseva's group from Lawrence Livermore National Laboratory [64]. On the basis of their patent [65] Eljen Technology has manufactured the first samples of commercial plastic scintillators [66]. The first PSD performance of commercially available plastic scintillators were performed by Pozzi *et al.* [67] and Cester *et al.* [68]. They are, at this time still under development in regard to optimized the composition and manufacturing procedures. Cylinders up to 12.7 cm diameter $\times$ 15.0 cm long and plates with the surface of 6.25 cm^2, and up to 1.5 cm thickness. The photograph of two samples of plastic scintillators is shown in figure 4.4.

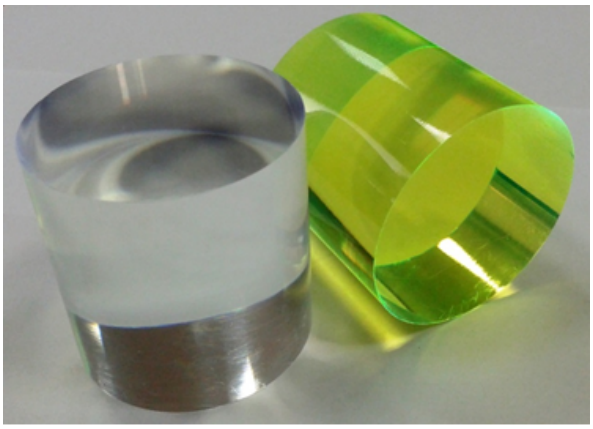

Figure 4.4: *The photograph of plastic scintillators (cylinders with the dimension of ⌀5.08 cm $\times$ 5.08 cm) provided by Eljen Technology.*

4.2 Slow neutron detectors

Every type of neutron detectors are the combination of a target material to convert the energy of an incoming, uncharged neutron into a detectable form. The kinetic energy of

slow neutrons is too low to be transferred through elastic scattering process; therefore, they are generally detected through nuclear reactions that result in emission of prompt energetic charged particles such as protons, or alpha particles. Gamma-rays produced by neutron capture are also used in some specialized detectors, but these applications are relatively rare. The most significant reactions used for slow neutron detection are sufficiently exothermic, which means that the kinetic energy of the reaction products is determined by the Q-value of the reaction and does not reflect the kinetic energy of incoming neutron. The slow neutron detectors presented in this thesis are limited to those that indicate only the detection of a neutron without providing the information about its energy. There are devices that are able to measure the energy of slow neutrons, such as crystal spectrometers, or mechanical monochromators, but they are usually very complex and research-oriented detectors [27].

4.2.1 The ^{3}He proportional counter

The ^{3}He(n,p) reaction exhibits a neutron cross section with $1/\upsilon$ dependence up to 200 keV and equal to 5330 barns for thermal neutrons at the speed of 2200 m/s. The reaction energy of 764 keV is shared between the triton and the proton (see section 2.5.2 in chapter 2). Because ^{3}He is a noble gas, the medium of the detector must be fabricated in a gaseous form with sufficient pressure and purity. Neutron detection efficiency of this type of detector depends on the pressure of the gas inside.

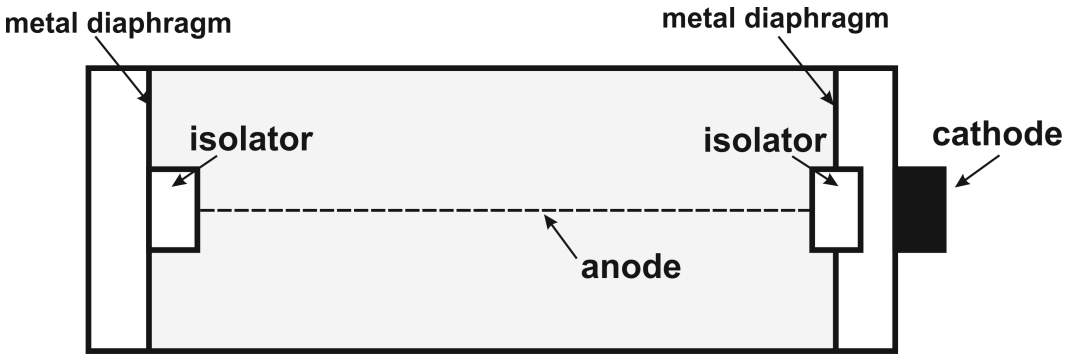

Figure 4.5: *Schematic diagram of a ^{3}He counter [69].*

A typical ^{3}He counter consists of a gas-filled tube with a high voltage applied across the anode and the cathode (see figure 4.5). A neutron, interacting with the ^{3}He produces a tritium and a proton. The proton and the triton ionize the surrounding gas, and create a charge

cloud, which in turn ionizes the other ^{3}He atoms in an avalanche-like multiplication process. The total charge is accelerated to the anode, and collected as the electrical pulses with the amplitude proportional to the neutron energy (proportional mode of operation). The pulses are collected to form a pulse-height energy spectrum. The exemplary pulse-height spectrum from the ^{3}He proportional counter is presented in figure 4.6. Two reaction products, oppositely directed - the proton and the triton - have energies 573 keV and 191 keV, respectively. If two of them deposit its energy in the detector medium (case A), the energy of 764 keV is registered. In the case of escaping one of the particles (case B and C) the registered energy is less than 764 keV. This phenomenon, called as *"wall effect"* is seen at the pulse height spectrum as a tail in the energy ranges from 191 keV (the energy of the triton) up to 764 keV [70]. A characteristic setoff at the energy of 573 keV, originated from the fact that the proton and the triton move in opposite direction, and only one of them is able to escape from the detector. The wall effect is a sum of two tails:

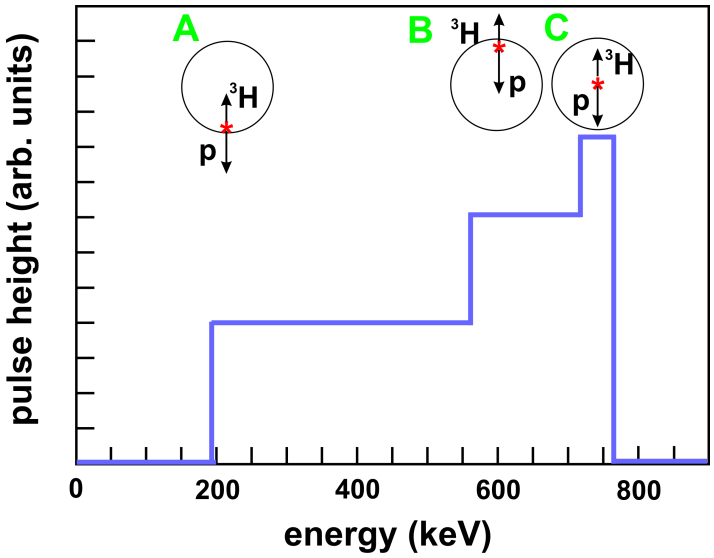

Figure 4.6: *The idea of the spectrum obtained from ^{3}He counter [69].*

– from 191 up to 573 keV – the whole energy of the triton and the part of the energy of the proton is registered,

– from 573 up to 764 keV – the whole energy of the proton and the part of the energy of the triton is registered.

The wall effect is a consequence of the range of the proton and the triton – in the normal conditions, the range of 573-keV proton is about 50 mm [71]. The admixtures of additive

gases, such as argon or krypton, reduces the range of the proton in the detector. Also, the addition of a few percent of polyatomic gas keeps the detector in the proportional mode operation (to prevent the excessive discharge that leads to the Geiger-Müller mode of operation) [27]. Typical gas additives that have been used in practical applications are Xe-CO_2 mixture. It should be noted that the larger photon cross-sections of the admixtures results in a slightly poorer discrimination of gamma-rays. Moreover, the addition of other than ^{3}He gases results in additional contributions to pulse height distribution (e.g. from recoil carbon).

4.3 Detectors based on the ^{6}Li(n,α) reaction

In the search for alternative methods of neutron detection in the crisis of ^{3}He shortage, it is worthy to focus on ^{6}Li(n,α) reaction that has high cross section of 940 barns for thermal neutrons. Because a stable lithium-containing proportional gas does not exist, lithium-based equivalent of ^{3}He, or BF_3 counters is not available. Nonetheless, large reaction energy offers an advantage in discrimination against external gamma-ray background, or other low-amplitude events. Because ^{6}Li(n,α) reaction goes exclusively to the ground state of the product nucleus, the same energy is always imparted to the reaction products for all slow neutron interactions. Therefore, the resulting pulse height spectrum is a Gaussian-shape peak. Since no gamma-rays are emitted in the ^{6}Li(n,α) reaction, these scintillators can be a promising alternative to ^{3}He counters.

Inorganic scintillators with ^{6}Li have been studied since 50's XX century. Cerium activated lithium silicate glass scintillators have been used for a variety of radiation detection applications since their development in the late 1950's. [72] Also in this time, ^{6}LiI(Eu) was investigated by Murray as fast neutron detector [73]. He showed only poorly defined, broad peaks corresponding to fast monoenergetic neutrons. A detailed study on ^{6}LiI(Eu) were performed by Syntfeld *et al* [74]. In this work, gamma-ray spectrometry as well as response to slow neutrons were tested. The excellent discrimination of slow neutron events from gamma-rays was presented. The next generation of ^{6}Li-based scintillators, e.g. the elpasolite Cs_2LiYCl_6:Ce (CLYC:Ce), was proposed by Delft group in 2004 [75]. More complex scintillators, in the form of scintillation screen with wavelength shifting (WLS) fibers contain the thin sheet of powder of ZnS(Ag)/^{6}LiF mixed together in a binder. Neutrons are captured

by the ^{6}Li and the reaction products excite the light emission from the ZnS(Ag) scintillator, which is subsequently absorbed in an adjacent ribbon of WLS fibers. This configuration is quite flexible and allows to manufacture screens with large active area [76], [IV].

4.3.1 Lithium glass

Amorphous materials activated with Ce^{3+} ions with high ^{6}Li content, referred to as lithium glasses are light (density of about 2.5 g/cm^3), and have fast response (decay time of 75 ns). The main components of a typical Ce^{3+}-activated glasses are SiO_2 (75.6%), Li_2O (11.3%), Al_2O_3 (4.9%), and Ce_2O_3 (7.8%) [77]. Lithium glasses are manufactured in several ^{6}Li-enrichments, as well as in various forms. These glasses are produced by many companies, from which the most popular is Saint Gobain that offers several types of scintillators with different lithium content. For example, for the neutron detection purposes, the GS20 glass, enriched with 95% of ^{6}Li is available [78].

4.3.2 ^{6}LiI(Eu)

Crystalline lithium iodide, with small amount of europium as an activator, was the first lithium-based scintillator for both gamma-ray spectrometry and neutron detection. The emission spectrum of ^{6}LiI(Eu) under X-ray excitation is located at 475 nm, whereas absorption spectrum reveals a sharp cut-off at about 450 nm [73]. Since the maximum of the emission spectrum is peaked just above the self-absorption edge, crystals with large dimensions can reduce total light output of the scintillator and degrade the energy resolution (see appendix C). The first experiments carried out on ^{6}LiI(Eu) by Murray were focused on fast neutron detection, and showed only poor defined broad peaks that were sensitive to temperature change, and the best resolution was achieved in a very low temperature of about -140°C [73].

^{6}LiI(Eu) is extremely hygroscopic, therefore it must be sealed in a hermetical assembly. The density of the crystal is 4.08 g/cm^3. Crystalline structure of ^{6}LiI(Eu) is similar to that of NaI(Tl) with the light output of approximately 35% of that from NaI(Tl) [27]. ^{6}LiI(Eu) has a long decay time of about 1.2 μs, which is characteristics for Eu^{2+} 5d-4f transition. Highly enriched (96% of ^{6}Li) ^{6}LiI(Eu) with thickness of few mm totally absorbs thermal neutrons.

Moreover, it has a good performance characteristics for gamma-ray spectrometry, which makes it a good candidate for hand held devices for simultaneous gamma-ray identification and neutron detection.

4.3.3 CLYC

Since 1997, numerous elpasolites with the general formula: A_2BMX_6 (A = Rb, Cs; B = Li, Na, K; M = Y, La; X = F, Cl, Br, I) doped with rare earth ions as the activators have been studied by the group from Delft [79, 80] and Radiation Monitoring Devices Inc. (RMD) [81] in search for fast and efficient gamma-ray and neutron scintillators. Especially Cs_2LiYCl_6:Ce (CLYC) has demonstrated excellent scintillation properties (the FWHM for 662 keV energy from ^{137}Cs starts from $\sim$3.5% [82], but strongly depends on the size of the sample and Ce^{3+} concentration), thermal neutron detection capabilities via the (n,α) reaction on ^{6}Li (the neutron peak at 3.5 MeV gamma energy equivalent (GEE), and with the FWHM of $\sim$2.9% [82]), as well as fast neutron detection through the ^{35}Cl(n,p) reaction [83, 84].

CLYC is a hygroscopic scintillator with the density of 3.31 g/cm^3 [85]. The effective atomic number (Z_{eff}) of CLYC is 46.4, which is an advantage in comparison to ^{6}LiI(Eu) (Z_{eff} = 52.3) when neutron/gamma discrimination based on pulse height analysis is required. On the other hand, CLYC has lower ^{6}Li content than ^{6}LiI(Eu) by a factor of 1.4, which causes lower intrinsic efficiency for slow neutron detection. Maximum emission wavelength of CLYC is 370 nm, which matches to maximum sensitivity of typical bialkali photomultiplier tubes [85]. The scintillator exhibits core-valence luminescence (CVL) under the irradiation with gamma-rays with a very fast decay time of 2 ns [86]. The CVL is absent under irradiation of alpha-particles, or neutrons, and significantly increases, when the scintillator is cooled below room temperature [87]. This property of elpasolite crystals is used in discrimination between various types of particles via the PSD technique. The presence of chlorine atoms in CLYC gives the opportunity to detect fast neutrons via the ^{35}Cl(n,p) and ^{35}Cl(n,α) reactions, with the threshold of about 1 MeV and 2 MeV neutron energy, respectively.

4.3.4 $LiCaAlF_6$ and $LiSrAlF_6$

Cerium- and europium-doped $LiCaAlF_6$ and $LiSrAlF_6$ (LiCAF and LiSAF, respectively) scintillators have been developed by Tokuyama Corporation for slow neutron detection [88] [III], in which ^{6}Li is contained in the aluminofluoride host matrix [89]. Crystals up to 50 mm in diameter have been grown. The scintillators are characterized by low density of 3 g/cm^3 and low stopping power (Z_{eff}=14-15) for gamma-rays, which allow to discriminate events generated by neutrons from gamma-ray background by pulse height analysis. The scintillator is non-hygroscopic, which is an advantage in comparison to CLYC and ^{6}LiI(Eu).

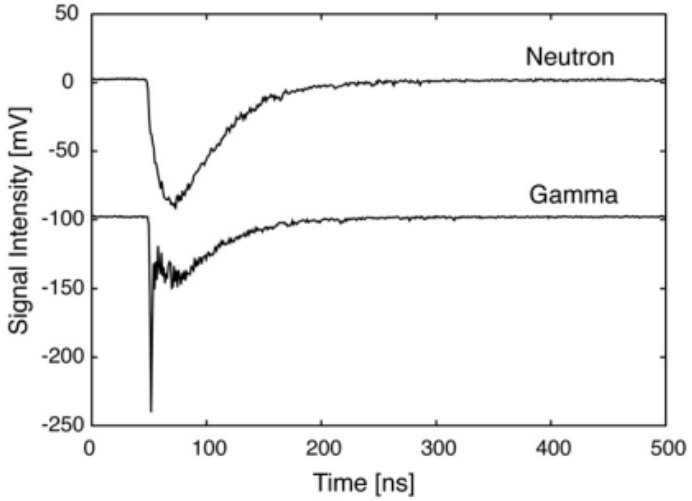

Figure 4.7: *Light pulses from gamma-rays and neutrons recorded with Ce:LiCAF (from [90]).*

Ce:LiCAF has an average decay time of approximately 40 ns, but we can observe fast component in gamma-ray-induced scintillator pulse (see figure 7.3). This property has probably the same origin, as in the case of CLYC (CVL). In the paper of Yamazaki *et al*. [90] authors presented the discrimination between gamma-rays and neutrons based on PSD technique with Ce:LiCAF scintillator.

Eu:LiCAF has slower response of about 1.5 μs, but significantly higher light output than Ce:LiCAF. Additional improvement of light output for Eu:LiCAF and Ce:LiCAF co-doped with Na was presented in [91, 92]. Further development of Eu:LiCAF results in a flexible sheet consisting of small grains of scintillator (hereafter called as *Eu:LiCAF rubber*) [93]. Unique configuration of the detector, in which wavelength shifting fibers are incorporated in the scintillation crystal grains, makes efficient light collection from large to small area

photodetector.

The information about Ce^{3+} and Eu^{2+}-doped LiSAF crystals used as scintillators are presented only in few publications [94–96]. Authors reported that these scintillators have the light output even lower than their LiCAF equivalents. Moreover, LiSAF scintillators are characterized by the opacity in higher Ce^{3+} and Eu^{2+} concentrations, which reduces the emission intensity of the crystals [96].

Figure 4.8: *Flexible sheet of scintillator consisting of LiCAF crystalline grains (400 mm × 400 mm).*

4.3.5 The scintillation screen with light readout by wavelength shifting fibers

Slow neutron detector ^{6}LiF/ZnS(Ag) integrates the neutron capture ^{6}LiF medium and ZnS(Ag) scintillator into a thin screen, which is coupled to a WLS fibers. The scintillation screen is made of granular ^{6}LiF (95% of ^{6}Li) mixed with crystals of ZnS(Ag) in a hydrogenous binder (BC–704). The detector is constructed of subsequent layers of the capture/scintillation screen and the fiber-optic ribbon. The scintillation light is produced in the ZnS(Ag), and is absorbed and reemitted in the fibers, by which is transported to the photomultiplier tube [76]. Figure 4.9 presents the photograph of the detector.

The system based on ^{6}LiF/ZnS(Ag) is commercially available for homeland security

Figure 4.9: *The photograph of a single paddle of the scintillation screen with ^{6}LiF/ZnS(Ag) and WLS (from [IV]).*

applications under the name of *Neuport* and sold by Saint Gobain company in various photomultiplier configurations and sizes [9]. The entire assembly containing the detector with the electronics is contained within a high density polyethylene moderator box. The sensitive area of the typical detector is 1050 cm^2 for a single paddle.

Chapter 5

Experimental techniques in neutron detection

5.1 Light output of scintillators

Scintillation efficiency, known also as a *light output*, is a fraction of kinetic energy lost by a charged particle in a scintillator medium that is converted into fluorescent energy [27]. The remainder of energy is dissipated nonradiatively, usually in a form of lattice vibrations, or heat, and is known under the common term *quenching*. The presence of quenching effects that transfer the energy nonradiatively, reduces the light output of the scintillators. The detailed discussion on the mechanisms of quenching in organic materials is presented in [97]. The light output depends on the composition of the scintillator, as well as on the type and energy of the incident particle. The light output is usually quantified as a number of photons (N_{ph}) produced per 1-MeV gamma-ray energy (in ph/MeV). Practically, we are able to measure the number of photoelectrons (N_{phe}) per energy unit (in phe/MeV), which can be converted into the light output (in N_{ph}) by the convolution of the emission spectrum of the scintillator with the quantum efficiency curve of the photodetector.

In the case of organic scintillator, the light output is often described as a percentage value of the light output of anthracene crystal, which is the brightest from all organic scintillators. For example, the textbook value of the light yield of stilbene is 50% of the anthracene, whereas the light yield of EJ301 liquid scintillator is about 78% [27].

For the purpose of this dissertation, the N_{phe} was measured with the scintillators coupled with silicone grease to Photonis XP5500 spectrometry photomultiplier tube. The parameters of the photomultiplier are collected in table 5.1. The anode signal was sent to the preamplifier, and further sent to the amplifier operated in a bipolar pulse shaping. The shaping time was adjusted to the decay time of the light pulse from the scintillator. In the case of fast organic scintillators, the value was 0.5 μs. The data for N_{phe} estimation were collected and analyzed by Tukan8k acquisition system [98]. High quantum efficiency (37%) and cathode blue sensitivity of 13.6 μA/lmF of the photomultiplier allowed easy registration of relatively large N_{phe}, which is important in order to obtain good quality of the pulse shape discrimination (PSD) that will be discussed in the section 5.2.

Table 5.1: *Photomultiplier XP5500 (56 mm, round tube) basic parameters.*

Description		
window material	borosilicate glass	
photocathode	bi-alkali	
Refractive index at 420 nm	1.54	
Photocathode characteristics		
spectral range	270-650 nm	
maximum sensitivity at	420 nm	
sensitivity	blue	13.6 μA/lmf
	luminous	110 μA/lm

The N_{phe} can be determined using the Bertolaccini *et al.* method [99, 100]. It is based on a comparison of the two spectra registered in a multi-channel analyzer (MCA). The first spectrum is a single photoelectron spectrum recorded with the photomultiplier, whose photocathode is covered from the external light sources. In this configuration, the spectrum is a result of only dark counts due to thermal emission of mostly single photoelectrons from the photocathode. The centroid of the single photoelectron peak (ctr_{1phe}) defines its mean amplitude at the photomultiplier output. The second spectrum is recorded with the scintillator coupled to the photomultiplier, and represents the energy spectrum of gamma-rays from the radioactive source. The source has a characteristic peak (full energy peak), or point (Compton edge), which energy is well known. In most cases the N_{phe} is calculated on the basis of the 662-keV full energy peak from the ^{137}Cs gamma-ray source.

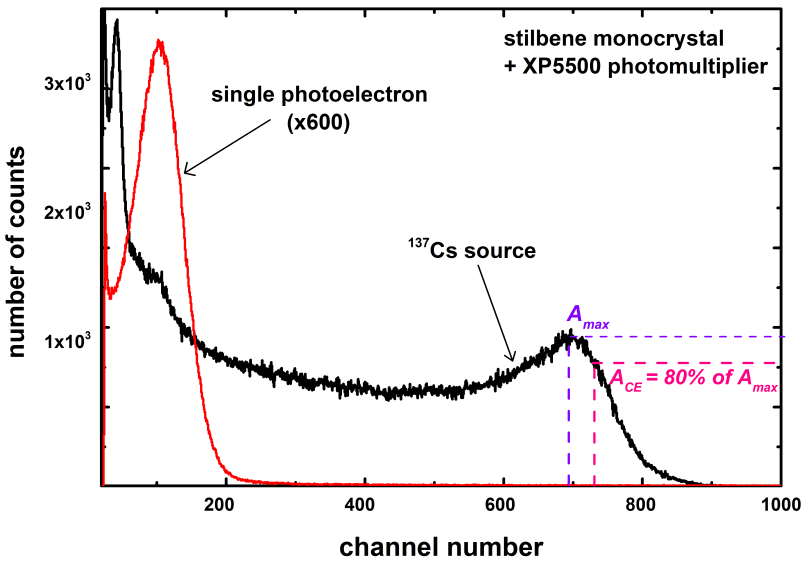

Figure 5.1: *The pulse height spectra recorded with Photonis XP5500 photomultiplier and stilbene crystal used for N_{phe} calculation. The position of the Compton edge (A_{CE}) is estimated as 80% of the upper part of the Compton distribution (denoted as A_{max}) [101, 102].*

Taking into account large differences between the amplitude of a single photoelectron peak, and the amplitude of the full energy peak (or Compton edge) from the ^{137}Cs source, the peak positions are usually recorded with different gains of the spectroscopy amplifier (K). Therefore, the N_{phe} can be calculated in a following way

$$N_{phe}(\text{phe/MeV}) = \frac{ctr_{source}}{ctr_{1phe}} \cdot \frac{K_{1phe}}{K_{source}} \cdot \frac{1}{\text{energy (MeV)}} \tag{5.1}$$

where ctr_{source} is the position of the full energy peak, or the Compton edge for a gamma-ray source, K_{source} is the gain on the amplifier for the source, and K_{1phe} is the gain for the single photoelectron spectrum. In the case of organic scintillators, the effective atomic number is low, therefore we do not observe the full energy peaks, but just the Compton edges, except for gamma-rays of energy below about 100 keV (for example, 59.5-keV line, which is emitted from the excited state of ^{237}Np, and being the decay product of ^{241}Am).

5.2 Pulse shape discrimination in organic scintillators

The PSD in organic scintillators is a key technique used for detection of neutrons in the presence of gamma-ray background, described in the literature over the past 50 years. Organic scintillators are sensitive to several types of radiation, however the pulse height analysis

turns to be insufficient, because the energy deposition for gamma-rays and neutrons can be in the same range. However, the mechanism of the scintillation in organic materials often allows to discriminate gamma-ray and neutron events, because the shapes of the scintillation signals due to excitation by gamma-rays (recoil electrons) are different from those caused by neutrons (recoil protons) [103].

5.2.1 Scintillation mechanism in organic materials

In the case of organic materials, the scintillation process takes place by the transitions between the energy levels in molecules, therefore it can be observed independently of the state of matter of the scintillator [62]. Free electrons, situated on the energy bands of the molecules are responsible for these transitions. If the molecule is in the ground state, two electrons on the same orbital have oppositely directed spins (*Pauli exclusion principle*). If the molecule is excited, the electron spin can have either the opposite (excited singlet state – S_1), or the same direction (excited triplet state – T_1) in relation to the electron on the ground state (S_0). The simplified scheme of the energy levels in organic scintillators is presented in figure 5.2. Radiative transitions, such as fluorescence and phosphorescence are responsible for the scintillations.

Fluorescence is the emission of light during the transition between two singlet states ($S_1 \rightarrow S_0$). This process is very fast (prompt fluorescence with the timescale of below 10^{-8} s) [97]. **Phosphorescence** is the transition between triplet and singlet state ($T_1 \rightarrow S_0$). This process is forbidden, from the quantum mechanics point of view, therefore it is longer in time (from the milliseconds up to seconds) [105]. There are also processes of **delayed fluorescence**, from which **triplet-triplet annihilation** is of importance in neutron detection. This transition occurs when the density of the molecules in triplet states is high, and they can collide with each other. The energy of two molecules is then high enough to excite the singlet state (S_1). Triplet-triplet annihilation leads to the excitation of additional singlet states decaying with the same spectral distribution, as fluorescence, but over a longer and delayed time scale [106].

In the case of organic scintillators for fast neutron detection, both gamma- and neutron-induced pulses contain a short decay (prompt) and a long decay (delayed) fluorescence com-

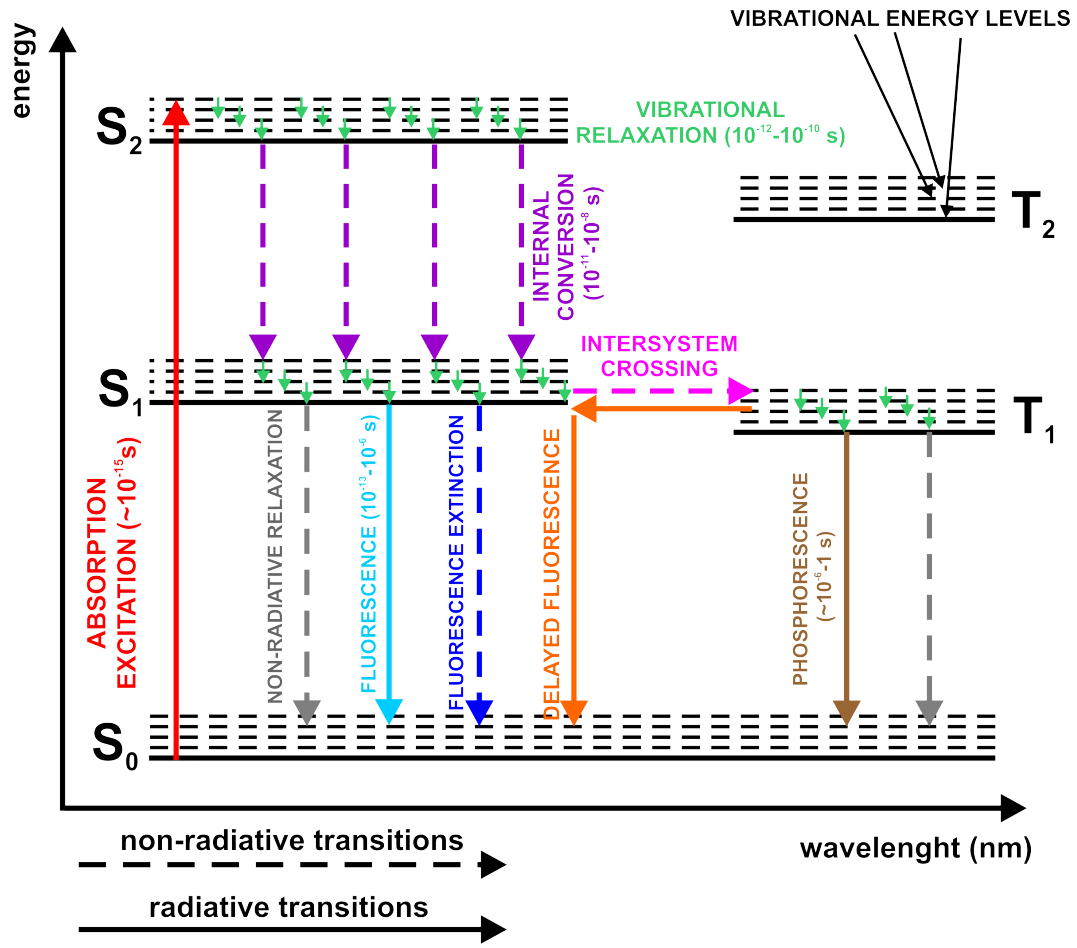

Figure 5.2: *The Jablonski diagram of energy levels in organic scintillators. Radiative and non-radiative transitions are marked (on the basis of [104]).*

ponents. The short range of energetic recoil protons produced from neutron elastic scattering yields a higher concentration of triplet states, than the longer range recoil electrons produced in gamma-ray interaction, leading to the enhanced level of delayed emission in neutron-induced pulses. Therefore, the slow component fraction depends primarily on the rate of energy loss of the exciting particle (*dE/dx*), and it should be larger for particles with higher *dE/dx*. The different proportions of the prompt and delayed components in scintillation pulses produced by neutron and gamma interactions give the basis for the pulse separation used in the PSD techniques. The scintillation pulses recorded for stilbene single crystal when irradiated by alpha, gamma and neutron sources are presented in figure 5.3.

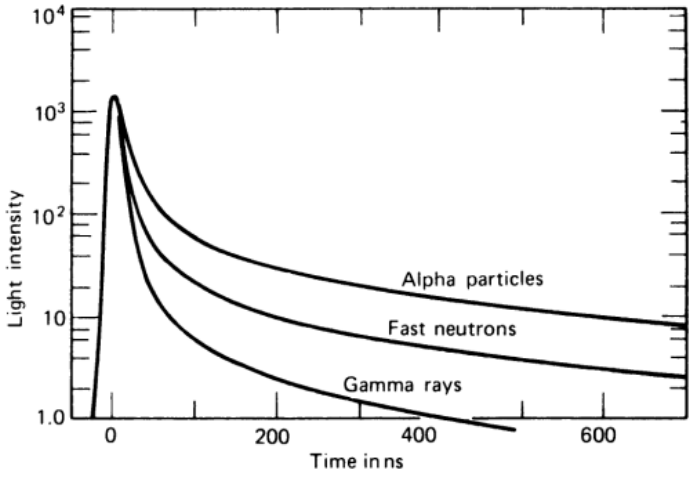

Figure 5.3: *The time dependence of scintillation pulses recorded for stilbene single crystal when excited by the different types of radiation (from [107]).*

5.2.2 Experimental technique

The PSD performance of organic scintillators was tested by the zero-crossing (ZC) method. This technique is based on the time difference between the constant fraction of the fast anode pulse from the photomultiplier tube (generating start signal), and the zero-crossing of the same pulse after passing neutron/gamma discrimination circuit (generating stop signal). This time difference between the start and the stop is referred to as "ZC time" (see figure 5.4). Signals originating from neutrons have longer decay time, and different intensity of the slow component than those from gamma-rays, therefore the ZC for neutrons is later than the ZC for gamma-rays, and these events can be discriminated. The ZC time is determined by the analogue NDE202 module designed in our laboratory [108].

The tested organic scintillators were coupled to the Photonis XP5500 photomultiplier tube. In contrast to fast photomultipliers that are commonly used in detectors working with discrimination [110], the XP5500 was designed for gamma spectrometry with $LaBr_3$, and it has slower response [111]. However, it does not affect the neutron/gamma discrimination, because precision of the method used in the experiment depends mainly on ZC detection of the integrated photomultiplier output pulse. High quantum efficiency and cathode blue sensitivity of 13.6 μA/lmF of the XP5500 allowed easy registration of relatively large number of N_{phe}, which is important in order to obtain good quality of the PSD. The NDE202 module provides fast logic signal from a constant fraction discriminator (CFD) and that of the

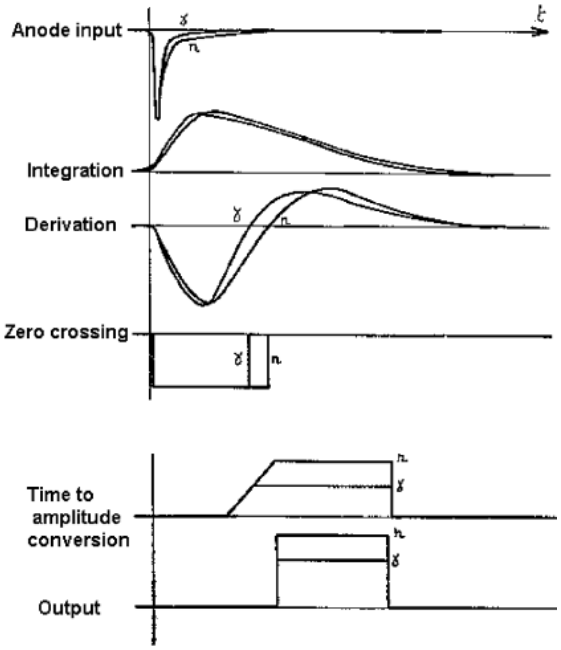

Figure 5.4: *Timing diagram explaining the ZC method (from [109]).*

zero-crossing (ZC) discriminator working on a bipolar shaped input signal. The CFD signal was used as a start for time-to amplitude (TAC) converter, whereas ZC logic signal stopped the TAC. Various intensities of a slow component of the light pulse from gamma-rays and neutrons resulted in the time differences between signals from CFD and ZC discriminators. Additionally, the information about the pulse height of the signal, which corresponds to the energy deposited by the neutron in the scintillator, was collected. The dynode signal was processed by the preamplifier and the amplifier working in a bipolar pulse shaping. Both signals – from the TAC and from the amplifier were recorded in a list-mode by the *Kmax* multiparameter data acquisition system [112]. The graph of the experimental setup is presented in figure 5.5.

5.3 Decay time constant measurements

The decay time of a scintillation light pulse is related to the life-time of the excited states created after the absorption of ionizing radiation. De-excitation of such states takes place in two ways: as a radiative transition followed by photon emission, and as non-radiative transition (quenching). The probability of the de-excitation is the sum of probabilities of both kinds of transitions. Since the life-time of the excited state is inversely proportional to

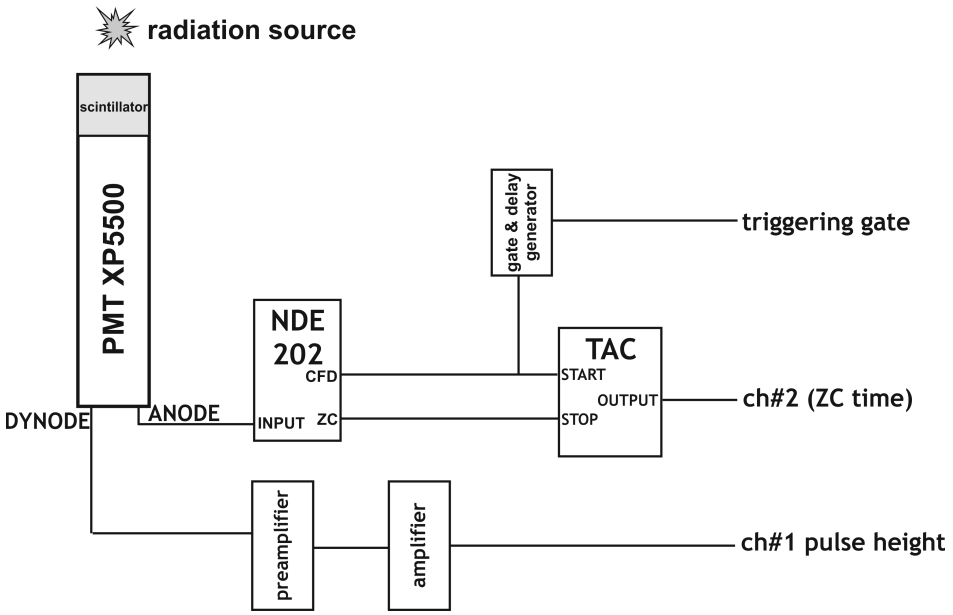

Figure 5.5: *The diagram of the experimental setup used for characterization of the PSD performance of organic scintillators.*

the probability of de-excitation of that state, the decay time of a luminescence induced in the scintillator is defined as

$$\tau \propto \frac{1}{P_r + P_{nr}} \tag{5.2}$$

where P_r and P_{nr} are the probabilities of radiative and non-radiative de-excitation processes, respectively [113].

The time evolution of the light intensity emitted by the scintillator is given by an exponential function

$$I(t) = I(0)exp(\frac{-t}{\tau}) \tag{5.3}$$

where $I(0)$ is the initial intensity [114].

When scintillator exhibits more than one decay component, the light intensity is a sum of the exponential functions

$$I(t) = \sum_i \frac{N_i}{\tau_i} exp(\frac{-t}{\tau_i}) \tag{5.4}$$

where N_i is the number of photons emitted in the *i*-component with the decay time of τ_i [114].

For most scintillators, one component is generated significantly faster than the others, therefore the nomenclature *fast* (or prompt) and *slow* (or delayed) component can be found

in the literature.

The prompt and delayed fluorescence are the main mechanisms that are responsible for radiative transitions in organic materials. The scintillation light pulse, observed at the anode output of the photodetector, has then two main components: the fast with the decay time of few nanoseconds, and the slow component with the decay time of several hundred nanoseconds [27]. Although the majority of the light occurs in the prompt component, the fraction light in the long-lived tail is a consequence of the nature of the exciting particle. This dependence allows to differentiate between various particles that deposit the same amount of energy in the scintillator. The PSD is particularly essential in the case of organic scintillators used as neutron detectors, where discrimination between gamma-ray and neutron induced events is of importance. In our laboratory, the analysis of the light pulse shapes from gamma-rays and neutrons from organic scintillators was performed. The measurements of the decay time constants and estimations of the intensities of particular components for liquid and plastic scintillators were carried out.

5.3.1 Decay time of liquid scintillators

The studies of decay time of liquid scintillators were carried out on $\oslash$5.08 cm $\times$ 5.08 cm cylindrical samples encapsulated in aluminum cells. Some of the samples were capable to detect also slow neutrons through the (n,α) reaction on ^{10}B. They were coupled via a perspex plate to a 7.62 cm timing Photonis XP4312 photomultiplier [115]. The light pulses were recorded using the Boilinger-Thomas single photon method [107]. The set of two photomultipliers - the XP4312 and a fast Hamamatsu R5230 [116] - was placed in the light tight box. The detailed description of the experimental setup is presented in the paper of Szczesniak *et al.* [117]. Scintillators were irradiated by the ^{238}PuBe neutron source. In the case of ^{10}B-loaded liquids, the ^{238}PuBe was placed in a paraffin ball to thermalize the neutrons. The recorded time distribution of the single photons detected in R5320 reflects the scintillation light pulse.

The experiment had three electronic chains:

– slow electronic chain (blue) — selection of the amplitudes corresponding to the single

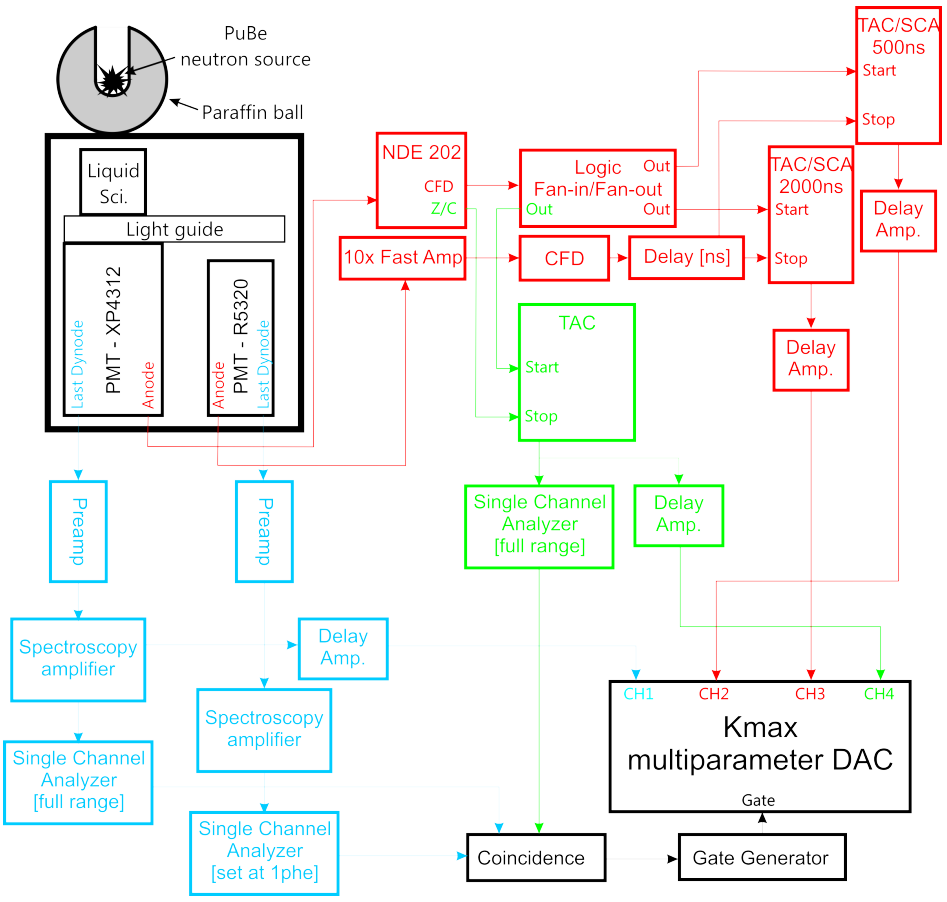

Figure 5.6: *The experimental setup for the light pulse shape measurements using Bolinger-Thomas single photon method and the PSD module.*

photons. Additionally, the pulse height spectrum was collected.

– PSD electronic chain (green) — the time spectrum related to gamma-rays and neutrons. The PSD was done by means of a modified NDE202 module. The electronics for the PSD was described in the previous section.

– fast signal electronic chain (red) — the time spectra of single photons distribution at 500 ns and 2000 ns ranges.

The parameters obtained in the electronic chains were recorded by the *Kmax* multiparameter data acquisition system. Also, a two-dimensional spectrum of the ZC time as a function of pulse height was collected (see figure 7.4). Such plot allows distinguishing gamma-rays from fast neutrons, and further extraction, from the recorded event-by-event mode data, the light pulse shapes characteristics for specific particles. The pulse shape spectrum recorded in the system was a mix of all neutron and gamma-ray events. Therefore, the gates set at ZC time

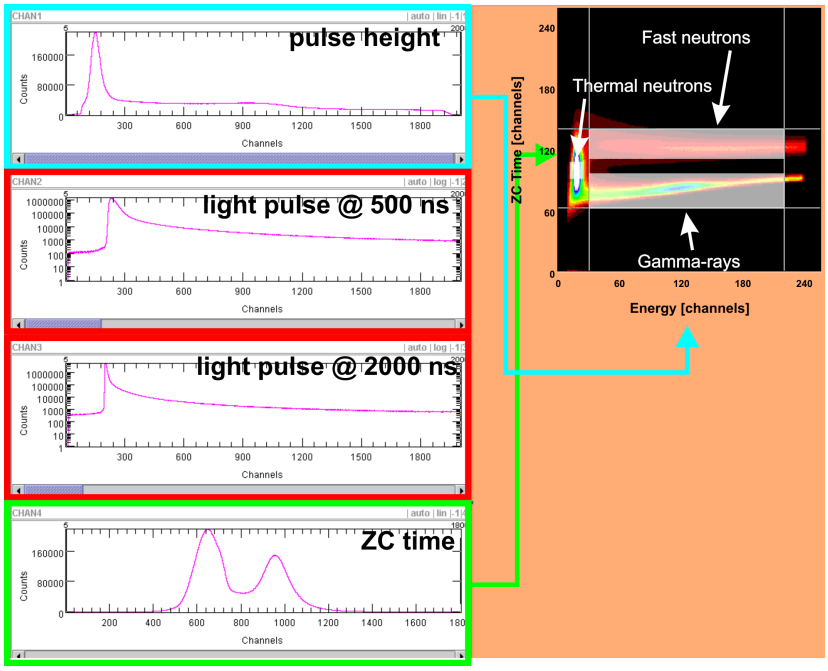

Figure 5.7: *The data acquisition system graphical interface with measured parameters. Two-dimensional plot of ZC as a function of pulse height is presented on the right panel.*

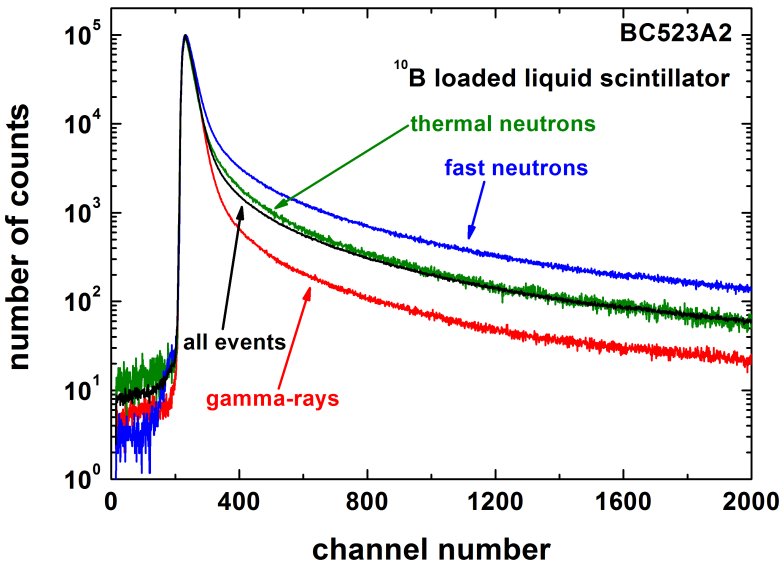

Figure 5.8: *The light pulse shapes for various particles recorded for ^{10}B-loaded BC523A2 liquid scintillator.*

list-mode data allow to extract only the decay shapes that were typical for a given type of events (see figure 5.8).

5.3.2 Light pulses for plastic scintillators (from [VI])

Light pulses for plastic scintillators, similarly to liquids [117], were recorded using the Boilinger-Thomas method. However, the plastics were covered on the sides with the Teflon® tape and coupled to fast Photonis XP20D0 photomultiplier [118]. Two photomultipliers, XP20D0 and Hamamatsu R5320 were placed in both sides of the light-tight tube with the length of approximately 50 cm. Plastic scintillators were also irradiated with the ^{238}PuBe neutron source. Similarly to the setup with liquid scintillators, three electronic chains recorded by the *Kmax* were distinguished (see, section 5.3.1). The only difference was that the time spectra of single photon distribution were recorded at 2000 ns, only.

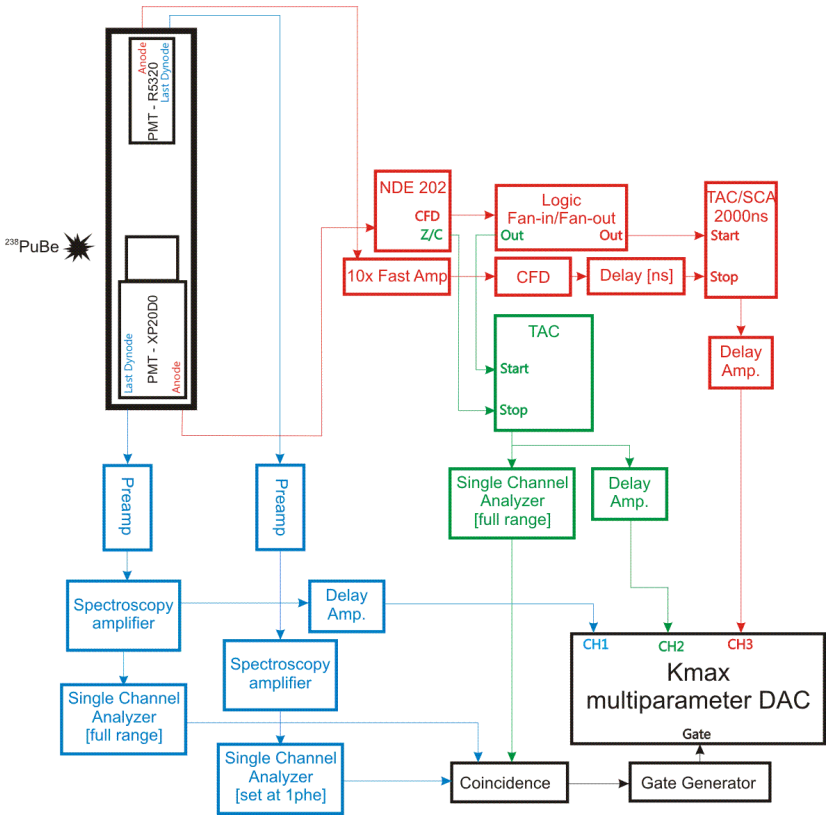

Figure 5.9: *The experimental setup for the light pulse shape measurements with plastic scintillators.*

Figure 5.10 presents an exemplary data acquisition graphical interface together with three measured parameters, recorded with EJ299-34 plastic. To obtain single photons time distribution reflecting light pulse shapes for gamma-rays and neutrons separately, we set the gates at pulse height and ZC time axes. This operation allows to choose only gamma-ray or neutron

events with an energy range from about 500 keVee[1] (upper level, *UL*, see figure 5.10) up to 2 MeVee (lower level, *LL*). In this experiment, voltage applied to the photomultiplier was high (2000 V); therefore, anode signal fed to NDE202 module had high amplitude. The module consists of a fast amplifier, a limiter and a discriminator. The maximum amplitude that can be applied on the discriminator is $\pm$ 1 V. If the amplitude of the anode signal is very high, the fast amplifier is saturated. The saturated signal is fed to the limiter and a discriminator, which causes a shift on a zero level in a ZC pulse. We can observe events above 3 MeV, however, the ZC time is dependent on the energy. The dependence of ZC time on the energy occurs as kinks at high-energy range (above 3 MeV) of the two-dimensional spectrum.

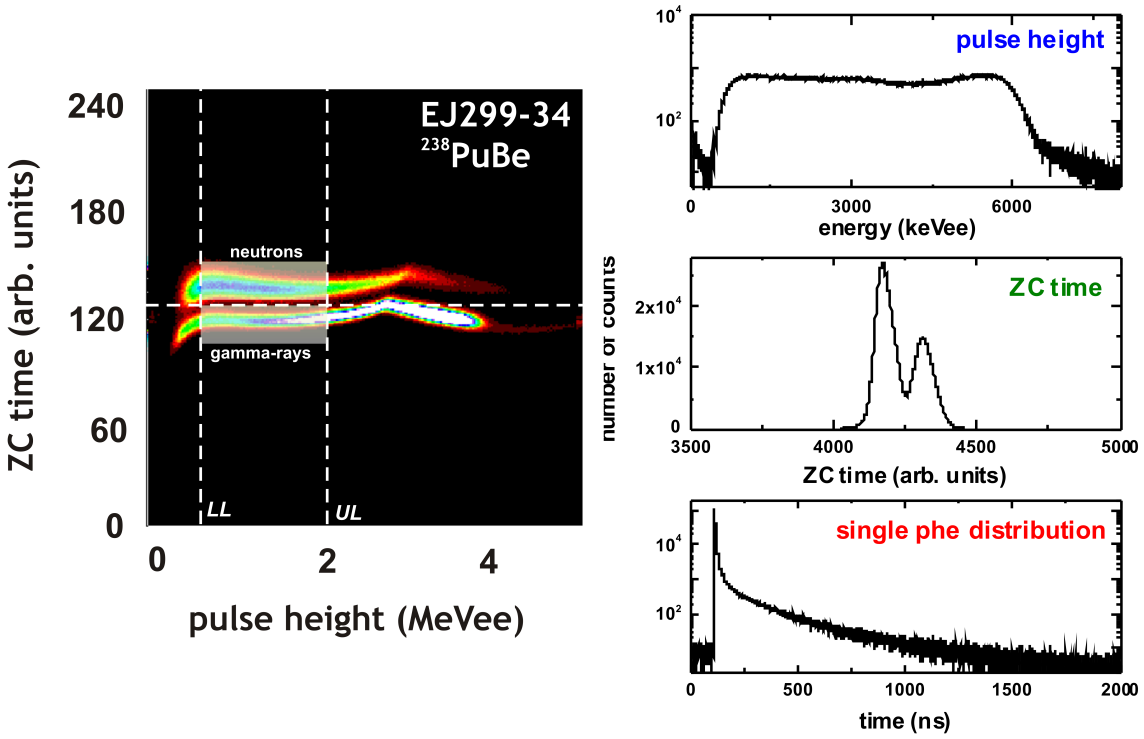

Figure 5.10: *Two-dimensional plot of ZC time as a function of pulse height (left panel) and one-dimensional plots of three collected parameters (right panel) [VI].*

[1] ee-electron equivalent - keVee is defined as amount of energy converted to light, induced by an electron that deposits 1 keV in the scintillator.

5.4 Time-of-flight (ToF) method for calibration of organic scintillators

A small fraction of the kinetic energy lost by a charged particle in the scintillator is converted into fluorescent energy, whereas the remainder is dissipated in the form of heat, or lattice vibrations. The conversion between the deposited energy and emitted light (*scintillation efficiency*) [27] in elastic scattering process in organic scintillators depends on the type and the energy of the incident particle that interacts in the scintillator medium. In the case of organic scintillators, large reduction of the luminous efficiency caused by quenching effects is observed for heavier charged particles, when comparing to the light output for electrons.

The first experimental data together with parameterizations of the light output plot for NE213 liquid scintillator are reported in [119–121]. More recent measurements of the proton response function of NE213 using 0.5 – 6 MeV neutrons from the ^{252}Cf neutron source and the ToF method were presented in [122]. The study of the light generation by monoenergetic neutrons in BC501A together with the simulations, were done by Pozzi *et al.* [123] and Gohil *et al.* [124]. The authors reported a good agreement between analytical calculations, simulations, and measurements of the proton light output of the BC501A. The recoil-proton-response method based on the ToF in conjunction with isotopic sources, such as the ^{241}AmBe, and neutron facilities that produce monoenergetic neutron beams, among others, was demonstrated in many papers, including [125] and [126]. The effectiveness of the ToF technique using LS-301 organic liquid scintillator and a Van de Graaff accelerator was shown by Aspinall *et al.* [127]. Enqvist *et al.* [128] presented the first results of recoil proton light output response functions and detector resolution functions for three EJ309 liquid scintillation detectors with different size. The neutron beam was generated by deuterons from the Van de Graaff accelerator impinging on an ^{27}Al target.

We present an experimental method for acquiring the neutron responses of various liquid organic scintillators at various energies of recoil protons using a ToF technique in conjunction with a DT neutron generator. The study of a high-flashpoint ^{10}B-loaded EJ309B5 showed the thermal neutron peak at approximately 100 keVee [VIII], which is significantly higher than for the xylene-based liquids, such as BC523A, BC523A2, and EJ339A2 ($\sim$60 keVee, [129]). The observed differences suggest different calibration characteristics of high-

flashpoint liquid scintillators than those of NE213, or BC501A.

5.4.1 The experimental method

The technique is based on the DT generator and two organic scintillators - a START detector (one the tested liquid scintillator - ⌀5.08 cm × 5.08 cm EJ301, EJ309, or EJ309B5) and a STOP detector (⌀4.00 cm × 5.00 cm BC408 plastic scintillator). The diagram of the geometry of the experiment is presented in figure 5.11. The maximum neutron flux generated with the DT generator, used in this study, is 3×10^8 n/s. Deuterium ions are accelerated towards a titanium target (200 μm thick), in which a mixture of 50% deuterium and 50% tritium is implanted. The dominant reaction is the DT process, in which neutrons with the energy of approximately 14 MeV are emitted. The details of the kinematic of the DT reaction are described in appendix B. In our experiment, deuterons are accelerated to the energy of 80 keV, and the resulting neutron flux is 2×10^7 n/s. The angle θ between the direction of the

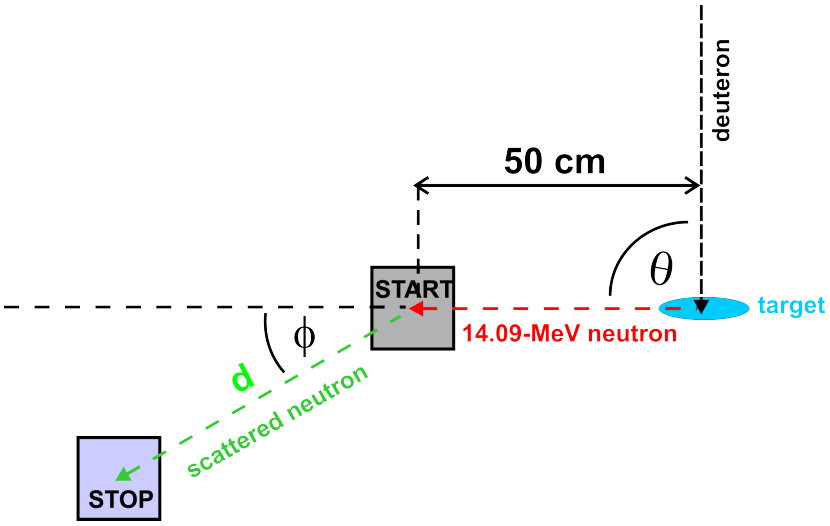

Figure 5.11: *The geometry of the experiment.*

deuteron beam and emitted neutron is 90° (see figure 5.11). The neutron energy varies with the angle θ - for 90° E_n = 14.09 MeV. The uncertainty of the incoming neutron energy (ΔE_n) is caused by two main factors:

– the slowing-down process of a deuteron in the target: the range of 80-keV deuterons in the titanium is approximately 0.6 μm. Simplifying that the deuteron loses the uniform fraction of energy per unit of path until complete stop, the average energy loss is the

half of the initial energy. This approximation leads to the energy dispersion of 20 keV at the angle = 90°.

– The finite size of the START detector: due to the finite size of the detector we observe neutrons emitted from the target at angle that can differ from 90° up to ± 0.05°. This fact introduces the spread of the incoming neutron energy of 0.1 keV.

A neutron with an energy of 14.09 (± 0.02) MeV scatters on a proton in a liquid-scintillator medium. Afterward, the single-scattered neutron is detected in the STOP detector. The fixed angle between the centers of the START and STOP detectors (the angle ϕ, see figure 5.11) determines the energy of scattered neutron – $E_{n'}$ – from the equation

$$E_{n'} = E_n cos^2\phi. \tag{5.5}$$

The scattered neutrons registered in the experimental setup at a fixed scattering angle have some finite energy spread. We determined the ToF of the scattered neutron to calculate $E_{n'}$ more precisely:

$$E_{n'} = \frac{d^2 m_n}{2(ToF)^2} \tag{5.6}$$

where d - is the distance between the centers of the START and STOP detectors, and m_n - is the neutron mass. The neutron energy of 14.09 MeV is non-relativistic, therefore the classical mechanics can be applied.

The uncertainty of scattered neutron energy ($\Delta E'_n$) is caused by:

– the dimension of the START and STOP detector: the distance that a scattered neutron travels between the detectors is in the range of 1997.5 – 2002.5 mm. Therefore, the ($\Delta E'_n$) is, depending on the E'_n, in the range of 6-9%.

– the time resolution of the system: this value was measured directly and was found to be 1 ns (see 5.4.2).

The recoil proton energy (E_r) deposited in the liquid scintillator can be calculated from the equation

$$E_r = E_n - E_{n'} \tag{5.7}$$

By changing the position of the STOP detector, we scan different scattering angles, which translates to different proton recoil energies.

All organic scintillators contain carbon and hydrogen. However, collisions between the incoming neutrons and carbon nuclei generate very little light. In the extreme, a head-on collision, a 14-MeV neutron can transfer 100% of the energy to a hydrogen and 28.4% of the energy to a carbon nucleus. Pulses from collisions involving carbon only are very small when compared to those created on hydrogen; therefore, the scattering on carbon was not addressed in this experiment. We also assumed that each neutron collides only once in the START detector. Additionally, the ToF method eliminates the events arising from scattering on carbon only.

5.4.2 The electronics used in the experiment

ToF measurements

The ToF technique is used to determine the energy of scattered neutrons. While using this method, the START signal was obtained from the tested liquid scintillator, whereas the STOP signal was obtained from the BC408 plastic scintillator. The START detector was placed at a distance of 50 ($\pm$ 1) cm from the DT generator. Both scintillators were coupled to Photonis XP20D0 fast photomultipliers to assure excellent time resolution. The anode signals from the detectors were fed into a five-channel CFD. The time difference between the START and STOP signals was measured with a TAC. The logic signals from the outputs of the CFD were also fed to a coincidence module that produced a gate to trigger a *Kmax* acquisition system. Additionally, a PSD technique was applied to separate neutrons from gamma-rays. The PSD was performed by means of the ZC method. The diagram of the experimental setup is presented in figure 5.12. Three parameters were acquired:

- pulse height for the START detector,
- ZC time,
- time difference between the arrivals of the START and STOP signals (see equation 5.8), from which the ToF is calculated.

The ToF of scattered neutrons is defined as a result of the following sum:

$$ToF = x + t_\gamma \tag{5.8}$$

where x - is the time difference between the arrivals of the START and STOP signals, and t_γ is the ToF of a gamma-ray travelling between the two detectors. In the case of the distance of 2 m, the t_γ is 6.67 ns.

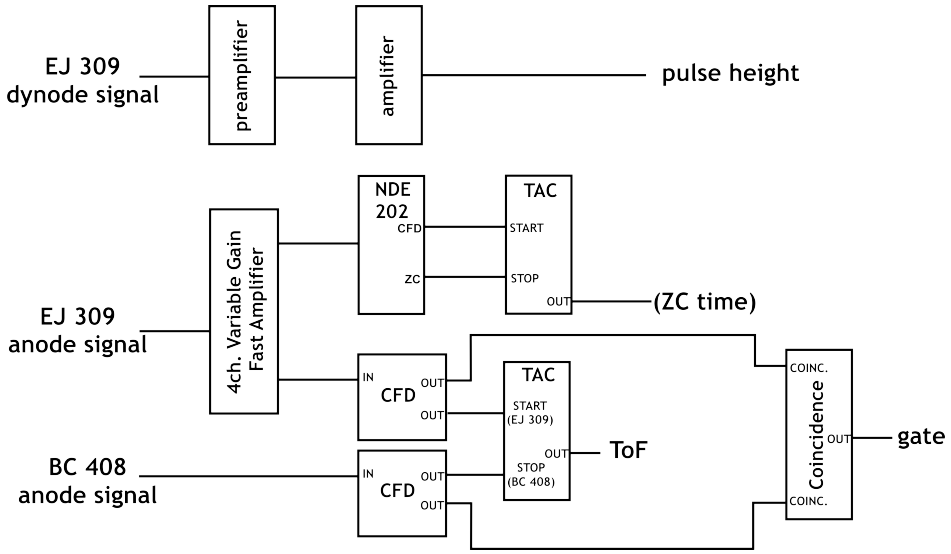

Figure 5.12: *The diagram of the experimental setup.*

Time resolution of the system

The time calibration of the system was performed in coincidence with 511-keV annihilation photons from a ^{22}Na gamma-ray source. The spectra measured for ^{22}Na and the time spectra of the coincidences in both detectors measured for the D–T generator are presented in figure 5.13. The time resolution of the system was approximately 1 ns. This value is crucial in determining the energy of a detected neutron.

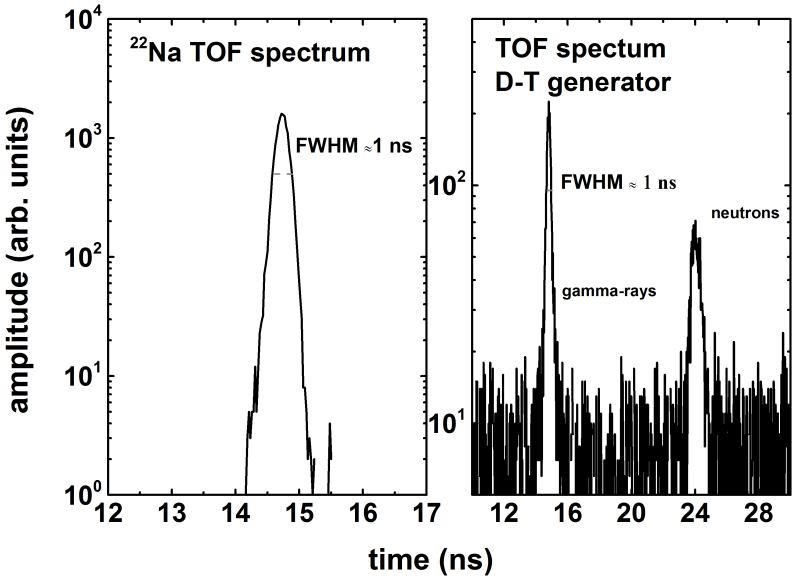

Figure 5.13: *Timing spectra measured using the EJ301 liquid scintillator.*

Chapter 6

Results of the study on fast neutron detectors

6.1 Organic liquid scintillators

Liquid scintillators can be considered as the alternative detectors to the ^{3}He proportional counters in the crisis of ^{3}He supply. They are sensitive to fast neutrons, which are mainly detected via the elastic scattering on hydrogen and carbon, and can be used in the presence of a gamma-ray field when the PSD techniques are applied to discriminate pulses generated by different incident particles. Moreover, ^{10}B-loaded liquid scintillators are sensitive to neutrons of energies down to thermal without using additional moderator, because thermal neutrons are captured by ^{10}B in the scintillation medium, leading to the (n,α) reaction. Liquid scintillators provide the alternative to other detectors in applications, where large volumes are required, because they can be produced in cells, or storage containers from less than 1 liter up to several thousand liters.

The tests of organic liquid scintillators, presented in this dissertation, covers the measurements of basic scintillation performance, such as light output, as well as neutron/gamma discrimination performance, decay time of the light pulses from gamma-rays and neutrons, efficiency to neutrons, and suppression of gamma-ray events. Liquid scintillation cells tested in our laboratories are 5.08 cm in diameter and 5.08 cm in height cylinders, but some of the tests have been performed also with larger samples.

6.1.1 Light output

The N_{phe} measured for organic liquid scintillators are listed in table 6.1. The differences between the values of the N_{phe} encountered in our papers are due to the uncertainty of the Compton edge estimation, as well as due to using different photomultiplier tubes. In the previous papers, i.e. Nassalski *et al.* [130] authors claimed that the Monte Carlo simulations performed by Dietze and Klein deduced the position of the Compton edge as 66% of the upper part of the Compton distribution. However, in the work of Swiderski *et al.* [102] the coincidence measurements indicated that the position of the Compton edge is at the level of 80%. Liquid scintillators have the N_{phe} at the level of approximately 2000 phe/MeV, which

Table 6.1: *The number of photoelectrons per energy unit (phe/MeV) measured for various organic liquid scintillators, recorded with XP5500 photomultiplier tube (see table 5.1 in chapter 5.)*

scintillator	**dimension**	**N_{phe}** (phe/MeV)	**reference**
BC501A	⌀5.08 cm × 5.08 cm	1650	[I]
		1780[1]	[130]
EJ301	⌀5.08 cm × 5.08 cm	2540	[VIII]
EJ309	⌀5.08 cm × 5.08 cm	2600	[VIII]
EJ309B5 (liquid + ^{10}B)	⌀5.08 cm × 5.08 cm	1850	[VIII]
BC532A (liquid + ^{10}B)	⌀5.08 cm × 5.08 cm	1540	[VIII]
BC532A2 (liquid + ^{10}B)	⌀5.08 cm × 5.08 cm	2450	[VIII]
EJ339A2 (liquid + ^{10}B)	⌀5.08 cm × 5.08 cm	2190	[VIII]

is a typical value for organic materials. Moreover, loading with ^{10}B atoms does not affect on the light output of the scintillator.

6.1.2 The PSD performance of liquid scintillators

By means of organic scintillators for neutron detection we may observe events generated by Compton scattering of gamma-rays and fast neutrons elastically scattered on protons. Figure 6.1 presents a two-dimensional plot of ZC time as a function of pulse height mea-

[1]Recorded with Photonis XP5200 photomultiplier tube with blue sensitivity of 13.3 μA/lmF.

sured with BC501A liquid scintillator irradiated with the ^{137}Cs and the ^{238}PuBe sources, and recorded by *Kmax* acquisition system. The events generated by two different particles are separated on ZC time axis, because recoiled protons produce more intense slow components in scintillation than electrons, which leads to a larger time difference between signals from CFD and ZC outputs. The pulse height scale was calibrated using several gamma-ray sources (see table 6.2). The results of the calibration is given in keVee, or MeVee energy units.

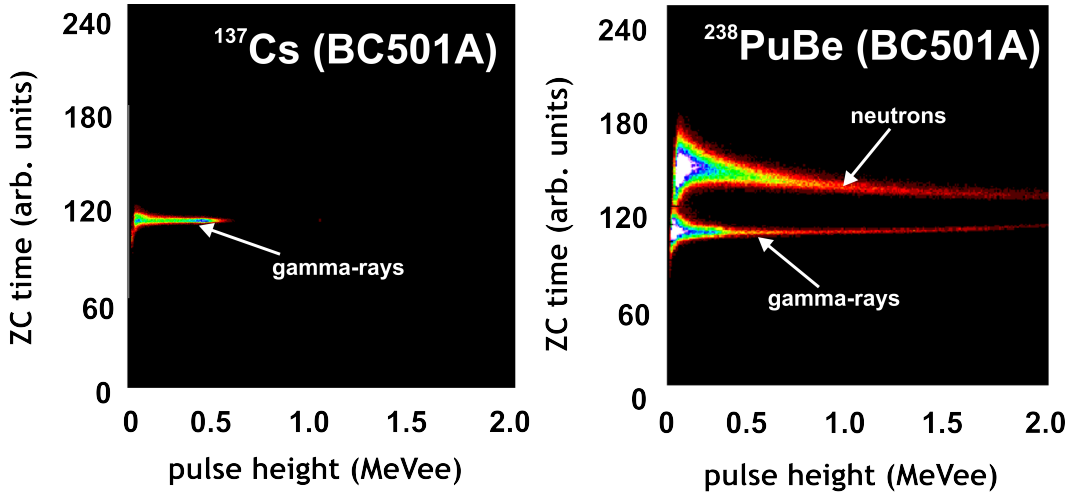

Figure 6.1: *Examples of experimental PSD two-dimensional patterns recorded by Kmax system obtained under irradiation of BC501A liquid scintillator with the ^{137}Cs and the ^{238}PuBe sources.*

Table 6.2: *Gamma-ray energies (E_γ) emitted by the calibration sources together with the energies of the Compton edges (E_{CE}).*

gamma-ray source	E_γ (keV)	E_{CE} (keV)
^{241}Am	59.5	11.2
^{22}Na	511.0	340.7
^{22}Na	1274.5	1061.7
^{137}Cs	661.7	477.4
^{60}Co	1173.2	963.4
^{60}Co	1332.4	1118.1
^{238}PuBe[2]	4438.0	4196.4

[2]The ^{238}PuBe also emits gamma-rays (see section 3.2 in chapter 3).

Figure of Merit

To evaluate the PSD performance of the tested liquid scintillators, narrow energy cuts were projected onto ZC time axis (see figure 6.2), and Figure of Merit (FoM) of Gaussian-shaped peaks was calculated. The FoM can be defined as:

$$FoM = \frac{S_{s\gamma}}{FWHM_n + FWHM_\gamma} \tag{6.1}$$

where $S_{n\gamma}$ is the separation between the gamma-ray and neutron peak, and $FWHM_n$ and $FWHM_\gamma$ are the full width at half maximum for neutron and gamma-ray peak, respectively [27].

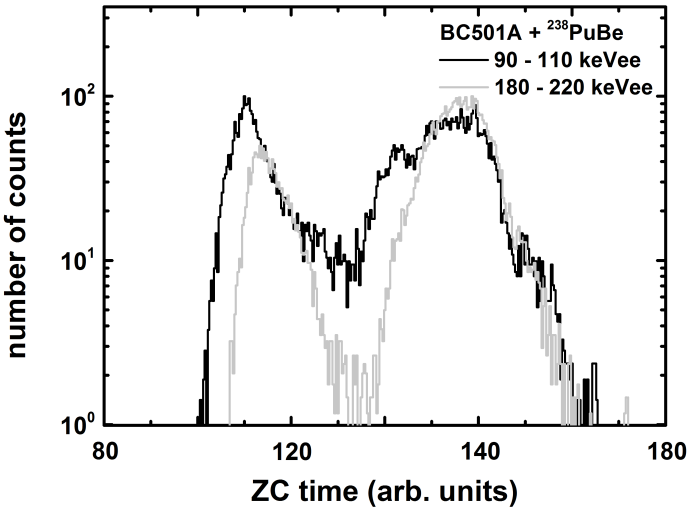

Figure 6.2: *ZC time spectra measured with BC501A liquid scintillator under irradiation of the ^{137}Cs and the ^{238}PuBe.*

EJ301 versus EJ309

The most common liquid scintillators for fast neutron detection, which are currently available on the market are EJ301 [131] and its equivalent BC501A [132]. They have the same composition as NE213, which is known since the seventies of the XX century and was manufactured by Nuclear Enterprise company. The composition of these scintillators (the presence of toxic and flammable xylene as a solvent) limits their usage in harsh environments, and in homeland security applications, where the safety of the public is a priority.

The liquid scintillator that can be used in environmentally difficult conditions is EJ309 with the flash point of 144 °C. EJ309 provides just slightly poorer PSD characteristics than EJ301 (see figure 6.3), but possess a number of chemical properties giving it an advantage over other liquid scintillators for use in harsh environments.

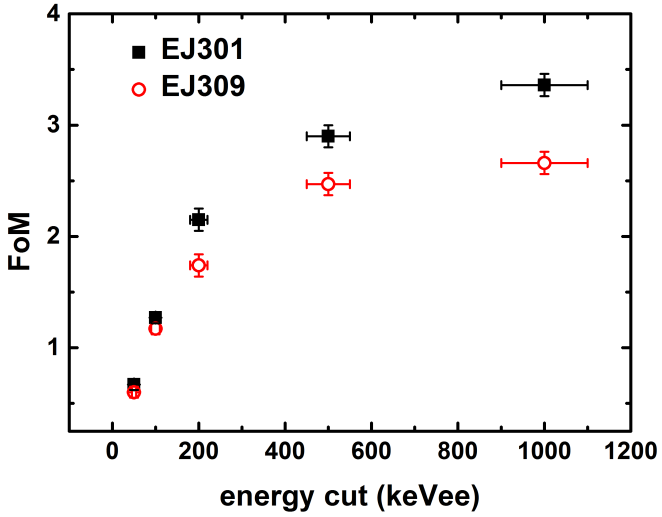

Figure 6.3: *FoM calculated for EJ301 and EJ309 liquid scintillators.*

PSD performance for various sizes of EJ309 liquid scintillation cells

We have tested the PSD characteristic of three sizes of cylindrical EJ309 liquid scintillator cells [I]:

- 5.08 cm in diameter and 5.08 cm in height coupled to Photonis XP5500 photomultiplier,
- 7.62 cm in diameter and 7.62 cm in height coupled to ETL9305 photomultiplier,
- 12.70 cm in diameter and 12.70 cm in height coupled to Photonis XP4512 photomultiplier.

The FoMs for the tested samples are collected in figure 6.4. We observe the decrease of FoM with increasing the volume of the cell. This fact is connected with different quantum efficiency of the photomultipliers used in the measurements (35% at 420 nm for XP5500, 30% for ETL9305 and 24% for XP4512), which subsequently decreases the output pulse,

and lower the precision of the PSD method. Moreover, in most of photomultiplier tubes, an outer zone of the cathode can be made inactive by defocusing the electrons from it, so that they are not collected by the first dynode. Therefore, light collection from photomultiplier tubes that have the same dimension, as scintillator is worse than for slightly larger in diameter photomultipliers.

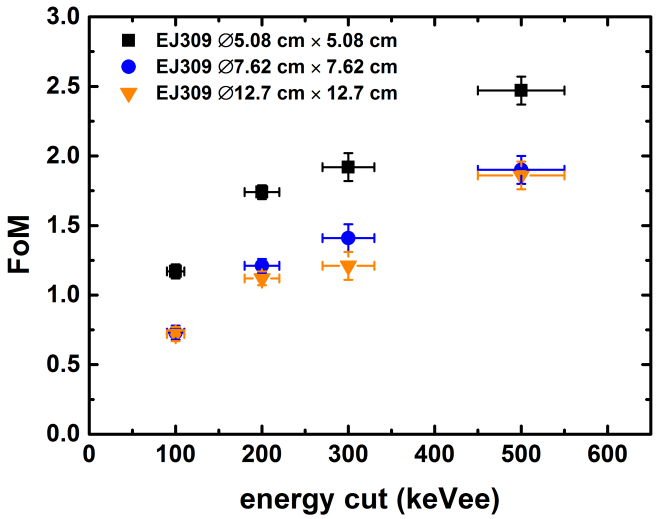

Figure 6.4: *The FoM calculated for different cell sizes of liquid scintillator EJ309.*

6.1.3 Light pulses from liquid scintillators

Light pulses from organic liquid scintillators were recorded with several samples of 5.08 cm in diameter and 5.08 cm in height cylindrical cells. Some of the samples were loaded with ^{10}B to extend the neutron sensitivity to thermal energies. Most of the manufacturers of liquid scintillators provide the information about the fastest component [133, 134], or the mean decay times of the three components [60, 131]. The accurate knowledge about the particular components of the light pulses originating from gamma-rays and neutrons allows improving neutron/gamma discrimination. This information is used both in analogue, and digital PSD algorithms.

The measurements were performed with two different time ranges to determine the slow component from the time spectrum recorded at 2000 ns TAC range, where fast and medium component was determined from the time spectrum measured at 500 ns TAC range (see section 5.3.1 in chapter 5). Liquid scintillators are encapsulated within aluminum cells, so the

perspex light guide plate was placed between the photomultiplier and scintillator output window. Although the Hamamatsu photomultiplier was not directly coupled to the light guide to minimize the number of detected photons, the background was still quite high. Therefore, this experimental setup did not allow measuring light pulses with required low background level, and additional background exponential component was fitted at 2000 ns TAC range.

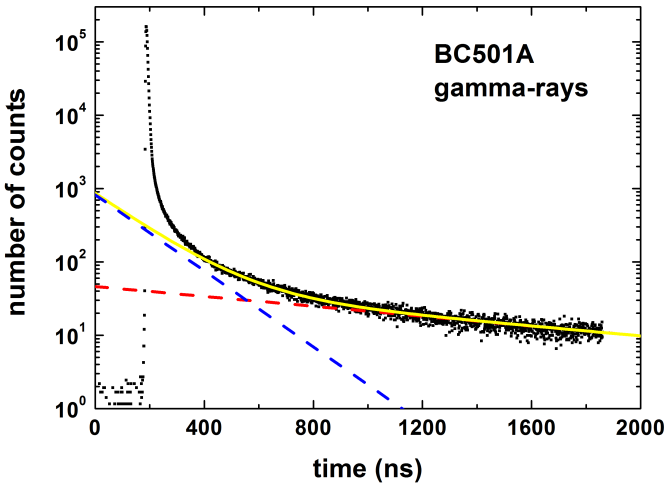

Figure 6.5: *The exemplary light pulse shape recorded for BC501A gated for gamma-ray events at 2000 ns time range.*

The fitting procedure of light pulse shapes for gamma-rays and neutrons, recorded at 500 ns and 2000 ns time ranges, are presented in details in [117]. The final light pulses recorded with liquid scintillators are approximated by three exponential functions with the components: fast-τ_1, medium-τ_2, and slow-τ_3, as well as the function with additional, background component-τ_4 (see table 6.3). The sum of all the components determined the final fit, and representation of the light pulse shape for a given type of particle detected in a scintillator.

The results obtained with BC501A are in good agreement to that from NE213 (fast component = 3.16 ns, medium component 32.3 ns [135]). However, long component is significantly shorter than reported in [135] (270 ns). Faster and less intense long component (τ_3), recorded in our experiment, is caused by presence of additional fourth, background component. In the case of gamma-ray pulses for classical liquid scintillators, short component is dominant and exceeds 80% of the total intensity. On the other hand, fast neutron events significantly enhance medium and slow components.

Table 6.3: *Decay times (τ) and the light intensities (*I*) for all tested liquid scintillators (from [117].*

		fast component		medium component		slow component		background component	
scintillator	particle	τ_1 (ns)	I_1 (%)	τ_2 (ns)	I_2 (%)	τ_3 (ns)	I_3 (%)	τ_4 (ns)	I_4 (%)
EJ301	gamma-rays	4.1 ± 0.4	**89**	32 ± 3	**7**	160 ± 20	**3**	1870 ± 190	**2**
	neutrons	5.2 ± 0.5	**51**	32 ± 3	**23**	130 ± 10	**17**	510 ± 50	**9**
EJ309	gamma-rays	3.7 ± 0.4	**80**	31 ± 3	**10**	140 ± 10	**7**	790 ± 80	**3**
	neutrons	4.8 ± 0.5	**46**	32 ± 3	**24**	140 ± 10	**20**	620 ± 60	**11**
BC501A	gamma-rays	4.0 ± 0.4	**83**	32 ± 3	**7**	170 ± 20	**5**	1290 ± 130	**5**
	neutrons	5.0 ± 0.2	**54**	22 ± 3	**21**	180 ± 15	**25**	–	–
BC523A	gamma-rays	4.2 ± 0.4	**91**	31 ± 3	**6**	150 ± 10	**2**	970 ± 100	**1**
	thermal neutrons	4.6 ± 0.5	**72**	33 ± 3	**18**	220 ± 20	**10**	–	–
	fast neutrons	5.0 ± 0.5	**62**	35 ± 3	**19**	150 ± 10	**12**	640 ± 60	**7**
BC523A2	gamma-rays	4.4 ± 0.4	**88**	32 ± 3	**7**	140 ± 10	**3**	870 ± 90	**6**
	thermal neutrons	5.0 ± 0.5	**65**	33 ± 3	**21**	160 ± 20	**11**	1400 ± 140	**3**
	fast neutrons	5.4 ± 0.5	**57**	35 ± 3	**20**	140 ± 10	**14**	630 ± 60	**9**
EJ309B5	gamma-rays	4.2 ± 0.4	**73**	35 ± 4	**12**	160 ± 20	**10**	880 ± 90	**6**
	thermal neutrons	4.9 ± 0.5	**49**	35 ± 3	**26**	160 ± 20	**18**	890 ± 90	**7**
	fast neutrons	4.9 ± 0.5	**42**	35 ± 3	**22**	150 ± 20	**19**	770 ± 80	**17**
EJ339A2	gamma-rays	4.3 ± 0.4	**90**	34 ± 3	**7**	130 ± 10	**2**	2510 ± 250	**1**
	thermal neutrons	4.8 ± 0.5	**70**	31 ± 3	**20**	120 ± 10	**9**	–	–
	fast neutrons	5.3 ± 0.5	**63**	35 ± 4	**21**	130 ± 10	**13**	1150 ± 120	**2**

The light pulses recorded with ^{10}B-loaded liquid scintillators shows that fast component is dominating for gamma-ray events, covering approximately 90% of the emitted light (with the exception of EJ309B5, where the fast component is 73% of the total light intensity), similarity to classical liquid scintillators. The events originating from fast and thermal neutrons have almost identical medium components for all ^{10}B loaded liquids. The intensity of fast components is reduced up to about 70% for thermal energies and 60% for fast neutrons. The only exception is again EJ309B5, where the fast component is reduced to 49% for slow neutrons and about 42% for fast neutrons.

6.1.4 Suppression of gamma-ray sensitivity for liquid scintillators

EJ309 liquid scintillator is one of the candidates as an alternative to the ^{3}He counter in homeland security applications, because it is characterized by a high flash-point, high neutron detection efficiency and low cost. EJ309 has also a good PSD performance, significantly better than the plastics, and just slightly worse than EJ301. However, all liquid scintillators have relatively high gamma-ray sensitivity. Although it is possible to discriminate events induced by fast neutrons from those induced by gamma-rays, some gamma events may appear in neutron detection window, especially when the detector is placed in a high intensity gamma-ray field. These misidentified events are usually due to the pile-up of gamma-ray pulses.

The criterion for detectors applied for homeland security purposes is their insensitivity to gamma-rays with simultaneously high neutron detection efficiency. The quantity describing the insensitivity of the detector to high intensity gamma-ray field is defines as the *intrinsic gamma-neutron detection efficiency* ($\varepsilon_{int\gamma n}$). There are three relevant documents from which the requirements for gamma-ray sensitivity of neutron detectors can be obtained [136–138]. Generally, on the basis of these requirements, and taking into account the exposure rate of commercially available sources for medical purposes (radiopharmaceutical are the main sources of gamma-rays at the border crossings), the dose rate of 100 μSv/h (10 mR/h) at the detector's surface with no neutron source present, is used. A tolerable count rate must also be defined. Therefore, the $\varepsilon_{int\gamma n}$ specifies the response of a neutron detector to the presence of a gamma-ray field when no neutron source is present. This value is the net number of

gamma-rays misidentified as neutrons, divided by the number of photons striking the front facial area of the detector (including the moderator). In the ideal case, the $\varepsilon_{int\gamma n}$ is zero. However, it is required that a neutron detector for homeland security applications in RPMs should be characterized by the $(\varepsilon_{int\gamma n}) \leqslant 10^{-6}$ [139].

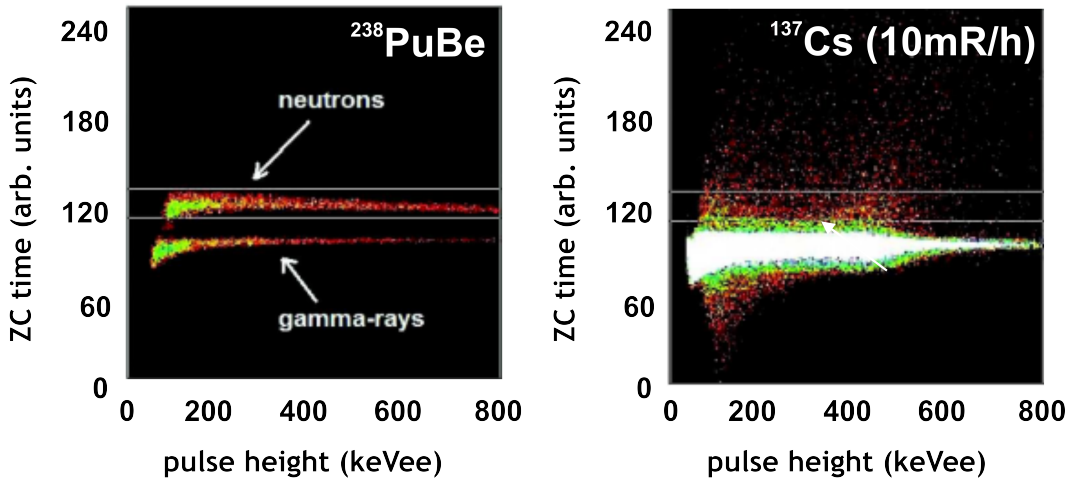

Figure 6.6: *Two-dimensional plots of ZC time as a function of pulse height from EJ309 irradiated with the ^{238}PuBe (left panel) and an intense ^{137}Cs source (right panel).*

The ⌀5.08 cm × 5.08 cm EJ309 scintillator was coupled to Photonis XP5500 photomultiplier. A ZC method was applied to the anode signal to discriminate events from gamma-rays and neutrons by means of an analogue PSD module equipped with pile-up rejection (PUR) circuit [140]. The setup for ZC technique consists of a constant fraction discriminator (CFD, Philips 715), where the anode signal is fed, creating a start signal to the TAC. A stop signal is created by the PSD module, when the bipolar-shaped signal crosses the zero level. The time differences between start and stop are converted into the amplitude in the TAC and sent to the *Kmax* acquisition system, as channel 2. The signal from the dynode is fed to the preamplifier and the amplifier, and gives the information about the amplitude of the incoming signal (channel 1).

The measurements are carried out in an intense field of gamma-rays from the ^{137}Cs source yielding 10 mR/h at the detector's surface. Several configurations of shielding materials (lead, tin and copper) are used for reduction of gamma-ray field, as well as PUR circuit was applied to suppress gamma-ray induced pile-up events in neutron detection window.

The ^{238}PuBe neutron source was used to define neutron detection window (see figure 6.6,

left panel), which was placed between 110 and 130 channel in ZC time axis. The gamma-ray rejection problem occurs when the scintillator is irradiated with an intense ^{137}Cs source (see figure 6.6, right panel). Large number of gamma-ray events occurs in the neutron window, being a result of pile-ups in the electronics ($\varepsilon_{int\gamma n} \approx 3.9 \times 10^{-4}$). Using the PUR circuit with the dead time of 10 ns (the pile-up events occurring within 10 ns time period are not rejected) the total number of pile-up events decreases, but the majority of rejected events are located above 130 channels. As a result, the $\varepsilon_{int\gamma n}$ is reduced by 25% only. The same conditions applied to the ^{3}He counter gave the results at the level of 10^{-7}, where the relative neutron detection efficiency was at the level of 1.25 between the liquid scintillator and the ^{3}He detector.

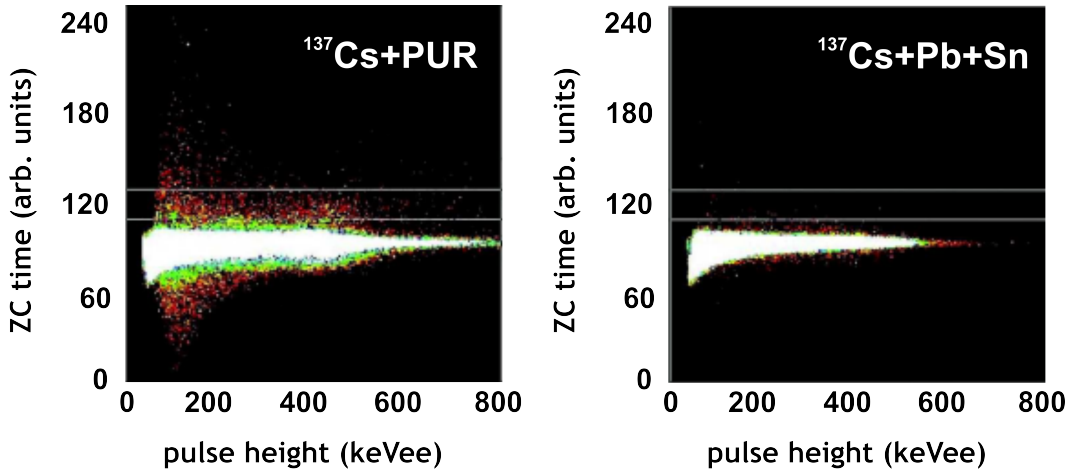

Figure 6.7: *Two-dimensional plots of ZC time versus pulse height from EJ309 irradiated with an intense ^{137}Cs with PUR switched on (left panel) and with shielding materials (right panel).*

Further reduction of gamma-ray field was done by using various shielding materials around the liquid scintillator cell (see figure 7.5, right panel). First, 50 mm lead brick was put at the front and 10 mm lead cylinder was placed around the detector. In this case, the $\varepsilon_{int\gamma n}$ was reduced by a factor of 20, where the relative neutron detection efficiency decreased to 0.84 due to neutron scattering in the lead. Shielding the detector with lead may result in build-up of 75-keV kX-rays that also generate pile-ups. Therefore, additional 7 mm layer of tin was placed in front of the detector and 3.5 mm around, resulting in 3 times lower $\varepsilon_{int\gamma n}$ and reduction of neutron detection efficiency to the level of 0.7. Copper shield of 3 mm thickness was also added in front of the detector to reduce 25-keV kX-rays emitted by tin. However, in this case we do not observe significant influence on the $\varepsilon_{int\gamma n}$ value.

It is worth noting that in the face of ^{3}He crisis is possible to achieve the $\varepsilon_{int\gamma n}$ at the level od 10^{-6} with 5.08 cm $\times$ 5.08 cm EJ309 liquid scintillator irradiated with 662-keV gamma-rays yielding the dose rate of 10 mR/h at the detector. However, this value is still at least an order of magnitude worse than that obtained with ^{3}He counter. On the other hand, by using the PUR and various shields, the relative neutron detection efficiency is reduced only by 45%.

Table 6.4: *Gamma-ray flux at the detector (in kcps), relative neutron detection efficiency and $\varepsilon_{int\gamma n}$ measured with EJ309 and various configuration of shielding materials (from [X]).*

shield	**no shield**	**Pb**	**Pb+Sn**	**Pb+Sn+Cu**
Pb				
front	–	50 mm	50 mm	50 mm
side	–	10 mm	10 mm	10 mm
Sn				
front	–	–	7 mm	7 mm
side	–	–	3.5 mm	3.5 mm
Cu				
front	–	–	–	3 mm
side	–	–	–	3 mm
gamma-ray flux (kcps)	41	6.8	4.6	4.5
relative neutron detection efficiency[4]	1.25	0.84	0.70	0.70
$\varepsilon_{int\gamma}$	3.1×10^{-4}	1.6×10^{-5}	5.1×10^{-6}	5.5×10^{-6}

6.1.5 Calibration of organic liquid scintillators

Organic liquid scintillators, especially low-flashpoint EJ309, has been used in wide area of nuclear physics experiments, as well as a possible alternative for the ^{3}He counters in homeland security applications. However, since the mechanism of neutron detection is based on proton recoil by elastic scattering, one needs to know the response function of light output to make a reliable energy determination of incident neutrons, and to obtain the detection

[4]Relative to intrinsic neutron detection efficiency of a polyethylene moderated ^{3}He counter with the same measurement conditions and geometry.

efficiency of liquid scintillators. As most organic scintillators show nonlinear response to neutrons, it is crucial to measure the response function as a function of recoil proton energy for various types of liquid scintillators. We have characterized three samples of liquid scintillators: EJ301, EJ309, and ^{10}B-loaded EJ309B5 [VII]. The detailed description of the experimental method for measurement of proton response for organic scintillators is presented in section 5.4, in chapter 5.

The experimental setup was validated with the ^{238}PuBe neutron source. A plot of the ZC time as a function of the ToF measured for the ^{238}PuBe is shown in figure 6.8. We observe four groups of coincidence events: gamma-gamma (γ-γ), neutron-neutron (n-n), neutron-gamma (n-γ), and gamma-neutron (γ-n). The results obtained with the DT generator reflect only n-n and γ-γ coincidences concentrated in well-defined groups. The gamma-rays in this case originate from the activation of the background (mainly in the metal tube of the generator). The angle θ, defined in the subsection 5.4.1 of the chapter 5 was set to 45 °. The distance from the START detector to the DT generator tube is 50 cm.

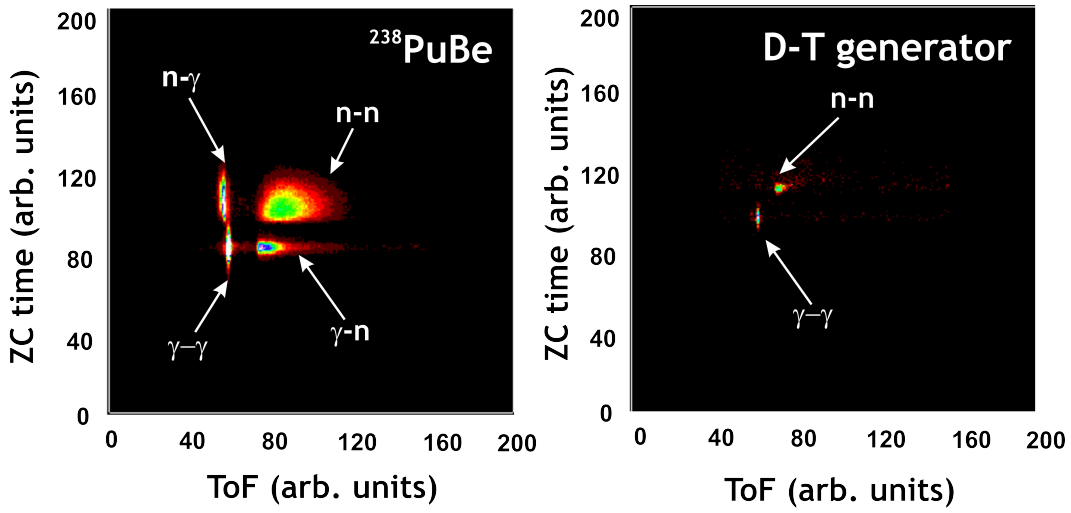

Figure 6.8: *Two-dimensional patterns of ZC time as a function of ToF recorded with EJ309 liquid scintillator irradiated with ^{238}PuBe source (left panel) and the DT generator (right panel).*

The calibration of liquid scintillators was performed with monoenergetic neutrons from the DT generator. The gain of the photomultiplier was controlled with several gamma-ray sources: the ^{137}Cs, the ^{60}Co, and 4.4-MeV gamma-rays from the ^{238}PuBe source. The data recorded by the *Kmax* acquisition system [112] were analyzed offline by choosing narrow

energy cuts (corresponding to ± 100-keV energy) on the ToF axis (which determine with relatively high accuracy the energy of recoil protons), and on ZC time axis (to reject gamma-ray background). Afterward, the selected data were projected onto the energy axis. Representative results of these projections for 4-MeV and 5-MeV recoil protons are presented in figure 6.9.

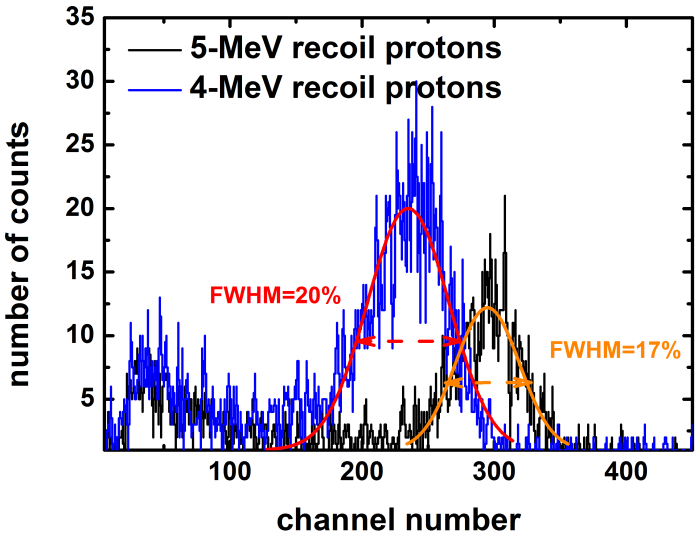

Figure 6.9: *The projection of ToC cuts onto energy (in MeVee) axis.*

The response functions of three tested organic liquid scintillators as a relation of the photoelectron yield (L-in MeVee) versus the kinetic energy of the recoil protons (E_p) in the energy range between 0.5–11 MeV are displayed in figure 6.10. The biggest drawback of the ToF method with the DT generator are relatively large uncertainties, particularly in the low energy region of the E_p-axis. It is due to using high energy neutrons for registering low energy recoil protons. The uncertainties can be reduced either by applying the DD generator that yields lower energy neutrons, or by increasing the distance between the detectors. However, the higher distance between the detectors would dramatically reduce the efficiency of the method.

The calibration data presented in figure 6.10 (left panel) were fitted with several model functions using a weighted least-square method. Initially, the response function were fitted with the linear empirical fit, similar to those given in [141]. However, the obtained fits are nonphysical, because for the energies close to zero, the curves have negative amplitude. The same situation occurs for a quadratic fit, proposed in [123] – the amplitude is either negative,

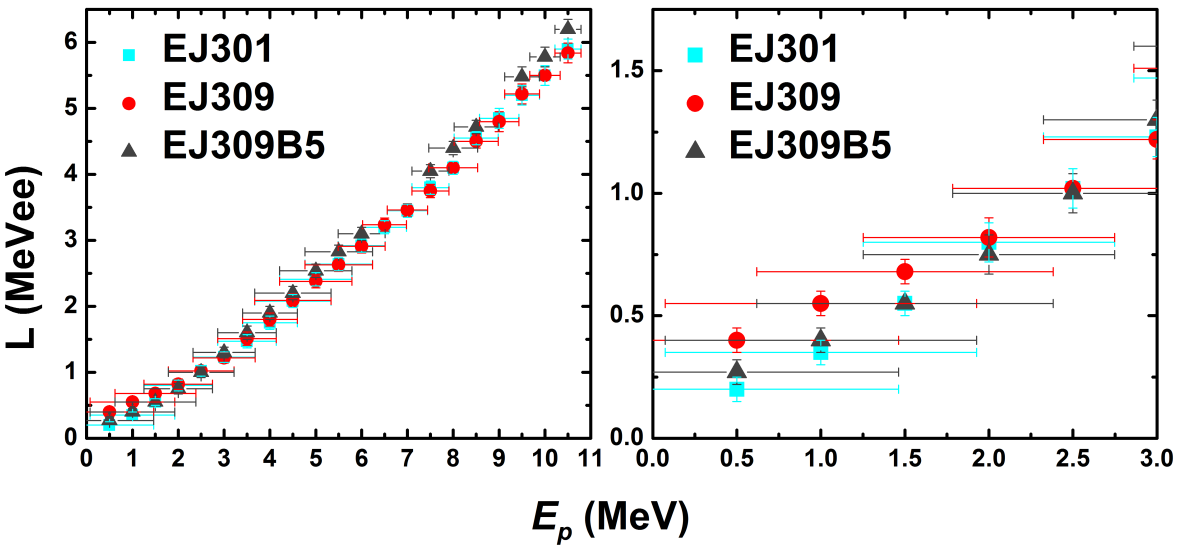

Figure 6.10: *Light output (in MeVee) of tested liquid scintillators as a function of recoil proton energy (in MeV).*

or more than zero at zero proton energy. Other possible empirical formula suggested by Kornilov *et al.* [142] and used in [128] is the ratio of polynomials

$$L = a\frac{E_p^2}{E_p + b} \tag{6.2}$$

where *a* and *b* are fitting parameters. Another possible formula, presented by Cecil *et al* [119] and also used in [128] is the exponential

$$aE_p - b[1 - e^{(-cE_p^d)}] \tag{6.3}$$

where *a, b, c* and *d* are fitting parameters. Those fitting functions have the benefit of extrapolating to zero at zero proton energy, without going negative for positive proton energies. Table 6.6 presents the parameters of the fitting functions 6.2 and 6.3 for all tested scintillators. The calibration plot for EJ309 liquid scintillator together with two fitting functions is shown in figure 6.11.

The goodness of the fits as a function of detector type and fit type represent the values of reduced chi-square $\chi^2_{reduced}$ parameter

$$\chi^2_{reduced} = \frac{\chi^2}{D} = \frac{1}{D}\sum_{i=1}^{n}\frac{(y_i - \hat{y}_i)^2}{\sigma^2}, \tag{6.4}$$

where χ^2 - is the chi-square parameter, y_i - is the measured data point, $\hat{y}_i$ - is the fitted point, D - is the degree of freedom, and σ - is the uncertainty of the data point. The value

Table 6.5: *The parameters obtained by fitting the measured data to the the model functions together with the $\chi^2_{reduced}$ values.*

fit type	coefficients		
	EJ301	**EJ309**	**EJ309B5**
polynomial (6.2)	a = 1.89 $\pm$ 0.04	a = 1.89 $\pm$ 0.12	a = 1.29 $\pm$ 0.11
	b = 0.66 $\pm$ 0.04	b = 0.66 $\pm$0.05	b = 0.64 $\pm$ 0.05
	$\chi^2_{reduced} = 1.53$	$\chi^2_{reduced} = 4.18$	$\chi^2_{reduced} = 1.52$
exponential (6.3)	a = 0.73 $\pm$ 0.09	a = 0.77 $\pm$ 0.04	a = 0.78 $\pm$ 0.07
	b = 2.95 $\pm$ 0.21	b = 2.63 $\pm$ 0.17	b = 2.44 $\pm$ 0.24
	c = 0.11 $\pm$ 0.07	c = 0.14 $\pm$ 0.07	c = 0.15 $\pm$ 0.08
	d = 0.99 $\pm$ 0.06	d = 1.12 $\pm$ 0.09	d = 1.09 $\pm$ 0.07
	$\chi^2_{reduced} = 1.04$	$\chi^2_{reduced} = 1.15$	$\chi^2_{reduced} = 0.99$

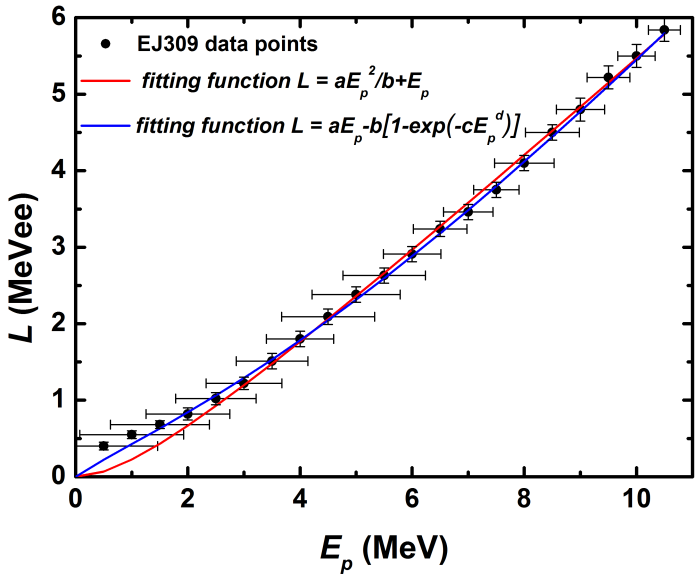

Figure 6.11: *The calibration curve measured with EJ309 liquid scintillator together with polynomial and exponential fitting functions.*

of $\chi^2_{reduced} \cong 1$ indicates that the extent of the match between the measured data points, and the value predicted by the fitting curve is in accord with the error variance. A $\chi^2_{reduced} \gg 1$ means that whether the fit has not captured the data, or that the errors are underestimated. The $\chi^2_{reduced}$ values for two fitting functions are presented in table 6.6. The goodness of fit is somewhat better for exponential fitting function than for the polynomial one. However, the $\chi^2_{reduced}$ values for both fitting functions are close to unity with the exception of EJ309, where the rational fit reveals higher value of 4.18, which means that this fit is worse matched

to the experimental data.

The results of the calibration versus the PSD performance

The calibration plot presented in the right part of the figure 6.10 indicated that for high-flashpoint EJ309B5 the recoil protons create more light than in EJ301. This means that in the high-flashpoint media the quenching effect is lower than in xylene-based ones. This result is in good agreement with the upshift of the thermal neutron peak observed in EJ309B5 in comparison to the xylene-based BC523A [VIII] and EJ339B5 [129]. It suggests that EJ309 should have better PSD capability in a low-energy range of recoil protons due to the higher relative light output. The FoM calculated for EJ309 for 500-keV recoil proton energy is higher than FoM calculated for EJ301, which means that the PSD quality in the case of EJ309 is better (see figure 6.12).

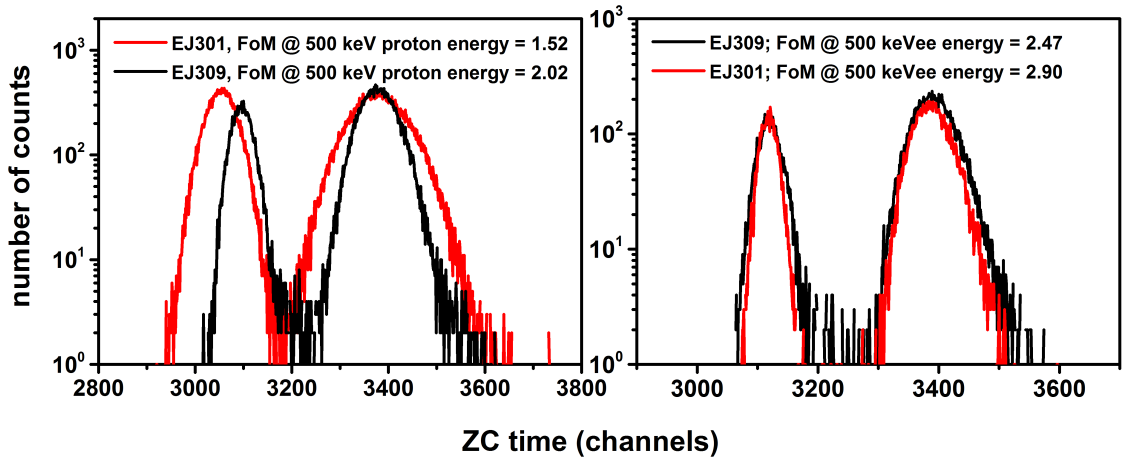

Figure 6.12: *ZC time spectra measured for a 500-keV recoil proton energy and 500-kev gamma-rays for EJ301 and EJ309 liquid scintillators.*

The PSD capabilities of EJ301 and EJ309 have been demonstrated by Stevanato *et al.* [143]; the comparison of these scintillators showed that EJ309 has worse neutron/gamma discrimination properties. This fact was confirmed by Pawelczak *et al.* [144]. It was also presented in our measurements (see figure 6.3). However, the result of PSD performance was determined for the same gamma-ray energies. Taking into account the same recoil proton energies, we observe the opposite - EJ309 has a higher FoM than EJ301 below approximately 1.5 MeV proton energy. The relative light output for EJ309 is higher than for EJ301 - a

500-keV recoil proton energy gate corresponds to recoil electron energies of approximately 400 keVee in EJ309 and approximately 200 keVee in EJ301. As a consequence of lower quenching for low-energy neutrons, the high-flashpoint liquid scintillators have lower neutron detection thresholds than xylene-based ones. Therefore, EJ309 and EJ309B5 may have higher neutron detection efficiencies than EJ301, if the detection threshold is set sufficiently low.

6.2 ^{10}B-loaded liquid scintillators for detection of fast and slow neutrons

Liquid scintillators are capable to detect and discriminate neutrons and gamma-rays using PSD technique. It has already been demonstrated in [110, 145] that, in the case of BC501A, the lower threshold can be achieved down to 40 keVee, which corresponds to approximately 300 keV of neutron energy detected by elastic scattering on protons [146]. Therefore, lower energy neutrons cannot be detected in classical liquid scintillators, because they produce to small amount of light and the signal has to low amplitude to be discriminated from gamma-rays and noise. ^{10}B-loaded liquid scintillators have been developed to increase the neutron sensitivity by detecting slow neutrons through the ^{10}B(n,α) reaction. They are capable to detect neutrons of energies ranging from tens of MeV down to thermal without any additional moderator.

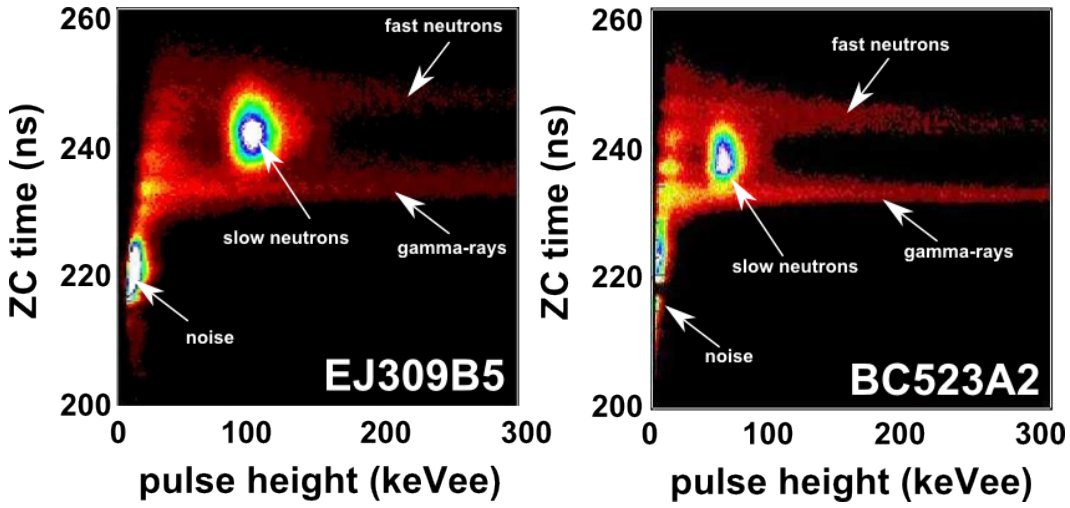

Figure 6.13: *A two-dimensional PSD plot recorded for boron-loaded BC532A2 and high flash point EJ309B5 liquid scintillators irradiated with moderated ^{238}PuBe source (from [129]).*

The PSD plots recorded with BC532A2 and EJ309B5 are presented in figure 6.13. The scintillators were irradiated by the ^{238}PuBe source placed inside the paraffin ball. Slow neutron capture reaction results in forming a peak at approximately 60 keVee for BC532A2 and at about 100 keVee for EJ309B5. We expected that events generated by the reaction products appear at larger values of ZC time, than fast neutron events, because the scintillation decay for alpha-particles and ^{7}Li should be longer than for protons. Surprisingly, the capture events are concentrated between the gamma-rays and fast neutrons. This fact is attributed to a strong light quenching of the slow component from particles by boron compounds dissolved in liquid scintillators [147]. In BC532A and EJ339A2 ^{10}B-loaded liquid scintillators thermal neutron events appear also at approximately 60 keVee [VIII]. Only EJ309B5 has thermal neutron peak at higher value of 100 keVee.

Detection efficiency of ^{10}B-loaded liquid scintillator and ^{3}He proportional counter

We have performed the comparative study of neutron efficiency, as well as gamma-ray sensitivity of ^{3}He proportional counter and EJ309B5 liquid scintillator:

– ^{3}He counter – was 5.08 cm in diameter and 101.90 cm long, with ^{3}He gas under the pressure of 2 atmospheres. The tube was made of 1 mm thick steel, and is surrounded with a polyethylene moderator – 5.08 cm on the back and 2.54 cm on the front and the sides. The signal from the detector was fed to the preamplifier, and further to shaping amplifier working on 1 μs time constant. The data were acquired using Tukan8k acquisition system.

– EJ309B5 - was 7.62 cm in diameter and 7.62 cm in height, and was coupled to Photonis XP53X2 photomultiplier. The experimental setup used for tests of EJ309B5 was presented in section 5.2 in chapter 5.

The detectors were tested using the same experimental procedure in the following conditions:

– according to [139] – for the evaluation of gamma-ray sensitivity in the values of the $\varepsilon_{int\gamma n}$ - under irradiation of an intense ^{60}Co gamma-ray source yielding a dose rate of

100 μSv/h (10 mR/h) at the detector. The $\varepsilon_{int\gamma n}$ can be measured using either an ^{192}Ir, a ^{137}Cs, or a ^{60}Co source.

– for neutron detection efficiency calculations - under irradiation of a moderated by several centimeters of polyethylene ^{252}Cf source yielding 10^6 n/s in full solid angle located 1 m perpendicular to the geometric midpoint of the detector. The American National Standards Institute (ANSI) standards assume using ^{252}Cf yielding 2×10^4 neutrons/s/4π, therefore our results were scaled to the response of the ANSI standard source.

– for background radiation.

A. ^{3}He counter

Due to the fact that both tested detectors are sensitive not only to neutrons, but also to gamma-rays, it is necessary to apply appropriate techniques to discriminate these two types of radiation. In the case of ^{3}He counter, gamma-ray rejection is due to the pulse height discrimination (PHD), which means that neutrons and gamma-rays deposit different amount of energy in the detector, and the separation can be performed by the inspection of the amplitude of the registered pulses. The PHD is based on setting a pulse height discriminator that acts a partition between two classes of pulses. The discriminator may be set either by hardware electronics, or by software. In our case, we introduce a mathematical parameter – *lower level discriminator* (*LL*, see figure 6.14) to clarify the determination of what LL setting will be necessary to achieve the $\varepsilon_{int\gamma n} \leqslant 10^{-6}$ with simultaneous as high as possible neutron detection efficiency. The efficiency parameter provides an information how sensitive the detector is to the incoming radiation, and is defined as

$$\varepsilon = \frac{N_{observed}}{N_{crossing}} \tag{6.5}$$

where the $N_{observed}$ is the recorded count rate, and the $N_{crossing}$ is the number of the photons or particles from the source crossing the detector.

A formulation of the $\varepsilon_{int\gamma n}$ as a function of LL is presented in the equation 6.7

$$\varepsilon_{int\gamma n}(LL) = \frac{\int_{LL}^{\infty} N_\gamma(x)dx}{\Phi_\gamma} \tag{6.6}$$

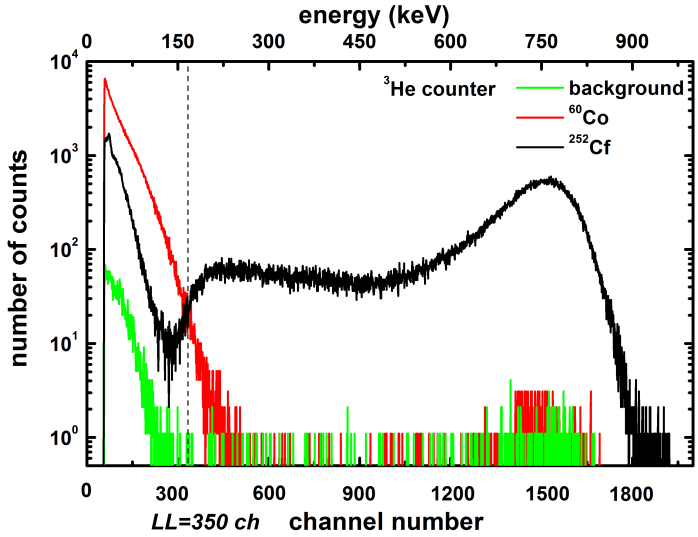

Figure 6.14: *Pulse height spectra recorded by ^{3}He proportional counter under irradiation of an intense ^{60}Co gamma-ray source, ^{252}Cf neutron source and background.*

where $\mathrm{N}_\gamma(x)$ is, the gamma-ray count rate after background subtraction, as a function of a channel number, and Φ_γ is the gamma-ray flux crossing the detector. By calculating the $\varepsilon_{int\gamma n}$ as a function of the *LL*, we only need to find what LL corresponds to having the $\varepsilon_{int\gamma n}$ of less than one in a million.

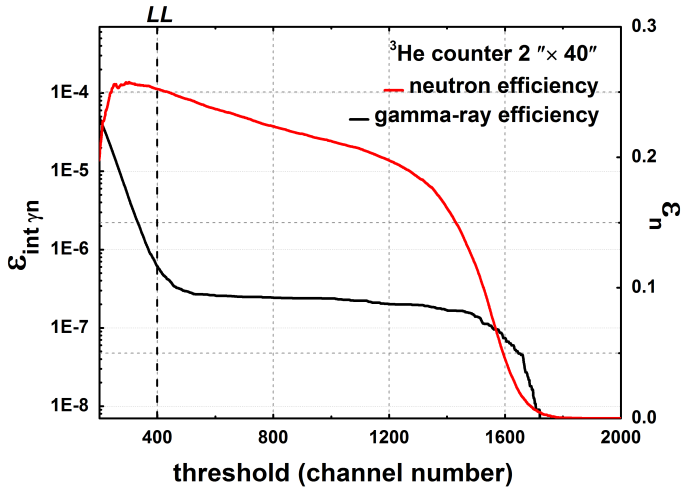

Figure 6.15: *The $\varepsilon_{int\gamma n}$ and the ε_n as a function of lower level measured for ^{3}He proportional counter.*

The neutron detection efficiency (ε_n) as a function of the *LL* is defined as

$$\varepsilon_n(LL) = \frac{\int_{LL}^{\infty} N_n^*(x)dx}{\Phi_n} \tag{6.7}$$

where the $N_n^*(x)$ is the scaled to the ANSI standards neutron count rate after background subtraction, as a function of a channel number, and Φ_n is the neutron flux crossing the detector. The number of counts obtained with the ^{252}Cf source was scaled to the ANSI standards source strength as follows:

$$N^* = \frac{(N - B)}{50} + B \tag{6.8}$$

where *N* is the count rate from recorded with the ^{252}Cf used in the experiment, and *B* - is the count rate in background.

The optimal value of LL, which is a gamma-ray cutoff point for the tested ^{3}He detector should be set at approximately 400 channel (see figure 6.15). Above this point, the $\varepsilon_{int\gamma n}$ is kept below 10^{-6}, whereas the ε_n is 0.25(3).

B. **EJ309B5 liquid scintillator (4.6% of ^{10}B)**

The implementation of neutron/gamma discrimination, based on the PSD technique, in EJ309B5 scintillator is much more complex than in the case of the PHD method applied in ^{3}He counter. A two-dimensional plot of ZC time as a function of pulse height recorded with EJ309B5 let us to observe events induced by different types of radiation (see figure 6.16). The data was obtained withe the polyethylene moderator around the scintillator, and the ^{252}Cf source was placed inside the paraffin ball.

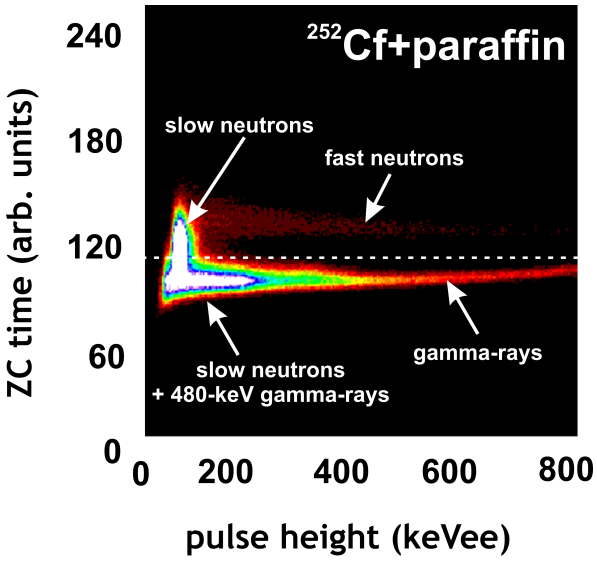

Figure 6.16: *ZC time as a function of pulse height recorded with EJ309B5 irradiated with the ^{252}Cf source.*

Due to the partial overlap of neutron and gamma-ray events in low-energy region, we marked three region of interest (ROIs) on the two-dimensional plot: low-energy(R1) - up to about 100 keVee, medium-energy (R2)- from 100 keVee up to about 500 keVee, and high-energy region (R3). We made a projection of the R1, R2, and R3 onto ZC time axis. We also marked those ROIs for gamma-rays from the ^{60}Co source (see figure 6.17). Analogously to ^{3}He counter, we calculated the $\varepsilon_{int\gamma n}$ and the ε_n for these ROIs. The lower level threshold (LL) was set at 3700 channel, where the separation between the neutron and gamma-ray events is the largest.

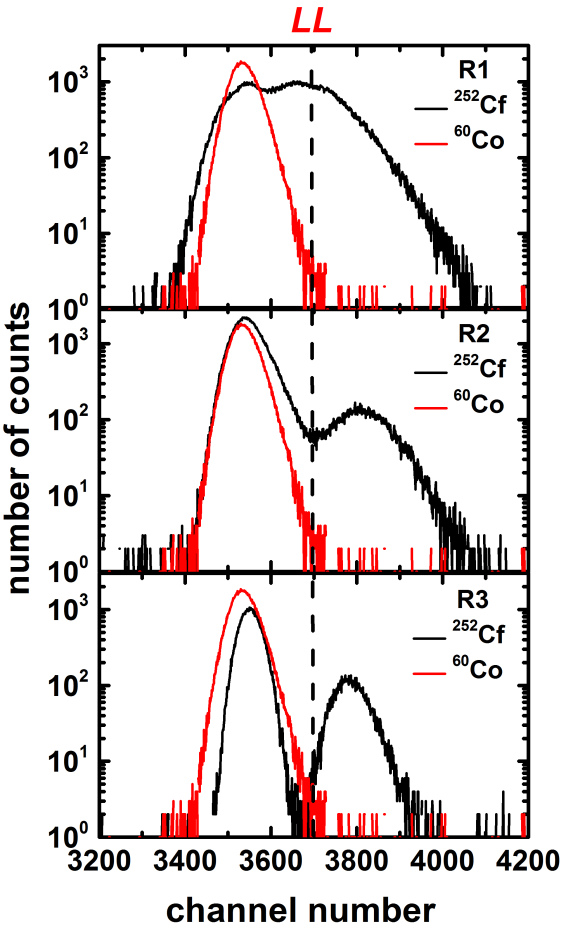

Figure 6.17: *ZC time spectra at three ROIs, recorded with EJ309B5 irradiated with the ^{252}Cf and the ^{60}Co.*

Table 6.6 presents the the $\varepsilon_{int\gamma n}$ and the ε_n calculated for events in ROIs R1, R2 and R3, separately, as well as for summed events from R1+R2, and R1+R2+R3. Due to large number of pile-up events in high-energy ROI, the sum of R1+R2 gives the best gives the best gamma-ray discrimination, with just slightly lower the ε_n. Figure 6.18 presents the $\varepsilon_{int\gamma n}$

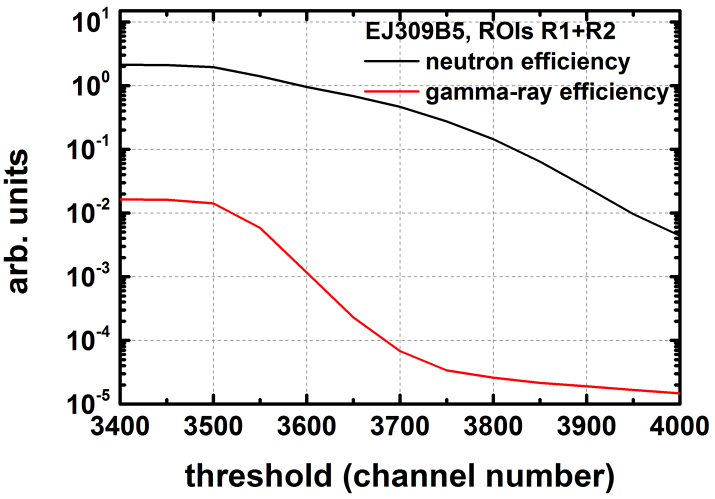

Figure 6.18: *The $\varepsilon_{int\gamma n}$ and the ε_n calculated for events in ROIs R1+R2 as a function of lower level threshold (ZC time) measured for EJ309B5 liquid scintillator.*

and the ε_n as a function of LL threshold calculated for R1+R2 ROIs.

Table 6.6: *The ε_n and the $\varepsilon_{int\gamma n}$ measured for EJ309B5 liquid scintillator at various ROIs.*

ROI	ε_n	$\varepsilon_{int\gamma n}$
R1	0.19(3)	$1.27(3)\times 10^{-5}$
R2	0.08(9)	$2.11(4)\times 10^{-5}$
R3	0.04(2)	$7.75(2)\times 10^{-5}$
R1+R2	0.3(7)	$2.68(9)\times 10^{-5}$
R1+R2+R3	0.27(4)	$1.13(2)\times 10^{-4}$

The $\varepsilon_{int\gamma n}$ calculated for EJ309B5 is much higher than obtained with ^{3}He counter, therefore it is necessary to apply additional, external shielding against large fluxes of gamma-rays, to meet ANSI requirements. The results show that the neutron detection efficiency is larger for the liquid scintillator than for the ^{3}He counter (note that ^{3}He counter has 6 times larger volume and covers more than 5 times larger solid angle). On the other hand the ^{3}He counter is significantly less sensitive to gamma radiation than the liquid scintillator. Thus, considering liquid scintillators as an alternative to ^{3}He counters, the improvement of performance is expected mostly by suppression of gamma-rays yield in neutron detection window.

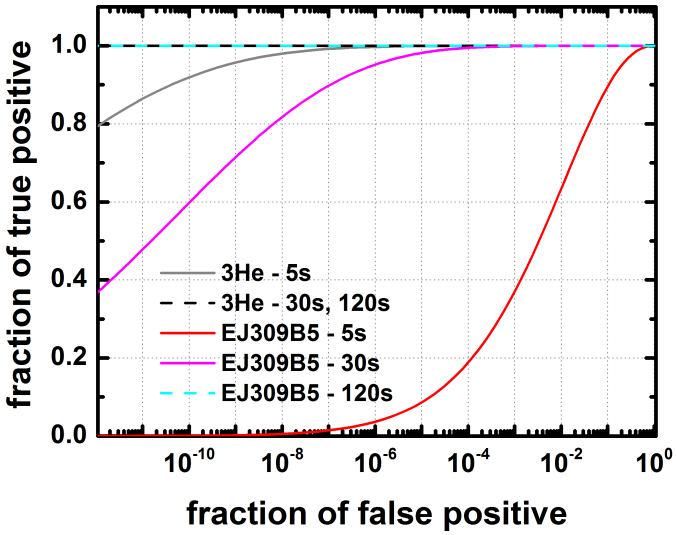

Figure 6.19: *ROC curves as a function of time obtained for ^{3}He proportional counter and EJ309B5 liquid scintillator.*

In the case of neutron detectors used for homeland security purposes, the speed of the measurement, as well as the problem of false alarm rate-the probability of accepting gamma-rays as neutrons-are of importance. In the context of detecting the SNM in a characterized background (or, in large gamma-ray flux), we invoke the **Receiver Operating Characteristic** (ROC) **curves**.The ROC curves are used to show how the fraction of false alarms (false positive signals at the detector) changes as a function of the probability of neutron detection (true positive), for various times of the measurement. We observe that for a very short measurement (in our case 5 s), the EJ309B5 has larger false alarm rate than the tested ^{3}He counter. However, 2 minutes of the measurement give the same results for both tested detectors.

6.3 Composite scintillators

It is commonly known that single crystals have the best neutron/gamma discrimination properties from all organic sciantillators. However, it is difficult to grow them in sizes larger than few cm^3 [27], therefore organic single crystals could not be the alternative for ^{3}He detectors, especially in the case of homeland security applications, where large volumes are required. The method of grinding single crystals, and incorporating them into a silicone matrix has been developed. Composite scintillators were developed in 2008 as the new type

of organic scintillators for fast neutron detection in the presence of gamma-ray background. Four samples of composites have been tested for basic scintillation proprieties, as well as neutron/gamma discrimination performance:

- *p*-terphenyl composite with dimension of ⌀5.0 cm × 2.5 cm,
- *p*-terphenyl composite with dimension of ⌀5.0 cm × 5.0 cm,
- stilbene composite with dimension of ⌀5.0 cm × 2.5 cm,
- stilbene composite with dimension of ⌀5.0 cm × 5.0 cm.

Stilbene single crystal with dimension of ⌀3.0 cm × 1.0 cm was tested as a comparison [II].

6.3.1 Light output

The number of photoelectrons for composite scintillators and stilbene single crystal are presented in table 6.7. In the case of composite scintillators, the resolution of the Compton continuum is deteriorated, due to the strong light absorption in a granular scintillator structure (see figure 6.20). Therefore, the determination of the Compton edge for composites is less precise than for other scintillators. The A_{max} for the composite scintillators was set as a centroid of the Gaussian fit. Despite the strong light absorption, composite scintillators have the N_{phe} comparable to liquids (see table 6.1). The light yield of a composite scintillator is a function of its thickness; for the thicker sample, the light transmission is poorer, than for the thinner one. It is caused by the scattering of light on the microcrystalline structures inside the scintillator.

6.3.2 PSD performance

Single crystals of anthracene, or stilbene are characterized by the best PSD performance from all organic scintillators. Figure 6.21 presents a two-dimensional plot of ZC time as a function of pulse height for stilbene single crystal irradiated with the ^{238}PuBe, and recorded by *Kmax* acquisition system. Figure 6.22 presents a two-dimensional plot of ZC time as a

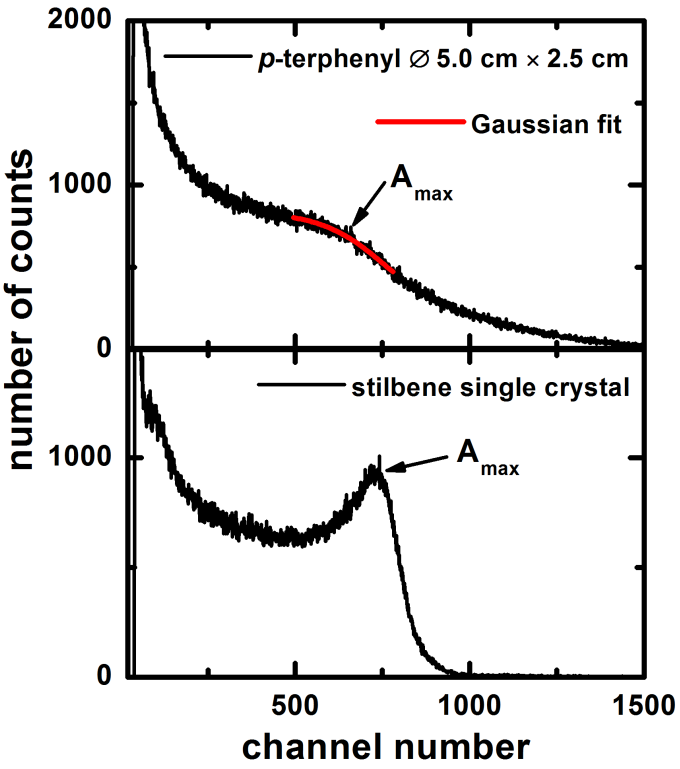

Figure 6.20: *The spectra recorded with a stilbene crystal and composite p-terphenyl irradiated with the ^{137}Cs. In the case of composite scintillator, the Compton continuum is broadened due to strong light absorption in a granular scintillator structure [II].*

Table 6.7: *The N_{phe} measured for composite scintillators and stilbene single crystal recorded with XP5500 photomultiplier tube (see table 5.1)*

scintillator	**dimension**	$\mathbf{N}_{phe}$ (phe/MeV)
stilbene (crystal)	⌀3.0 cm × 1.0 cm	3680
p-terphenyl (composite)	⌀ 5.0 cm × 2.5 cm	3100
p-terphenyl (composite)	⌀ 5.0 cm × 5.0 cm	1480
stilbene (composite)	⌀5.0 cm × 2.5 cm	1750
stilbene (composite)	⌀5.0 cm × 5.0 cm	860

function of pulse height recorded for *p*-terphenyl-based composite irradiated with neutron source. We can easily distinguish events generated by neutrons from those generated by gamma-rays. The lower threshold at the CFD was set at about 50 keVee. The PSD pattern recorded with stilbene single crystal is shown in figure 6.21.

To evaluate the PSD performance of the system for composite scintillators, the pulse

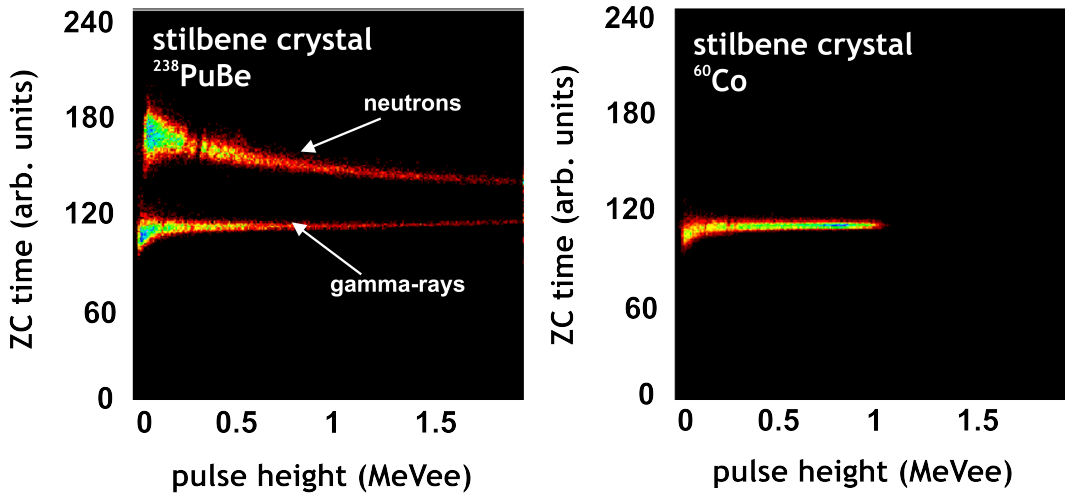

Figure 6.21: *Examples of experimental PSD two-dimensional patterns recorded by Kmax system obtained under irradiation of stilbene with the ^{238}PuBe and the ^{60}Co. The artifacts in the PSD spectrum are caused by oscillations in the neutron/gamma discrimination circuit.*

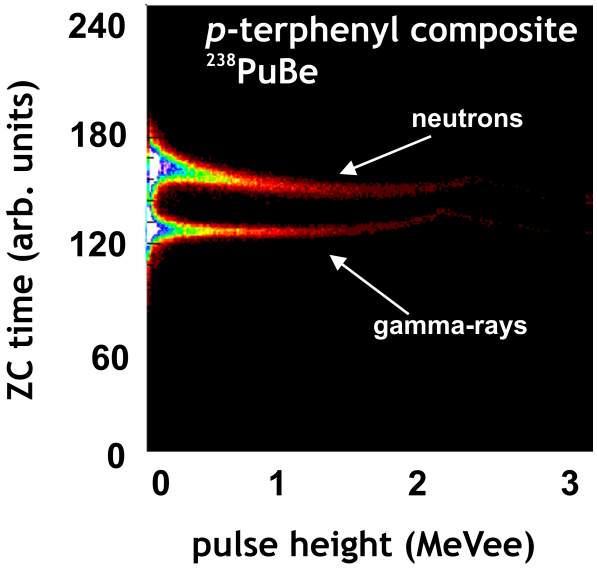

Figure 6.22: *Two-dimensional plot of ZC time as a function of pulse height measured with p-terphenyl-based composite (⌀ 5.0 cm × 2.5 cm) under irradiation of the ^{238}PuBe [II].*

height events were projected onto ZC time axis. This projection reveals notably resolved gamma-ray events and those generated by fast neutrons as two Gaussian-shaped peaks. The location of gamma-ray peaks was confirmed by the projection of events generated by ^{137}Cs source. In the case of *p*-terhpenyl-based composite we observe superbly resolved events from gamma-rays and neutrons down to 50 keVee (see figure 6.23). The spectrum from the ^{238}PuBe (black line) was recorded with the threshold set at 30 keVee. Noise bump appears on the left part of the spectrum (below 120 channel on ZC time axis). Raising the threshold

to 50 keVee (red line) the noise is reduced, and the discrimination between gamma-rays and neutrons improves.

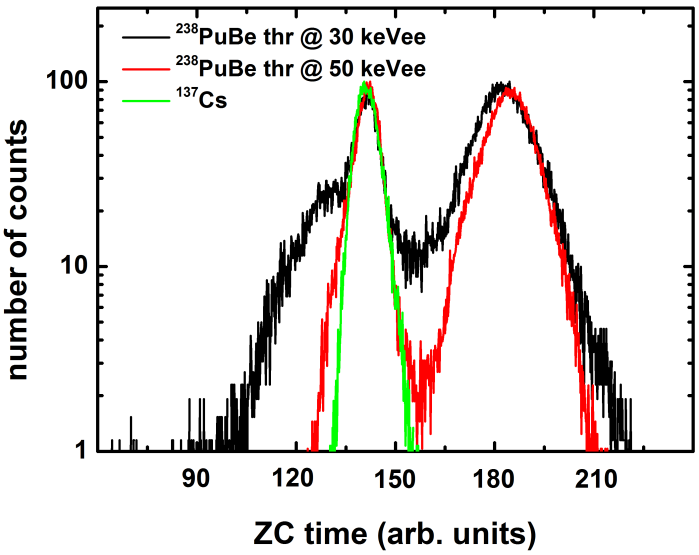

Figure 6.23: *ZC time spectra measured with p-terphenyl-based composite ⊘ 5.0 cm × 2.5 cm) under irradiation of the ^{238}PuBe and the ^{137}Cs. The spectra were normalized to 100 counts in gamma-rays peak maximum [II].*

The quantification of the PSD of the system was made by calculation of the FoM for the tested composite scintillators and stilbene single crystal (see equation 6.1). Due to slight dependence of ZC time on the energy in our PSD setup, FOMs were measured for narrow energy cuts, which ensured that the ZC time projections were Gaussian-shaped. In principle, the higher FoM value is, the better neutron/gamma separation is obtained. The values of FoM calculated for low energy cuts for *p*-terphenyl-based composite are comparable to those calculated for stilbene single crystal (see figure 6.25). For higher energy cuts the neutron/gamma separation for stilbene crystal is significantly better than for all composites. However, FoM $= 1.5$ means that peaks are well resolved (see figure 6.24).

When comparing the composites only, we can observe that for thicker samples the FoM is lower, because of the lower light yield caused by stronger light absorption inside the scintillator.

The photoelectron yield is an essential parameter for the accuracy of the ZC method, because the higher amplitude of the anode signal, the more precisely defined zero-crossing point. The *p*-terphenyl-based composites have better neutron/gamma discrimination perfor-

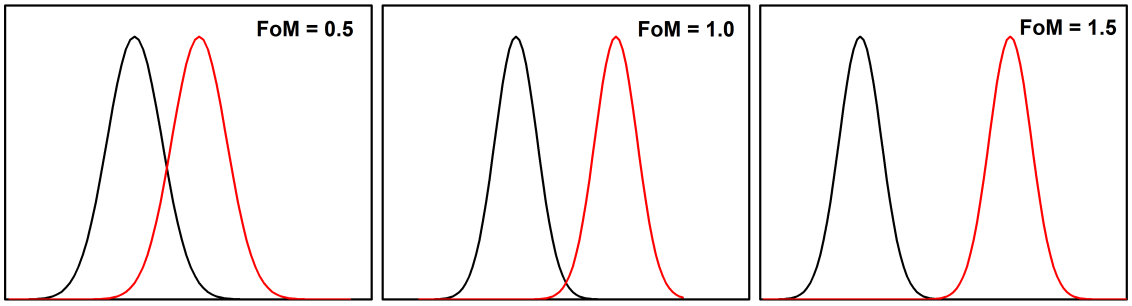

Figure 6.24: *.The exemplary plots with FoMs equal to 0.5, 1.0 and 1.5, respectively.*

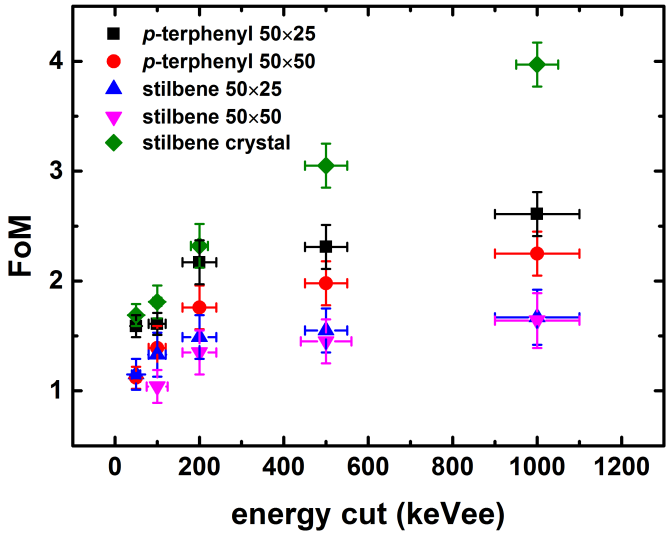

Figure 6.25: *The FoM as a function of energy cuts calculated for all samples of composite scintillators. The FoM for stilbene single crystal is presented as a comparison.*

mance than stilbene-based ones. The light in the composite scintillators, in contrast to single crystals, is diffused because of a scattering on the grains. Therefore, one can obtain higher signal in comparison with ordinary type of light transition for thin scintillators and the lower signal in comparison with the scintillation signal of a single crystal, if the composite scintillator and the single crystal are thick. They can be built in larger diameter than single crystals, but as their light output is reduced with increasing volume, they must be thin. Composite scintillators can be built as homogenous isotropic large surface detectors (not large thickness, due to decreasing transparency). In principle, they do not have technological limitation on the area of the detector, therefore could be used as large surface detectors for fast neutrons in the presence of background radiation.

6.4 Plastic scintillators with PSD capabilities

The lack of neutron/gamma discrimination in plastic scintillators has been overcome, and the results obtained by the group from Lawernce Livermore National Laboratory (the United States) [64], CEA in Saclay (France) [148], and the Institute of Scintillation Materials from the National Academy of Sciences of Ukraine [149] have been published. The most advanced work was done by the group from the United States, who sold their patent to the Eljen Technology company, and the plastics are now commercially available.

6.4.1 Small samples of plastics based on polystyrene

The first samples synthesized in the laboratories are usually small to test various configurations of solvent matrix and fluorophores. The first tested samples of plastics were based on polystyrene, and have been developed in two laboratories:

- $\oslash$ 2.5 cm $\times$ 1.0 cm plastic from Lawrence Livermore National Laboratory, hereafter called LLNL plastic,
- $\oslash$ 1.5 cm $\times$ 1.0 cm plastic from Institute for Scintillation Materials, National Academy of Sciences of Ukraine, hereafter called ISMA plastic.

The basic scintillation performance and PSD properties of LLNL and ISMA plastics were compared with the performance of stilbene single crystal ($\oslash$ 3.0 cm $\times$ 1.0 cm) V.

Photoelectron yield

Table 6.8 presents the comparative values of photoelectron yield for tested samples measured with the same experimental conditions. The stilbene crystal used in this experiment was the other sample that we have in our possession. Because the sample-to-sample variation in terms of basic scintillation properties, the photoelectron yield of the stilbene sample is slightly different than the yield presented in table 6.7. We see that the plastics have sufficiently high photoelectron yield, comparable to the first sample of stilbene crystal, and just

slightly lower than the second one.

Table 6.8: *The N_{phe} measured for plastic scintillators and stilbene single crystal and Photonis XP5500 photomultiplier tube 5.1.*

scintillator	dimension	N_{phe} (phe/MeV)
stilbene (crystal)	⌀3.0 cm × 1.0 cm	4200
LLNL plastic	⌀2.5 cm × 1.0 cm	3800
ISMA plastic	⌀1.5 cm × 1.0 cm	3100

The PSD performance

Figure 6.26 presents a two-dimensional plots of ZC time as a function of pulse height for the LLNL and the ISMA plastics under irradiation of the ^{238}PuBe. In the case of the ISMA plastic we observe slightly lower ZC time difference between gamma-rays and neutrons than for the LLNL plastic, which is the main factor of neutron/gamma discrimination properties of the scintillators.

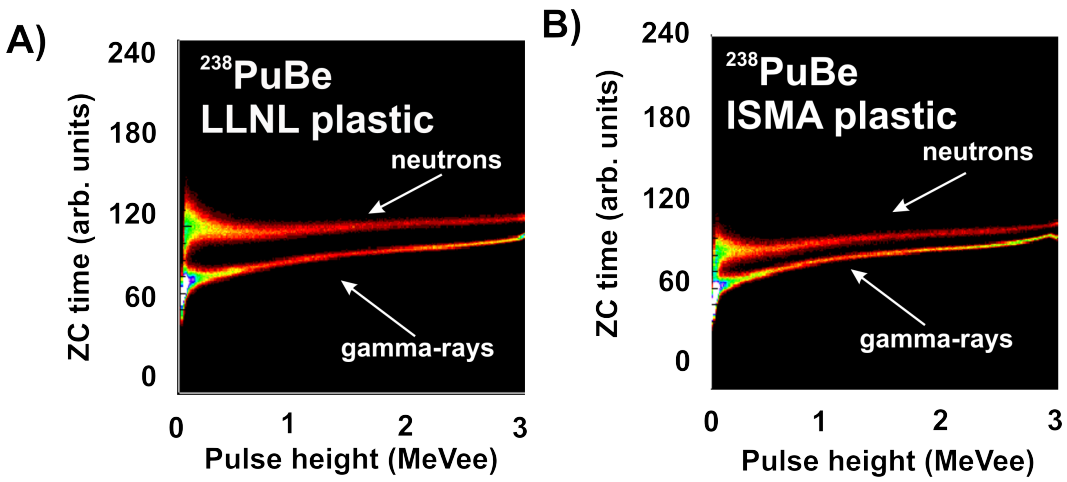

Figure 6.26: *Examples of experimental PSD two-dimensional patterns measured with the LLNL and the ISMA plastics [V].*

Figure 6.27 presents the FoM as a function of narrow energy cuts (± 10 keVee) for the LLNL and the ISMA plastics, as well as stilbene single crystal measured with the same experimental conditions. The LLNL plastic has slightly better neutron/gamma discrimination

performance than the ISMA plastic; however stilbene single crystal has still significantly better performance than all tested plastics.

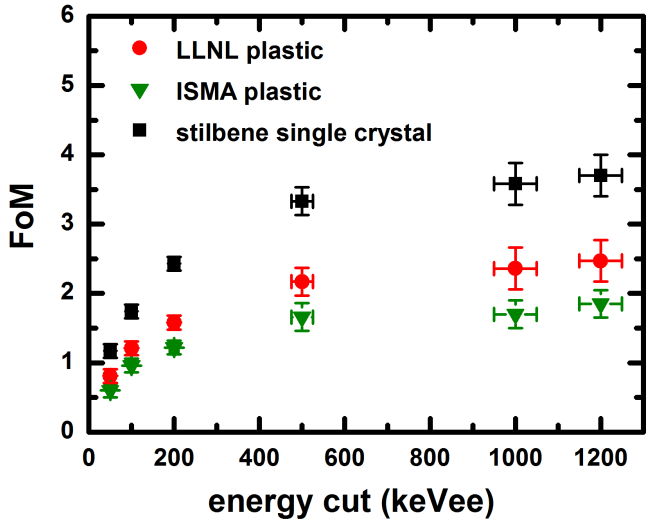

Figure 6.27: *FoM as a function of energy (in electron equivalent units) for the LLNL and the ISMA plastics, and stilbene single crystal.*

The tests of small samples of plastic scintillators showed that the problem of lack of neutron/gamma discrimination has been overcome, and there is significant improvement in development of plastic scintillators with PSD properties. Although organic single crystals have still better PSD performance than plastics, they give a reasonable alternative for neutron detection in gamma-ray background. The main advantages of plastic scintillators are their solid state of matter, non-toxicity, and inflammability in comparison to organic liquids. The results obtained with small samples are very promising, therefore there was necessary to test larger samples of plastics, to check if the PSD properties are unchanged with increasing dimension of the scintillator.

6.4.2 Scintillation properties and PSD performance of large plastic scintillators

The tested large plastic samples have commercial names as follows: EJ299-33, EJ299-34, EJ299-33G and EJ299-34G [VI]. Two of them are transparent and their emission maximum is approximately 430 nm (EJ299-33 and EJ299-34), whereas two others (EJ299-34G and

EJ299-33G) are greenish and maximum emission is shifted towards green wavelength (∼520 nm).

Light output

Table 6.9 presents the values of the photoelectron yield for the plastic samples and EJ309 organic liquid scintillator measured at the same experimental conditions. It is interesting to note that the N_{phe} measured for EJ299-34 plastic is almost equal to that of the liquid EJ309. The N_{phe} of EJ299-34G and EJ299-33G is about 4% less than their transparent equivalents, because the quantum efficiency of the PMT for 520 nm is 24%, whereas for 430 nm is 32%.

Table 6.9: *The N_{phe} measured for plastic scintillators with PSD capabilities and EJ309 organic liquid coupled to Photonis XP5500 photomultiplier tube 5.1.*

scintillator	**dimension**	**N_{phe}** (phe/MeV)
EJ309 (liquid)	⌀5.08 cm × 5.08 cm	2600
EJ299-34 (plastic)	⌀5.08 cm × 5.08 cm	2500
EJ299-34G (plastic)	⌀5.08 cm × 5.08 cm	2100
EJ299-33 (plastic)	⌀5.08 cm × 5.08 cm	1950
EJ299-33G (plastic)	⌀5.08 cm × 5.08 cm	1600

Light pulses from gamma-rays and neutrons

Light pulses for gamma-rays and neutrons after setting the gates recorded with EJ299-34 plastic are presented in figure 6.25. The pulses were fitted by triple-exponential curves in OriginPro 8.6 software [150]

$$y = A_1 e^{(\frac{-x}{\tau_1})} + A_2 e^{(\frac{-x}{\tau_2})} + A_3 e^{(\frac{-x}{\tau_3})} + y_0 \tag{6.9}$$

where A_1, A_2 and A_3 are the amplitudes of the curves, τ_1, τ_2 and τ_3 are the components of the decay time, y_0 is the baseline offset originating from random coincidences, which contribution was determined in the region before the light pulse. All the results for the tested scintillators, together with the decay time constants and intensities of components are collected in table 6.10.

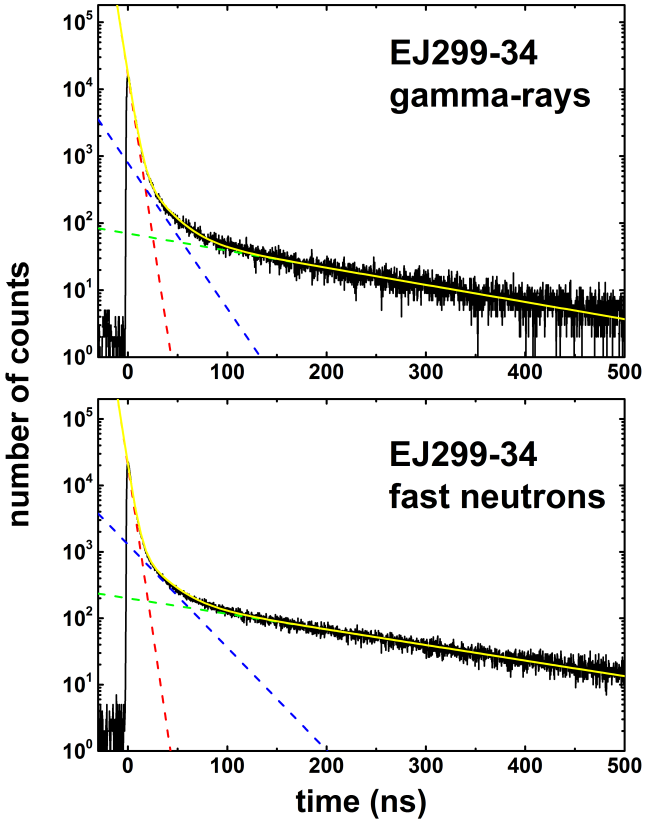

Figure 6.28: *Light pulse shapes recorded with EJ299-34 plastic irradiated with the ^{238}PuBe source and gated for gamma and neutron events, separately.*

Table 6.10: *Decay times (τ) and the light intensities (I) estimated for plastic scintillators [VI].*

		fast component		medium component		slow component	
scintillator	particle	τ_1 (ns)	I_1 (%)	τ_2 (ns)	I_2 (%)	τ_3 (ns)	I_3 (%)
EJ299-34	gammas	4.3 ± 0.2	**74**	18 ± 2	**14**	140 ± 10	**12**
	neutrons	4.5 ± 0.2	**58**	20 ± 3	**18**	170 ± 15	**24**
EJ299-33	gammas	4.6 ± 0.3	**73**	19 ± 2	**16**	130 ± 10	**12**
	neutrons	5.0 ± 0.2	**54**	22 ± 3	**21**	180 ± 15	**25**
EJ299-34G	gammas	5.3 ± 0.3	**73**	19 ± 2	**15**	150 ± 10	**12**
	neutrons	5.5 ± 0.3	**60**	25 ± 3	**17**	180 ± 15	**23**
EJ299-33G	gammas	5.6 ± 0.3	**76**	22 ± 3	**13**	160 ± 15	**11**
	neutrons	5.8 ± 0.3	**61**	25 ± 3	**15**	180 ± 15	**24**

First measurements of the light pulse shapes following excitation by gamma-rays and neutrons were measured in 1968 by Kuchnir and Lynch [135]. They measured the light pulses for stilbene crystal and three liquid scintillators: NE-213, NE-213M and NE-218 liquids. The

results of 4.05 ns and 33 ns for stilbene are comparable to those obtained with plastics (4.5 - 5.8 ns and 20-25 ns), whereas the third component, equal to 140-180 ns (depending on the sample) is much shorter than 270 ns reported in [135]. The measurements with liquid scintillators obtained by Szczesniak *et al.* [117] suggested that the quality of neutron/gamma discrimination for liquids is still better than for plastics. The differences in the intensities of slow components for gamma-rays and neutrons recorded with liquids are larger than for plastic samples. This component has the main influence on neutron/gamma discrimination. The same situation occurs with fast components; for example, fast component of EJ309 is dominating for gamma-ray events, covering about 90% of the emitted light, whereas, for tested plastics, it is only about 75%. In the case of neutron events, for EJ309 fast component is reduced to about 50%. For plastics, the intensity of the fast component for neutrons is 55-60%. The decay times fitted for EJ299-33 and EJ299-34 are equal in the range of statistical errors. The values obtained for "green" plastics are slightly longer, especially for fast components.

The PSD performance of plastic scintillators

Figure 6.29 (left top) presents the two-dimensional plot of ZC time as a function of pulse height obtained by irradiation of EJ299-34 plastic with 59.5 keV gamma-rays from the ^{241}Am source. The response to higher-energy gamma-rays was also checked by using the ^{22}Na source yielding 511 keV and 1275 keV gamma-rays. The measured spectra let us evaluate the location of gamma counts in ZC time vs. pulse height coordinates. The lower threshold was set at 50 keVee. As a comparison, the results for $\oslash$ 5.08 cm $\times$ 5.08 cm liquid scintillator are also presented.

To quantify the PSD performance of plastic scintillators, the FoM was calculated for narrow energy cuts. The neutron/gamma discrimination was studied using a ^{238}PuBe. We compared the FoMs obtained with the plastics to the FoM from EJ309 liquid scintillator. The plastics are capable of discriminating neutron events from gamma-rays; however, the FoM is much lower compared to the EJ309 (see figure 6.30). N. Zaitseva *et al.* presented the FOM at the level of 3 (for energy cut of 480 keVee $\pm$ 75 keVee) for 2.54 cm $\times$ 2.54 cm plastic scintillator [64], whereas for 5.08 cm $\times$ 5.08 cm sample the result for the energy cut of 500

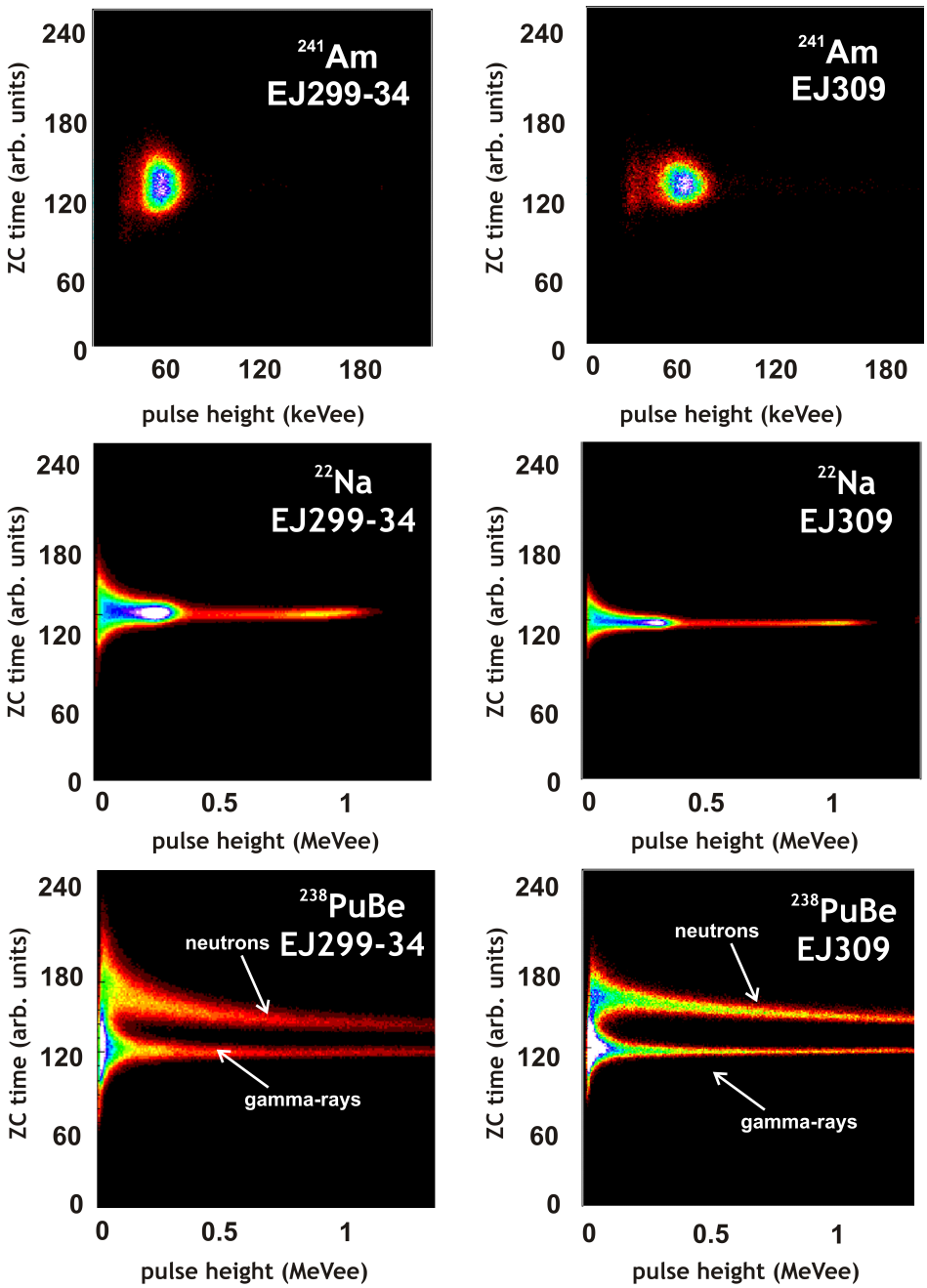

Figure 6.29: *Experimental two-dimensional PSD patterns recorded with EJ299-34 plastic and EJ309 liquid scintillator [VI].*

keVee ± 50 keVee is at the level of 1.5 [VI]. We also tested a small sample of plastic from LLNL, the results were just slightly poorer (FOM = 2.5 @ 500 keVee ± 50 keVee [V]), than those obtained by Zaitseva. The differences between 2.54 cm and 5.0 cm plastics are probably due to light attenuation in larger volume of scintillator.

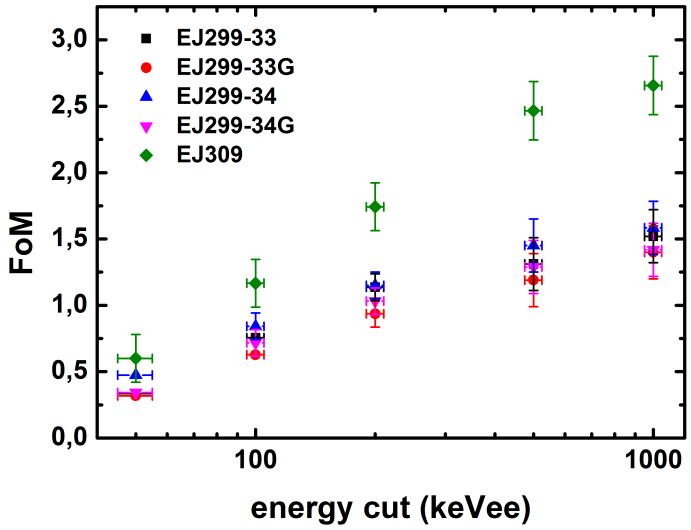

Figure 6.30: *The FoM as a function of energy cuts calculated for the plastics and EJ309.*

6.5 Conclusions

Neutron detection is an important aspect in detection of radiological threats for national security purposes, since SNM, such as plutonium, are used for nuclear weapons production. Commonly deployed neutron detectors used in Radiation Portal Monitors for homeland security applications are ^{3}He proportional counters. However, the shortage of ^{3}He isotope, and increasing the price of the systems based on the ^{3}He tubes, has motivated the researcher's community to find an efficient and cost-effective replacement technology. Fast neutron detectors based utilizing elastic scattering on hydrogen, such as organic single crystals, composites, as well as liquid and plastic scintillators have been tested in respect to be a possible alternative to ^{3}He counters.

Single crystals of anthracene, or stilbene are very efficient detectors with excellent PSD performance. However, it is difficult to grow them in large sizes, because of macrostructures appearing during the growth process. Therefore, organic single crystals could not be the alternative for ^{3}He proportional counters in homeland security applications. Recent reports in research on organic single crystals indicate a steady improvement in crystal size and quality. The technology, originally developed for growth of extremely large crystals of potassium dihydrogen phosphate (KDP) in Lawrence Livermore National Laboratory, allows to grow the organic scintillators from solution. This technology, transferred from inorganic crystals to organic ones, is currently under development. The Inrad Optics company that offers such

scintillators, reports that they are able to grow them 5.08 cm in diameter, and up to 10.16 cm in length.

Composite scintillators were developed as the efficient detectors of fast neutrons in presence of gamma-ray background. They are made of a small stilbene, or *p*-terphenyl grains introduced into a silicone matrix. Composites are usually compared with their parenteral materials in the terms of light output, decay time, and PSD performance. They have comparable neutron/gamma discrimination properties, as organic single crystals. However, the light in composite scintillators, in contrast to single crystals, is diffused because of their opacity. Therefore, the photoelectron yield of the composites is significantly lower than of the organic single crystals, and is strongly dependent on the composite's thickness. Large area composite scintillator, based on stilbene grains have been reached (20 cm in diameter and 2 cm in height). A composite scintillator made from stilbene single crystals embedded in Sylgard matrix is currently available via Proteus Inc. (USA). Considering composite scintillators as possible alternative to ^{3}He counter we must take into account light degradation with increasing volume of the scintillator.

Organic liquid scintillators are able to detect neutrons with energies from several hundred keV up to MeV. Moreover, loading them with ^{10}B increases the total neutron detection efficiency by capture reaction of slow neutrons on boron atoms. The majority of liquid scintillators are based on toxic and flammable xylene (the flashpoint of 24°C), which eliminates them from homeland security applications, where the safety of the public is crucial. The tendency of liquid scintillation cells to leak in time, could be also a disadvantage in using them for this purpose. Only EJ309 and boron-loaded EJ309B5 are less flammable – they have the flashpoint at 144°C. Organic liquids are very efficient neutron detectors, which was confirmed in our experiment with boron-loaded EJ309B5. They can be built in large volumes, and consequently, it is possible to increase the solid angle of detection. The advantage of liquid scintillators is their good neutron/gamma discrimination performance, but the $\varepsilon_{int\gamma n}$ is still too poor. In the case of homeland security applications, there is a strict requirement for limiting the false alarm rate (FAR) produced by the detection system, due to misidentification of gamma-rays as neutrons. Since the neutron alarm is an indicator of a plutonium threat, these alarms generate a significant response of the system. Neutron signatures can create only few signals per second over the background rate. Gamma-ray events generated by

sources used in medical treatment are several orders of magnitude larger than neutron events generated by the SNM. This puts a strong requirement on any neutron detection technology not to generate FAR in the presence of gamma-ray sources, only.

Plastic scintillators have been developed as non-toxic, solid-state detectors with the PSD properties for detection of fast neutrons in presence of a gamma-ray background. The photo-electron yield of commercially available plastics is comparable to liquid scintillators. However, the decay time constants measured for light pulses from gamma-rays and neutrons with plastics showed that the differences between fast and slow components are smaller for plastics than for liquid scintillators. This results in worse neutron/gamma discrimination properties of plastics. Moreover, tests of small and larger samples showed that the PSD performance became worse with increasing volume of the scintillator. This phenomenon is also observed in liquid scintillators, but it is not such significant, as in plastics. Although liquid scintillators have still better performance, and they could be better alternative than plastics in homeland security systems, plastics give a reasonable alternative for neutron detection with gamma discrimination in some applications. The advantage of plastic scintillators is their robustness, non-toxicity and inflammability.

Chapter 7

Results of a study on slow neutron detectors

Slow neutrons, interacting with the scintillation material, utilize capture reactions, and produce secondary charged particles, such as heavy ions, or gamma-rays. The Q-value of these reactions must be large to make an efficient and easy neutron/gamma discrimination. Moreover, the kinetic energy of secondary particles should be fully absorbed in the scintillation medium. The quenching of the light produced by charge particles, characteristic for scintillators, limits the neutron/gamma discrimination by a pulse height discrimination. The three most useful nuclear reactions for slow neutron detection are ^{10}B(n,α), ^{6}Li(n,α), and ^{3}He(n,p). The Q-values are so large in comparison to the neutron energy, that the reaction products do not give any information about neutron energy. Therefore, the detectors that utilize these reactions work in pulse counting mode, and the ToF spectroscopy must be employed, if slow neutron spectroscopy is necessary.

The shortage of ^{3}He in the world market forced the researchers to find the technology of neutron detection based on other isotopes. Besides fast neutron detectors, described in the previous chapters, also detectors that utilize nuclear reactions with slow neutrons can be applied in homeland security applications. However, in this case, additional external moderator is needed to thermalize fast neutrons from the SNM. The study on slow neutron detectors are focused on the scintillators that utilize ^{6}Li(n,α) reaction, because the Q-value of this reaction is larger than of ^{10}B(n,α). Moreover, in the case of the reaction on ^{10}B, not only

alpha particle, but also gamma-rays are emitted. These events may generate FAR, which is highly unwanted in the RPMs and hand-held devices at borders, where neutron events can generate only few counts per second above the background. There are few detectors based on ^{10}B isotope that can be potentially used for homeland security applications: BF_3 proportional counter, boron-coated straw detectors, and boron-loaded liquid scintillators (described and tested in the previous chapter). The BF_3 detector has lower neutron sensitivity than ^{3}He counter, and is highly toxic, which eliminates it for the applications, where the safety of the public is the most important. Boron-coated straw detectors could be promising alternative to ^{3}He counters [8], but they are unavailable at the European market.

7.1 ^{6}LiI(Eu)

Eu^{2+}-doped ^{6}LiI single crystals were investigated since late fifties by Murray, who tested the scintillator as fast neutron detector in the energy range 1-14 MeV [73]. He showed only poorly defined, broad peaks corresponding to elastic scattering of fast neutrons on lithium atoms. These fast neutron peaks were very sensitive to ambient temperature with the best energy resolution in -140°C. The scintillation efficiency of ^{6}LiI(Eu) was tested by Sakai, who compared it with the efficiency of NaI(Tl) [151]. The results were approximately 3.4-4.2 times lower than three NaI(Tl) samples presented in this paper.

Highly enriched ^{6}LiI(Eu) crystal (96% of ^{6}Li) is a very efficient slow neutron detector. ^{6}Li has a high cross-section for slow neutron capture (940 barns for 0.025 eV neutron energy). It has also a good gamma-ray spectrometry characteristics, with the FWHM for 662 keV from ^{137}Cs source of about 7% [74]. Combining the neutron detection with gamma-ray spectrometry, makes ^{6}LiI(Eu) very competitive for applications in hand-held detectors for homeland security. The crystals are hygroscopic, and it is difficult to obtain them in large sizes, therefore it is not possible to use ^{6}LiI(Eu) in large RPM systems.

The study on ^{6}LiI(Eu) were performed by Syntfeld *et al.*. Two samples of scintillator were examined: a large crystal with the dimension of ⌀50 mm × 5 mm (hereafter denoted as **L**) and smaller one (⌀30 mm × 3 mm) marked as **S**.

Pulse height analysis is the most common method used for measurements of slow neu-

tron detectors. The ^{6}LiI(Eu) scintillators were coupled to Photonis XP5200 photomultiplier with a silicone grease. A light guide was placed between the crystal and the photomultiplier's window to mix light produced in the planar-type crystal. This improved the transfer of the light between the scintillator and the photocathode, which consequently improved the energy resolution of the gamma-ray peaks, as well as the neutron peak. The anode signal was processed by a charge sensitive preamplifier, and then sent to the amplifier working on unipolar Gaussian shaping. The shaping time set at the amplifier is always fitted to the decay time of the scintillator to integrate the whole light from the sample. The Tukan8k multichannel analyzer was used to record the spectra. In the paper, the discussion on non-proportionality of the light yield, energy resolution in gamma-ray spectrometry was taken, as well as neutron detection performance was tested. The neutron tests were performed with the **L** sample.

7.1.1 Neutron detection with ^{6}LiI(Eu)

The tests of slow neutron detection was performed with moderated ^{238}PuBe source. The source was surrounded with paraffin blocks to slow down the neutrons, and 5 cm lead bricks were placed in front of the source to reduce the flux of 4.4-MeV gamma-rays from the excited state of the ^{12}C that is produced in the (α,n) reaction. The exemplary spectrum of a moderated and shielded ^{238}PuBe recorded with the **L** sample is presented in figure 7.1. Well defined, narrow Gaussian peak originating from tritons and alpha particles, with the FHWM of 3.9% [1] appears at approximately 3.5 MeV gamma energy equivalent (GEE), with a very good peak-to-background ratio. The position and the resolution of the peak indicates that the quenching of the light from (n,α) events is low. We also observe a continuous gamma-ray background with a peak from the ^{40}K isotope.

[1] *Energy resolution* is the parameter in radiation spectroscopy, where the measurement of the energy distribution of incident radiation is of importance. This is the extent to which the detector can resolve slightly different energies and is defined as the *Full Width at Half Maximum* (FWHM) divided by the location of the peak centroid, expressed as percentage [27]

Intrinsic efficiency for slow neutron detection

Intrinsic efficiency for neutron detection from moderated ^{238}PuBe source (ε_{PuBe}) can be expressed by the formula

$$\varepsilon_{PuBe} = 1 - e^{(-n\sigma x)} \tag{7.1}$$

where n is the number of ^{6}Li atoms per volume unit, σ is the cross section for the reaction of interest, and x is the thickness of the scintillator.

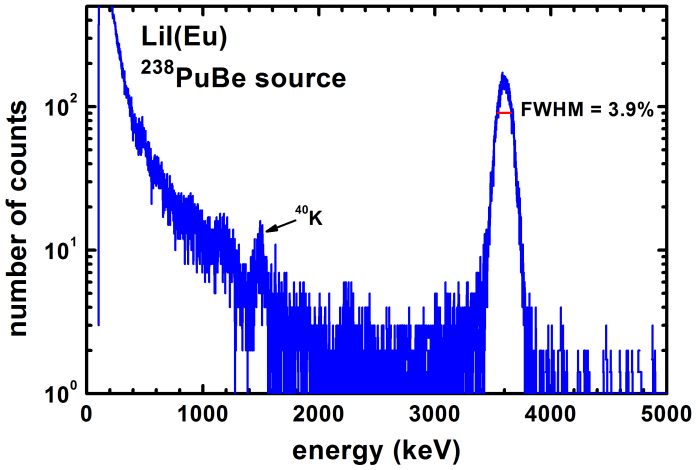

Figure 7.1: *The spectrum of the ^{238}PuBe shielded with paraffin and lead recorded with ^{6}LiI(Eu).*

The ε_{PuBe} for 5 mm sample was calculated as 99.98%, assuming that n = 1.85$\times$10^{22} atoms/cm^3, and the σ for ^{6}Li(n,α) = 940 barns. These calculation is based on the assumption that the neutrons are of thermal energy. However, the ^{238}PuBe source emits fast neutrons that are just partly thermalized by the paraffin, or polyethylene blocks, to the energies higher than 0.025 eV.

7.1.2 Detection of fissile materials with ^{6}LiI(Eu)

The fissile samples of enriched (4.46%) ^{235}U, low- (95%), and high-burnup (61%) ^{239}Pu were used to irradiate the **L** sample of ^{6}LiI(Eu). The first sample contained 7.6 g of the ^{235}U, the second one - 6.2 g of the ^{239}Pu, and 0.4 g of the ^{240}Pu, and the third one - 4.2 g of the ^{239}Pu and 1.7 g of the ^{240}Pu. The plutonium samples contained also small amount of

impurities. Pure ^{239}Pu produced the neutrons at a rate of about 20 n/s/kg and gamma-rays at energies from 300 to 700 keV. The ^{239}Pu is produced artificially, and always occurs with the other Pu isotopes: the ^{240}Pu, the ^{241}Pu, and the ^{242}Pu. Since they have the same chemical characteristics, it is impossible to separate them from each other by chemical techniques. The ^{240}Pu emits neutrons at a rate of 10^5 times higher than the ^{239}Pu.

Figure 7.2 presents spectra measured with ^{6}LiI(Eu) irradiated with the moderated low- and high-burnup plutonium shielded with 30 mm of lead. The neutron count rates measured with the plutonium samples were estimated as 45 n/s/kg for low-burnup sample, and 240 n/s/kg for high-burnup one. In the case of uranium sample, the number of neutrons produced by spontaneous fission process was only 0.01 n/s/kg. Moreover, the detection of neutrons was obscured by a high laboratory background.

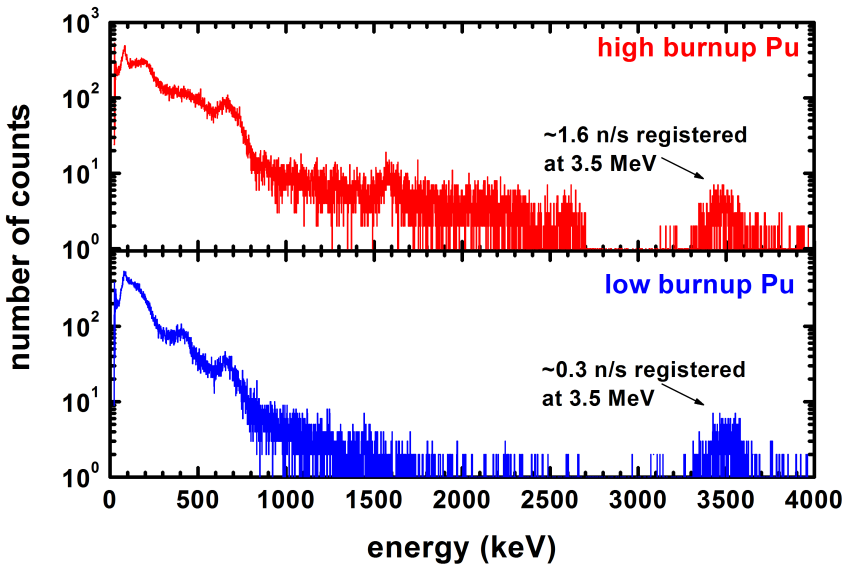

Figure 7.2: *The spectra of the high- and low-burnup plutonium samples recorded with ^{6}LiI(Eu). The 30 mm lead shield was placed between the detector and the plutonium.*

The measurements showed that ^{6}LiI(Eu) is a highly-sensitive neutron detector. Additionally, the capability of gamma-ray spectrometry allows to use the crystal in hand-held identifiers with simultaneous neutron detection. The gamma-ray discrimination was also presented in the paper, but the authors did not provide any value of $\varepsilon_{int\gamma n}$. However, the neutron peak was easily recognized from the events from an intense ^{60}Co source.

7.2 GS20 lithium glass

Silicate glasses containing ^{6}Li and activated with Ce^{3+} are widely used as neutron detectors, because amorphus structure provides wide range of sizes and shapes of the scintillator. Moreover, they are resistant to temperatures, relatively robust and non hygroscopic. The scintillation properties, as well as neutron detection performance of a sample of GS20 lithium glass with 95% enrichment of ^{6}Li were tested. Basic properties of the sample are presented in table 7.1.

The scintillator was coupled to Photonis XP5300 photomultiplier with silicone grease. Similarly to ^{6}LiI(Eu), a light guide was placed between the protective window of the GS20 and the photomultiplier, to distribute the light, produced in the planar-type scintillator, uniformly over the photocathode. The signal from the anode was sent to the preamplifier, and further, to the shaping amplifier. The signal from the scintillator was recorded with Tukan8k acquisition system. The N_{phe} was estimated using 661.7-keV full energy peak from the ^{137}Cs source.

Table 7.1: *Basic properties of GS20 lithium glass*

sample	GS20
dimension	⌀50.8 mm × 2 mm
density	2.5 g/cm^3
decay time	75 ns
maximum emission	395 nm
^{6}Li atoms/cm^3	1.58×10^{22}
N_{phe}	∼1300 phe/MeV

7.2.1 Neutron response of GS20

Neutron response of GS20 scintillator was tested with the ^{238}PuBe placed into a paraffin ball and shielded with 5 cm of lead to reduce the intensity of 4.4-MeV gamma-rays from the source. Figure 7.3 presents the spectra obtained with GS20 and irradiated with a moderated ^{238}PuBe source with and without light guide between the scintillator and the photocathode

window. The use of light guide improved the FWHM of the neutron peak.

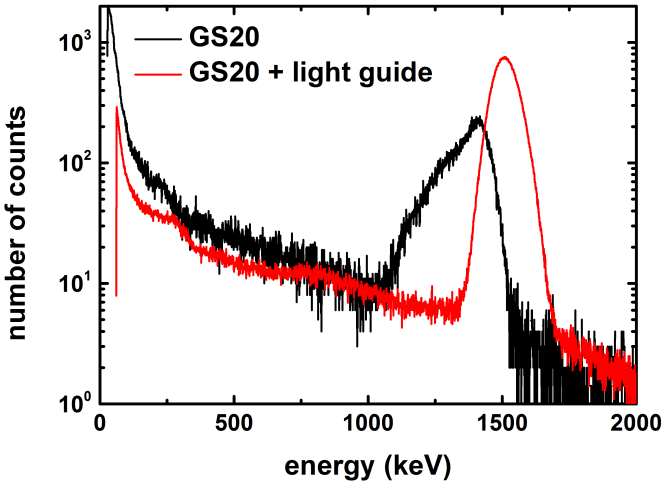

Figure 7.3: *Neutron response of GS20 lithium glass with and without light guide placed between the scintillator and the photocathode window.*

The neutron and gamma-ray response of GS20 is presented in figure 7.4. We observe the neutron peak at about 1.5 MeV GEE with the resolution of 7.35%. Full energy peak of gamma-rays emitted from ^{60}Co source is not observed, because the scintillator has low density, and low atomic number.

The ε_{PuBe} of the GS20 lithium glass with the thickness of 5 mm was calculated as 99.98%, which means that the intrinsic efficiency for slow neutron detection for lithium glass is similar to the result obtained with ^{6}LiI(Eu). The gamma-ray sensitivity expressed as a value of $\varepsilon_{int\gamma n}$ was also estimated. An intense ^{137}Cs source was placed in front of the detector to increase the ambient background to 10 mR/h. The value obtained with the sample of GS20 glass was kept below 10^{-7} [III].

7.3 LiCaAlF$_6$ (LiCAF)

Rare-earth-ion doped LiCAF scintillators containing ^{6}Li with large absorption cross section for thermal neutrons have been developed as high efficiency neutron detectors. Since a ^{6}Li(n,α) reaction has a large Q-value of 4.8 MeV, the light yield caused by neutrons is higher than that caused by gamma-rays. Therefore, we can discriminate neutron events from gamma-rays ones by the pulse height discrimination.

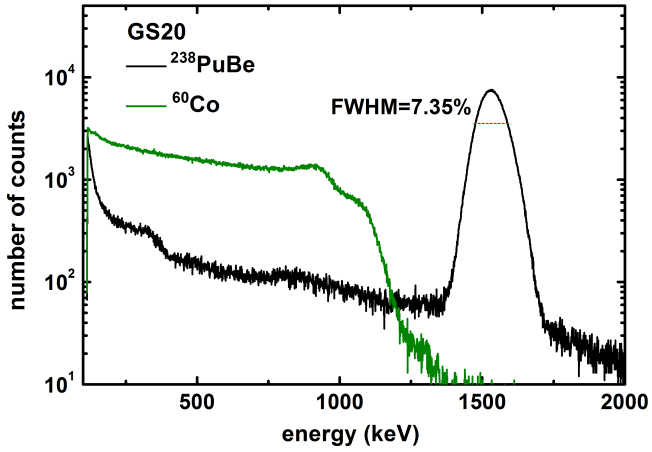

Figure 7.4: *Neutron and gamma-ray response of GS20 lithium glass [III].*

We have tested several samples of LiCAF scintillators, both Ce^{3+}- and Eu^{2+}-doped as single crystals, as well as a sample of Eu:LiCAF scintillator in the form of transparent rubber. The results obtained with the LiCAF samples were compared to those obtained with GS20 lithium glass. Basic parameters of the LiCAF samples are presented in table 7.2. The experimental setup was the same, as used for GS20 tests, with the difference that cuboid samples of LiCAF, and LiCAF rubber were coupled directly to the photomultiplier window.

Table 7.2: *Basic properties of LiCAF scintillators*

sample	**dimension (mm^3)**	**density (g/cm^3)**	**decay time**	**maximum emission (nm)**	**^{6}Li atoms/cm^3**	**N_{phe} (phe/MeV)**
low-doping Ce:LiCAF	10×10×2	2.94	40 ns	300	0.5×10^{22}	∼190
high-doping Ce:LiCAF	10×10×2	2.94	40 ns	300	0.5×10^{22}	∼225
high-doping Ce:LiCAF	⌀50.8 ×2	2.94	40 ns	300	1×10^{22}	∼255
Eu:LiCAF	15×15×1	2.99	1.6 μs	370	9.6×10^{21}	∼8100
Eu:LiCAF (rubber)	15×15×5	1.3-2.0	1.6 μs	375	$0.9\text{-}4.5\times10^{21}$	∼5600

7.3.1 Ce:LiCAF single crystals

The tested samples of Ce:LiCAF (see table 7.2) are dedicated to detect slow neutrons, therefore we used a paraffin moderated ^{238}PuBe neutron source, shielded by 5 cm of lead in order to reduce the 4.4-MeV gamma-ray flux. The results obtained for low-doping and high-doping small Ce:LiCAF samples, as well as for a large sample, are presented in figure 7.5. We can observe increasing the FWHM for neutron peak with increasing dimension of the scintillator. The ^{60}Co spectra are also presented to show that gamma-ray events do not overlap the neutron peaks.

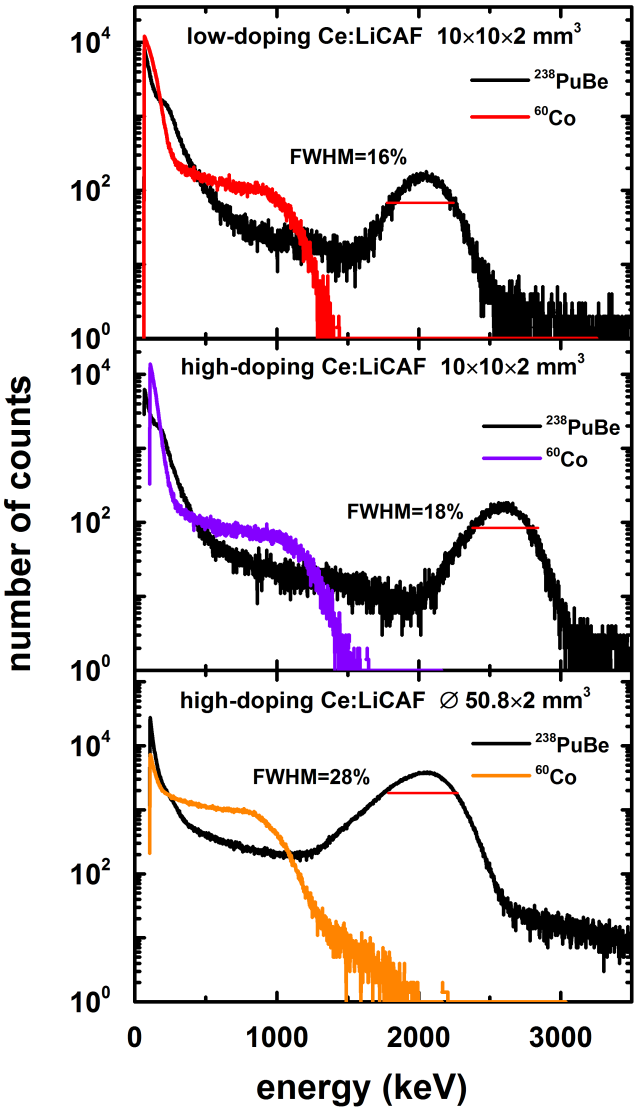

Figure 7.5: *Neutron and gamma-ray response of Ce:LiCAF samples [III].*

Neutron peak appears at 2 MeV GEE for low-doping Ce:LiCAF 10 mm × 10 mm × 2 mm, 2.5 MeV GEE for high-doping Ce:LiCAF 10 mm × 10 mm × 2 mm, and 1.9 MeV GEE high-doping Ce:LiCAF ⊘50.8 mm × 2 mm. The distribution of slow neutrons has the FWHM at about 16% for low-doping Ce:LiCAF 10 mm × 10 mm × 2 mm, 18% for high-doping Ce:LiCAF 10 mm × 10 mm × 2 mm, and 28% for high-doping Ce:LiCAF ⊘50.8 mm × 2 mm. Despite that neutron peaks are broad, in the case of both small cubic samples, neutron/gamma separation is good. Only in the case of large sample of Ce:LiCAF the neutron peak is partly covered by the Compton continuum from the ^{60}Co. For the reference GS20 glass the resolution of neutron peak is significantly better than for Ce:LiCAF samples (FWHM = 7.35%, see figure 7.4), mainly due to a larger photoelectron yield, however the neutron/gamma separation is worse (the neutron peak is located at about 1.5 MeV GEE), and neutron peak is slightly covered by the Compton continuum from the ^{60}Co.

Intrinsic neutron detection efficiency and intrinsic gamma-neutron detection efficiency

The ε_{PuBe} for Ce:LiCAF samples was estimated and compared with the efficiency of GS20 lithium glass. Considering 2 mm thick samples, quotient of thermal neutron efficiency for large discus-shaped Ce:LiCAF to GS20 will be 85%:99.8% (about 0.85:1.00) according to the formula, whereas we observed a ratio of 0.50:1.00. The same situation occurs for small samples of Ce:LiCAF (see table 7.3). This means that nσx $\ll$ 1, so we can assume that $\sigma \ll$ 940 barns. It results from the fact that the neutron flux from the ^{238}PuBe source after passing the paraffin is not enough thermalized, which agrees with our expectations.

Table 7.3: *Intrinsic neutron efficiency for tested Ce:LiCAF scintillators and GS20 as a reference.*

sample	**dimension (mm^3)**	ε_{PuBe}
GS20 lithium glass	⊘50 × 2	100%
low-doping Ce:LiCAF	10×10×2	32%
high-doping Ce:LiCAF	10×10×2	35%
high-doping Ce:LiCAF	⊘50.8 ×2	50%

Measurements with an intense ^{137}Cs radionuclide source were also performed. Using the gamma source we increased the ambient background to 10 mR/h, and we checked how many

events from gamma-rays occur in the neutron window. In the case of all tested samples of Ce:LiCAF, the $\varepsilon_{int\gamma n}$ was kept at the level of 10^{-6} [III].

7.3.2 Eu:LiCAF and Eu:LiCAF rubber

A study of Ce^{3+}-doped LiCAF as scintillators shows comparable neutron/gamma discrimination and thermal neutron detection efficiency to GS20 lithium glass. However, low scintillation efficiency limits a wider application of Ce:LiCAF as a scintillator. Eu^{2+}-doped LiCAF crystals present significantly higher light output than Ce^{3+}-doped ones. However, the discrimination between gamma-rays and neutrons is worse (see figure 7.7). The newest solution for improvement of neutron/gamma discrimination with Eu:LiCAF scintillator is a flexible sheet consisting of Eu:LiCAF crystals. Unique configuration of the detector, in which wavelength shifting fibers are incorporated in the scintillation crystal grains, makes efficient light collection from large to small area photodetector. Basic properties of Eu:LiCAF single crystal, as well as the rubber are presented in table 7.2.

Gamma-ray and neutron response of Eu:LiCAF

The estimation of the N_{phe}, in the case of single crystal of Eu:LiCAF, was made by using the Compton edge of gamma-rays from a ^{137}Cs source and a single photoelectron spectrum from the photomultiplier (Bertolaccini method). In the case of the Eu:LiCAF rubber, only a small fraction of electrons loses a full energy in the grains, and we do not observe typical Compton edge (see figure 7.8). Therefore, it is impossible to estimate the precise value photoelectron number. The end of the ^{137}Cs spectrum recorded for the rubber is about at 70% of the distance to the Compton edge measured for the single crystal. Therefore, we can assume that the photoelectron yield is approximately 70% of that measured for the single crystal (see Table 7.2). Low photoelectron number in the rubber is due to a small size of crystal grains, much lower than a range of secondary electrons produced by gamma-rays. The ^{238}PuBe neutron source was used to measure neutron spectra for both Eu:LiCAF scintillators. To obtain slow neutrons, we put the source inside the paraffin ball. Additionally, to reduce the flux of 4.4-MeV gamma-rays following the (α,n) reaction in the ^{238}PuBe, we used 5 cm thick lead wall. Exemplary spectrum measured with the single crystal of Eu:LiCAF is presented in

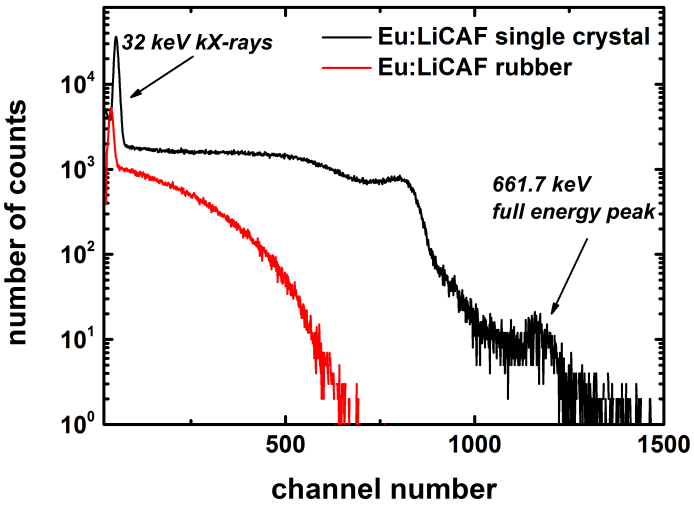

Figure 7.6: *Gamma-ray response of Eu:LiCAF single and Eu:LiCAF rubber.*

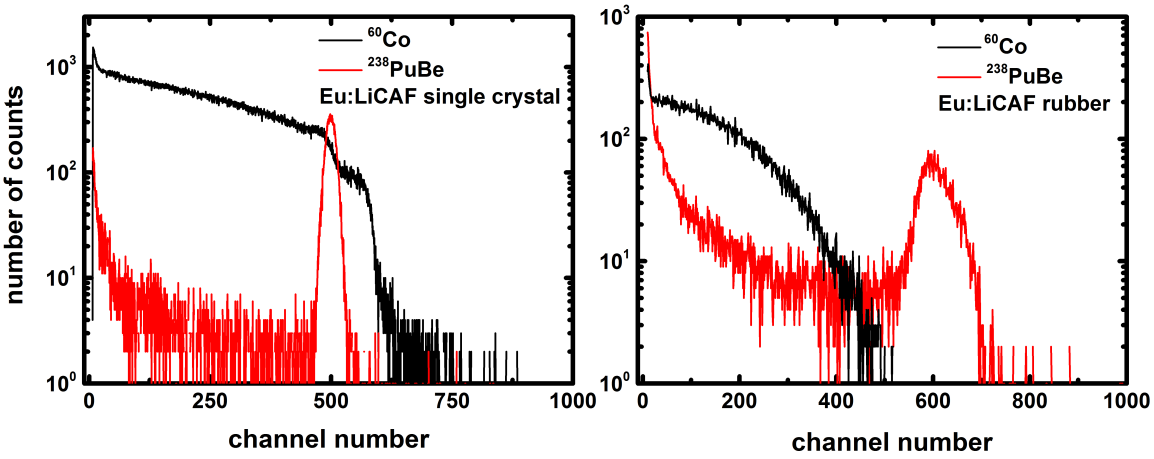

Figure 7.7: *The spectra of a shielded ^{238}PuBe source recorded with the Eu:LiCAF single crystal and Eu:LiCAF rubber. The spectra of the ^{60}Co are also presented.*

figure 7.7. Neutron events appear as sharp Gaussian peak with the FWHM of 4.7%, situated at about 1 MeV GEE. Additionally, a spectrum of the ^{60}Co source is also presented. Unfortunately, gamma-ray events associated with the ^{60}Co source overlap the neutron peak. In the case of the rubber, we observe that the events from the ^{60}Co do not overlap the neutron peak.

The calculations of ε_{PuBe} from the equation 7.1 showed that the efficiency for thermal neutron detection for the single crystal is about 60%, whereas the efficiency for the rubber is much less - about 20%. The measurement confirmed this results. Both Eu:LiCAF are characterized by lower neutron detection efficiency than Ce:LiCAF samples, which is caused by a lower ^{6}Li atoms content for these samples than for Ce-doped ones.

Measurements with an intense ^{60}Co radionuclide source were also performed. Using the gamma source with the activity of 7 MBq we increased the ambient background to 10mR/h and we checked how many events from gamma-rays occur in the neutron window. The value of $\varepsilon_{int\gamma}$ was estimated as 10^{-4} for the single crystal, and 10^{-6} for the rubber scintillator. The gamma-ray sensitivity of the rubber Eu:LiCAF is much less than for the single crystal, because the grains have less dimension than the range of primary electrons.

7.4 The scintillation screen with light readout by wavelength shifting fibers

The tested detector is a phosphor screen based on ZnS(Ag) and ^{6}LiF (containing 95% of ^{6}Li atoms) and WLS fibers. The powder of the transparent ZnS(Ag) has an emission spectrum in the range of blue and ultraviolet light, therefore a wavelength-shifter is necessary to match the maximum emission of the scintillator to the spectral response of the photomultiplier tube. These scintillation system benefits from both a relatively high density of neutron capture target nuclei, and a homogeneous mixture of neutron moderator and capture material. However, ZnS(Ag) can only be obtained as a powder. ^{6}LiF is admixed to ZnS(Ag), and the combination of these compounds is mixed with an organic binder to form a scintillating sheet. Granular structure of the scintillator, causes a self-absorption and scattering of light. The screen was developed as a replacement of ^{3}He proportional counters, and the prototype was tested in Los Alamos National Laboratory in early 2000s [76].

7.4.1 Neutron and gamma-ray response of the ZnS(Ag)/^{6}LiF

The tested detector (see figure 4.9 in section 4.3.5 of chapter 4) is a single flat paddle with 1050 cm^2 sensitive area and one light redout by the photomultiplier tube. The experimental setup for the detector tests is similar to the setup used for testing organic scintillators (see section 5.2 in chapter 5).

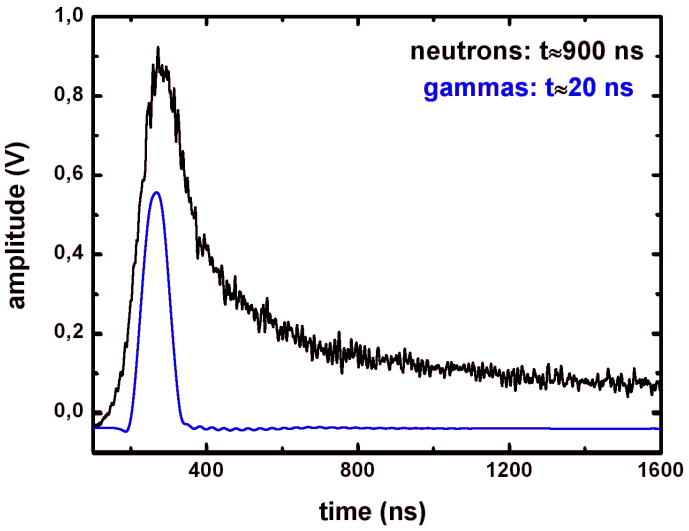

Figure 7.8: *Averaged, gated pulses recorded with BC-704 scintillation screen irradiated with gamma-rays and neutrons [IV].*

The detector is sensitive not only to thermal neutrons, but also to gamma-rays, which is mainly related to gamma-ray detection in thin plastic fibers. However, the problem of gamma-ray sensitivity can be overcome through pulse shape processing techniques. In the case of the tested detector, intrinsic differences of the excitation processes associated with neutron and gamma-ray interactions allow these particles to be separated via the PSD technique. The light pulses from gamma-rays and neutrons are presented in figure 7.8. The differences in decay time constants are extremely large - for gamma-rays it is on the level of nanoseconds, whereas for neutrons the light pulse has a decay time of a microsecond. Note that the pulse response of gamma-rays is affected by a light transport in the detector and a slow response of spectrometric photomultiplier, fortunately negligible in a comparison to the response of neutrons.

Two-dimensional plot of ZC time as a function of pulse height recorded for the tested

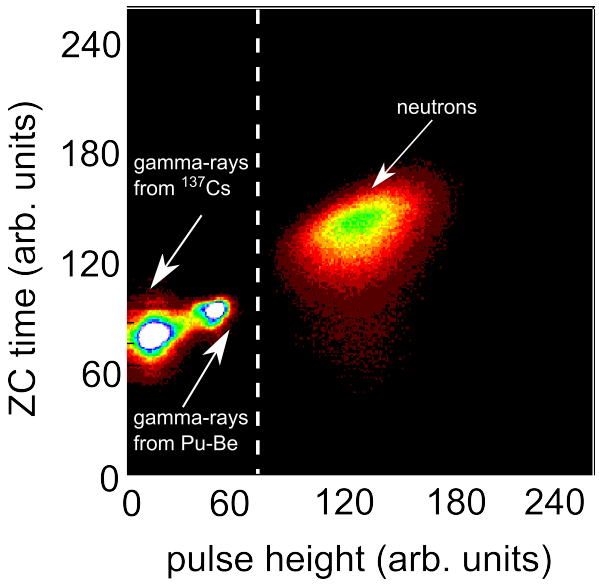

Figure 7.9: *A two-dimensional plot of ZC time as a function of pulse height recorded with ^{6}LiF/ZnS(Ag) irradiated with the ^{137}Cs and the ^{238}PuBe [IV].*

detector under irradiation of a moderated with 2.5 cm of polyethylene ^{238}PuBe is presented in figure 7.9 We can observe well discriminated events from gamma-rays and neutrons. It is well seen that events generated by gamma-rays are have much lower amplitude, than those generated by neutrons. The range of gamma-rays is determined by the interaction with thin fibers - excited electrons deposit just part of their energy according to the equation:

$$\Delta E = (\frac{-dE}{dx})_{avg} \cdot t \tag{7.2}$$

where *t* is the fiber thickness, and $(\frac{-dE}{dx})_{avg}$ is the *linear stopping power* [2] averaged over the energy of the particle while in the absorber.

For low energies, the electron range is less than the detector thickness, but for higher energies, only a portion of incident energy is deposited. Therefore, the energy cut–off in the case of 4.4 MeV and 6.13 MeV gamma–rays is the same (see figure 7.10).

7.4.2 Neutron detection efficiency and gamma-ray sensitivity

According to ANSI standards, to measure the neutron detection efficiency, we used a calibrated ^{252}Cf source yielding 4.5×10^{5} n/s, moderated with 2.5 cm of polyethylene and

[2] *Linear stopping power* – the differential energy loss for the particle within the material divided by the differential path length

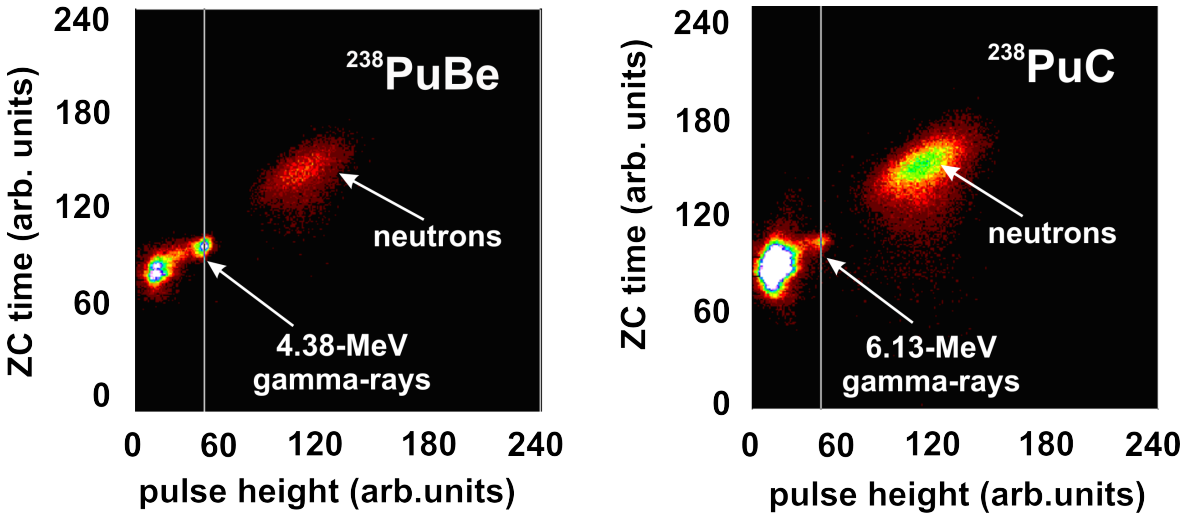

Figure 7.10: *Two–dimensional plots of ZC time as a function of pulse height measured for ZnS(Ag)/^{6}LiF irradiated with the ^{238}PuBe and the ^{238}PuC [IV].*

surrounded by 2 cm of lead to reduce gamma–ray flux. The absolute neutron detection efficiency (ε_{abs}) for such a source located 2 m perpendicular to the geometric midpoint of the detector shall be greater than 2.5 cps/ng of the ^{252}Cf. We also performed the measurements of the ($\varepsilon_{int\gamma n}$) with an intense ^{137}Cs radionuclide source, increasing the ambient background to 10 mR/h.

To calculate the ε_{abs} and the $\varepsilon_{int\gamma n}$ for the tested detector, we defined the optimal lower level (LL) value, which will be the gamma cut–off point for the detector. The position of the gamma cut-off point should be optimized to assure maximum neutron detection efficiency with maximum gamma-ray rejection, which stands for gamma sensitivity within neutron integration window. Figure 7.11 shows the ε_{abs} and the $\varepsilon_{int\gamma n}$ as a function of LL. It is seen that above 2200 channel, ε_{abs} is kept on the level of 0.02 cps/ng, whereas the $\varepsilon_{int\gamma n}$ is assumed as 1.53 ($\pm$ 0.53)$\times 10^{-10}$.

To compare the results obtained with the scintillation screen, we also tested the ^{3}He counter (5.08 cm in diameter and 53.34 cm long) under the pressure of 2 atmospheres. The detector was made od 1 mm thick steel, and it was surrounded by a polyethylene of 5.08 cm thickness on the back and sides, and 2.54 cm on the front. The reference ^{3}He counter showed in these conditions the ε_{abs} of 0.3 cps/ng. The measurements performed without the polyethylene gave the results of 0.016 cps/ng, which is about 19 times less than obtained with the moderator around the detector. In the case of the scintillation screen, the tests were

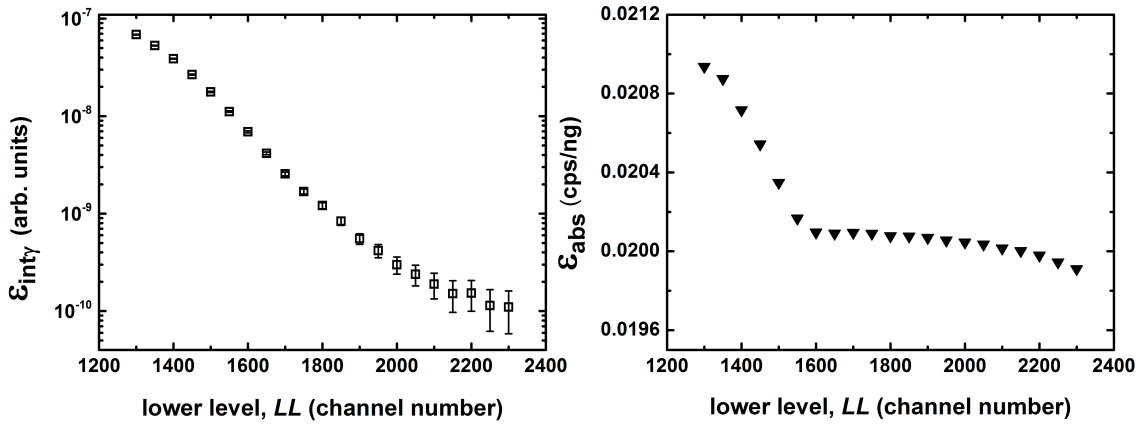

Figure 7.11: *The ε_{abs} and the $\varepsilon_{int\gamma n}$ of the scintillation screen as a function of LL (in channels) [IV].*

performed without the polyethylene moderator and the result of ε_{abs} was similar to obtained with ^{3}He counter without the polyethylene. By comparing the efficiency of the ^{3}He counter with and without the polyethylene, we expect that the ε_{abs} of the scintillation screen with additional, external moderator will be also almost 20 times better than measured (on the level of $\sim$0.4 cps/ng), thus even better than that of the reference ^{3}He detector.

The revised concept of neutron detector - the scintillation screen with ^{6}LiF/ZnS(Ag) and WLS fibers - is a promising idea of an alternative detector used in the RPMs for homeland security applications. The detector is sensitive to thermal neutrons and gamma-rays. However, intrinsic differences of the excitation processes associated with neutron and gamma–ray interactions in the tested detector, allow these events to be separated via the PSD technique. The gamma rejection of a single flat paddle is on the level of 10^{-10}. To obtain the neutron efficiency on the level of ^{3}He counter, additional external polyethylene moderator is required. The RPM system based on the tested detector should consist of at least six such panels, or one panel with six times larger surface, surrounded by the moderator.

Chapter 8

Summary

Science and technology play a key role in the prevention of radiological threats and nuclear terrorism. The growing deployment of detection systems for identification of nuclear materials has renewed interest in the field of radiation detection research. The applications for homeland security range from portable hand-held units, to large portal monitors located at ports of entry. Passive radiation monitor systems employ both gamma-ray and neutron detection. In the detection of gamma-ray signatures, classical, cost-effective plastic scintillators are utilized. The identification of the isotopes requires more advances spectroscopy systems. The limitation of these systems is the energy resolution of the detectors, or, in the case of germanium detectors, the necessity of cooling.

Illegal transport of SNMs is generally regarded as the matter of the utmost necessity in terrorist risk. These materials, which are used for nuclear weapons production, emits not only gamma-ray and alpha signatures, but also fast neutrons. SNMs can easily be hidden in the transport chain, and with standard detection portals not being able to find such materials, because energy gamma-rays and alpha signatures can be easily shielded. Additionally, naturally occurring radiation material (NORM) commonly meet in commerce, worsen the problem of SNM detection. Therefore, fast neutron detection becomes an important issue on the case of SNM detection, because of low neutron background in the normal conditions, and different shielding characteristics in comparison to alpha particles and gamma-rays. The most common neutron detectors installed at the borders, are large-area ^{3}He proportional counters enclosed in a polyethylene moderator. The use of ^{3}He as a neutron detector medium has

the great advantage, because it is almost only sensitive to neutrons, and its sensitivity in ^{3}He-based proportional counters to gamma-rays is negligible. However, the shortage of ^{3}He caused an urgent need to replace the detection systems based on this isotope, to alternative technologies. The data presented in 2010 show that the average demand of the ^{3}He in the United States was about 65 m^3 per year, whereas the supply was only about 20 m^3 per year [6]. The shortage of the ^{3}He entailed an increase in the price of this isotope - from about $ 200 per liter up to $ 3000 per liter [7], and have been the ground for searching the alternative technologies for neutron detection, either based on the isotopes with high cross-section for nuclear reactions with neutrons (^{6}Li, ^{10}B, or gadolinium isotopes), or based on light nuclei, on which neutrons can be scattered (^{1}H, ^{4}He). The ^{3}He is used not only as a neutron detection material, but also in other branches of technology, such as such as well logging in the oil and gas industry, in medical applications, basic research projects in nuclear and condensed matter physics, and in ^{3}He-based refrigerators.

The need of an alternative technology for neutron detection became a motivation for the studies in many laboratories in the world, as well as for the experiments presented in this thesis. Close cooperation with CEA in Saclay, LLNL in the United States, and ISMA in Kharkov, as well as many commercial companies, such as Tokuyama Corporation in Japan, or Scionix in the Netherlands allowed the studies of the present status on neutron detection, as well as the tests of novel scintillators.

A part of the reported experiments were focused on organic scintillators for fast neutron detection. The study showed that from all organic scintillators, the best PSD performance, especially in low energy region, have single crystals. Trans-stilbene ($C_{14}H_{12}$) is attractive neutron detector, because of its very efficient discrimination between gamma rays and neutrons. Moreover, it is a solid, non-flammable and non-toxic material. The use of stilbene in industry, medicine, and research applications, where large volumes are required, has been limited due to low commercial availability of the crystals grown using the traditional method (Bridgman melt growth). The alternative technology of grinding boules of organic crystals into small crystalline grains was developed by the laboratory in Kharkov. Composite scintillators are made of few millimeters-sized grains introduced into a silicone matrix. The measurements with stilbene- and *p*-terphenyl-based composites exhibited a good PSD performance, comparable to organic liquid scintillators, but large opacity with growing volume of

the scintillators, which leads to decrease the light output. Therefore, composite scintillators can be only used as large in surface, but small in thickness detectors.

Recent news [54] show that a solution-growth process was implemented to produce large, high-quality stilbene single crystals. The dimensions of the stilbene provided by Inrad Optics company are up to 10.16 cm in height cylinders. They have also developed methods for fabrication of stilbene into a variety of geometries, such as cylinders, bars, and thin plates. The reported FoM of the stilbene is 4.7 at 500 keVee for 2.54 cm $\times$ 2.54 cm cylinder, which is about 1.5 times better than the FoM for EJ301 liquid scintillator measured in our laboratory.

Up to 2014, organic liquids were the only organic scintillators that were available in large volumes. Classical liquid scintillators are usually low-flashpoint, with the exception of EJ309, which has a flashpoint of 144°C. There are also ^{10}B-loaded liquid scintillators available, which have the capabilities to detect also low-energy neutrons via the ^{10}B(n,α) reaction, and enhance the total neutron detection efficiency. The study presented in this thesis showed that liquid scintillators are efficient neutron detectors, with the performance comparable to ^{3}He proportional counters. Moreover, the measurements of light output curves for several liquid scintillators showed that high flashpoint liquid scintillators have higher light yield from neutrons in low energy region, than classical xylene-based ones. However, gamma-ray discrimination of liquid scintillators is still not enough efficient to meet ANSI requirements for RPM purposes. The comparative measurements showed that ^{3}He counter has 10 times better neutron/gamma discrimination than ^{10}B-loaded EJ309B5 with additional shielding.

Organic plastic scintillators with PSD capabilities are solid state alternative to liquid scintillators, which were developed in various laboratories. Plastics developed in Lawrence Livermore National Laboratory are currently in the commercial stage, and are sold under the name of EJ299-33. The studies on plastic scintillators showed that the PSD becomes less efficient with increasing volume of the scintillator. The comparative measurements of large plastic samples and liquid EJ309 with the same dimension exhibited that plastic have still lower neutron/gamma discrimination capabilities than liquids, becoming critical at low energy, where neutron and gamma-ray events are hardly separated. Although liquid scintillators have still better PSD performance, plastics give a reasonable alternative for neutron detection with gamma discrimination in several applications, especially in those where the risk of leakage of liquid scintillators is the main problem. The advantage of plastic scintillators is

their robustness, non-toxicity and inflammability.

Organic scintillators, especially high flashpoint EJ309 liquid, and plastics, can be used in homeland security applications as primary, hand-held detectors, where its high sensitivity to neutrons is an advantage. In 2013, the collaboration of University of Padova and CAEN SpA presented the idea of a system called *Plutonium Hunter* – the portable spectrometric neutron/gamma instrument, based on organic liquid EJ309 scintillator. The authors claimed that the system is dedicated for the identification of shielded and unshielded neutron sources, and also can be used for plasma diagnostic.

Slow neutron detectors presented in the thesis are based on ^{6}Li(n,α) reaction. Large Q-value of the reaction offers some real advantage in discrimination against gamma-rays, and other low-amplitude events. Because lithium reaction goes exclusively to the ground state, always the same energy is imparted to the reaction products for each decay, and the pulse height distribution is a single gaussian peak. Moreover, there are no gamma-rays emitted in the ^{6}Li(n,α) reaction.

Crystalline lithium iodide is the oldest lithium-based scintillator with gamma-ray spectrometry capabilities, which can be used in hand-held isotope identifiers with simultaneous neutron detection. The results obtained with ^{6}LiI(Eu) showed that the neutron peak is situated at about 3.5 MeV GEE, and is clearly separated from the gamma-ray background. Due to the high neutron detection efficiency of ^{6}LiI(Eu), the crystal detected neutrons emitted from small amount of fissile materials. The main disadvantage of ^{6}LiI(Eu) it its extreme hygroscopicity, and difficulty in growing large sizes.

Lithium-enriched glasses, as well as LiCAF crystals are low-density scintillators, which can be used as efficient detectors for thermal neutron counting. The neutron/gamma discrimination of GS20 is very good - at the level of 10^{-7}, which meet the ANSI standards ($\leqslant 10^{-6}$) for the neutron detectors in homeland security applications. Moreover, the flexibility in the design of the GS20 allows to manufacture the detector in various shapes and sizes. However, due to low effective atomic number of GS20, it is impossible to perform gamma-ray spectroscopy. Ce:LiCAF have also very good neutron/gamma discrimination of about 10^{-6}, but the light yield of these scintillators is very low, which limits their wider applications.

The results obtained with Eu:LiCAF scintillators indicated that they have significantly

higher light yield, than Ce:LiCAF ones. However, intrinsic gamma-neutron detection efficiency is lower than those measured with Ce:LiCAF crystals - the gamma-ray events from ^{60}Co source overlap the neutron peak. The $\varepsilon_{int\gamma n}$ value of 10^{-4} eliminates Eu:LiCAF single crystals from the possible candidates to replacement of ^{3}He detectors in homeland security applications. Recently developed Eu:LiCAF rubber, which consists of small crystalline grains have improved gamma-ray discrimination to the value of 10^{-6} , which is related to small size of the grains, much lower than a range of secondary electrons produced by gamma-rays. Only a fraction of gamma-ray energy is deposited in the rubber scintillator, whereas the deposition of energy by ^{6}Li(n,α) reaction products remains the same, as for single Eu:LiCAF crystals.

Table 8.1 presents the groups od the studied neutron detectors together with their advantages and drawbacks as possible replacements to ^{3}He proportional counters in homeland security applications. The two most promising technologies are liquid scintillators (under condition that additional reduction of gamma-ray flux by the external shielding is performed), and the BC-704 scintillation screen with the WLS fibers. The measurements with BC-704 screen performed in our laboratory showed that the scintillator has very low gamma-ray sensitivity, which is related to detection of gamma-ray events in thin plastic fibers. The detector does not contain any hazardous materials, therefore it can be installed at the border crossing. If the detector is built with sufficiently large dimension, it meets the ANSI requirements for the RPMs. Therefore, the system based on the ZnS(Ag)/^{6}LiF can be the most attractive alternative to the RPMs based on the ^{3}He tubes, in the crisis of ^{3}He supply.

Table 8.1: *The studied neutron detectors as possible replacements to ^{3}He proportional counter in homeland security applications.*

detection method	scintillators	advantages	disadvantages
fast neutron elastic scattering	liquids	good n/γ separation efficient neutron detection possible to obtain in large volumes	toxicity flammability poor n/γ separation in large gamma-ray fluxes
	composites	cost-effective solid solution possibility to obtain in large surfaces	opacity PSD decreases with increasing thickness
	plastics	non-toxic inflammable solid alternative to liquid scintillators	n/γ discrimination poorer than for liquids PSD decreases with increasing volume
capture reaction on ^{6}Li	LiI(Eu)	gamma-ray spectroscopy neutron counting good n/γ separation	hygroscopic only small samples available
	GS20 lithium glass	neutron counting various shapes and sizes good n/γ separation	no gamma-ray spectroscopy large FHWM of the neutron peak
	LiCAF	neutron counting Ce:LiCAF - good n/γ separation Eu:LiCAF - high light yield LiCAF rubber - large sizes available, good n/γ separation	no gamma-ray spectroscopy Ce:LiCAF - low light yield Eu:LiCAF - poor n/γ separation LiCAF rubber - poorer neutron detection efficiency
	ZnS(Ag)/6LiF	good n/γ discrimination large surfaces available	PSD necessary

Appendices

Appendix A

Kinematic of elastic collision - non-relativistic approach

Most scattering experiments with the target are carried out in the laboratory (LAB) system in which the target is initially at rest, whereas the projectile is moving. However, the calculations of the cross sections are easier to perform within the inertial center-of-mass (CM) frame in which the center of mass of the projectile-target system is at rest before and after collision. In the CM system, the momentum sum of the incident particle and the target nucleus is zero. The total cross section is the same for both frames, since the total number of collisions is independent of the frame in which the observation is carried out. However, **the differential cross section** $d\sigma/d\Omega$ is not the same, because the scattering angles are different. The transformation from the CM to the LAB frame is necessary. The LAB and the CM systems are presented in figure A.1 The symbols to be used in the equations are as follows:

m_1 – the mass of an incoming particle (neutron)

m_2 – the mass of a target nuclei

v_1 – velocity of an incoming neutron in the CM frame

V_1 – velocity of an incoming neutron in LAB frame

v_2 – velocity of the target particle in CM frame

v_1' – velocity of the neutron after collision in CM frame

V_1' – velocity of the neutron after collision in LAB frame

v_2' – velocity of recoil particle in CM frame

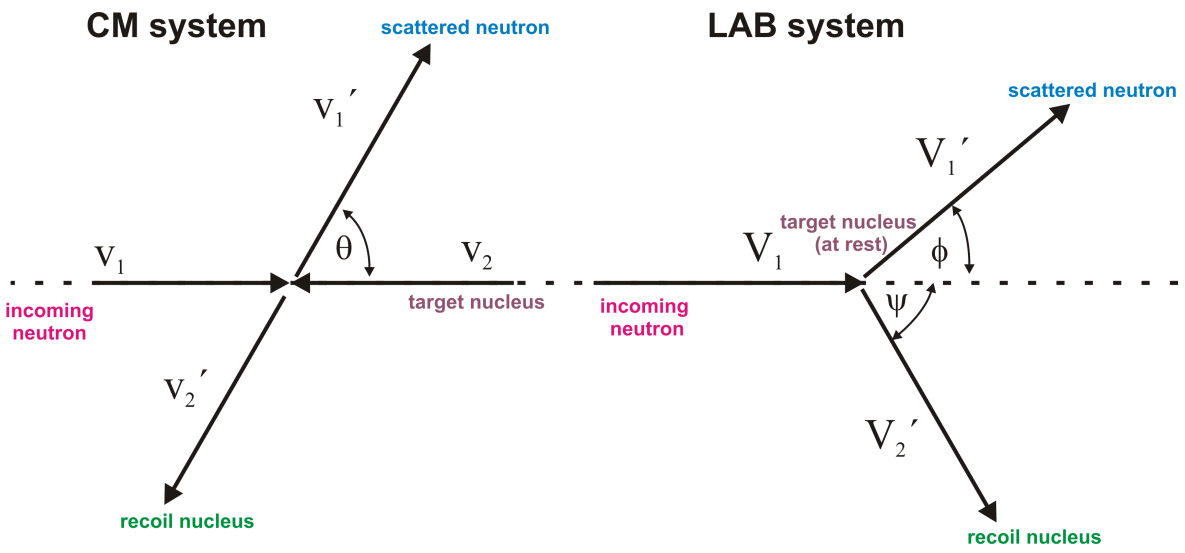

Figure A.1: *Scattering in the CM and the LAB frames.*

V_2' – velocity of recoil particle in LAB frame

In the CM frame from the momentum conservation we obtain the relationship

$$m_1\overrightarrow{v_1} + m_2\overrightarrow{v_2}m_1 = \overrightarrow{v_1'} + m_2\overrightarrow{v_2'}. \tag{A.1}$$

In the LAB frame that is moving with the uniform velocity -$\overrightarrow{v_2}$ with respect to the CM frame. Therefore, in the LAB frame the incoming neutron has initial velocity of

$$\overrightarrow{V_1} = \overrightarrow{v_1} - \overrightarrow{v_2}. \tag{A.2}$$

The scattered neutron has a velocity of

$$\overrightarrow{V_1'} = \overrightarrow{v_1'} - \overrightarrow{v_2} \tag{A.3}$$

and the velocity of recoil particle is

$$\overrightarrow{V_2'} = \overrightarrow{v_2'} - \overrightarrow{v_2}. \tag{A.4}$$

In the CM frame, both particles are scattered through the same angle θ. In the LAB frame the neutron and the target particle are scattered by the different angles: ϕ and ψ, respectively. From the momentum conservation A.1 and simple trigonometry we can calculate the Cartesian components of the velocities:

$$\overrightarrow{v_1} = \begin{pmatrix} v_1 \\ 0 \end{pmatrix} \tag{A.5}$$

$$\overrightarrow{v_2} = \begin{pmatrix} -\frac{m_1}{m_2} v_1 \\ 0 \end{pmatrix} \tag{A.6}$$

$$\overrightarrow{v_1'} = \begin{pmatrix} v_1 \cos\theta \\ v_1 \sin\theta \end{pmatrix} \tag{A.7}$$

$$\overrightarrow{v_2'} = \begin{pmatrix} -\frac{m_1}{m_2} v_1 \cos\theta \\ -\frac{m_1}{m_2} v_1 \sin\theta \end{pmatrix} \tag{A.8}$$

$$\overrightarrow{V_1} = \begin{pmatrix} (1 + \frac{m_1}{m_2}) v_1 \\ 0 \end{pmatrix} \tag{A.9}$$

$$\overrightarrow{V_1'} = \begin{pmatrix} (\frac{m_1}{m_2} + cos\theta) v_1 \\ v_1 \sin\theta \end{pmatrix} \tag{A.10}$$

$$\overrightarrow{V_2'} = \begin{pmatrix} (\frac{m_1}{m_2} v_1 (1 - cos\theta) \\ -\frac{m_1}{m_2} v_1 \sin\theta \end{pmatrix} \tag{A.11}$$

In the CM frame ε is the total energy described by the equation

$$\varepsilon = \varepsilon_1 + \varepsilon_2 = \varepsilon_1' + \varepsilon_2' \tag{A.12}$$

where ε_1 and ε_2 are the kinetic energies before the collision of a neutron and target particle, respectively; whereas ε_1' and ε_2' are kinetic energies for these particle after collision. In the case of the LAB frame, the total energy E is equal to the initial neutron energy E_1 and to the sum of energy of scattered neutron E_1' and recoil particle E_2' after the collision

$$E = E_1 = E_1' + E_2' \tag{A.13}$$

From the above energy conservation definitions and equations (A.5 - A.11) we can assume that the total energy in the LAB frame is greater than the total energy in the CM frame

$$E = (fracm_1 + m_2 m_1)\varepsilon \tag{A.14}$$

In the CM frame

$$\varepsilon_1 = \varepsilon_1' = (\frac{m_2}{m_1 + m_2})\varepsilon \tag{A.15}$$

$$\varepsilon_2 = \varepsilon_2' = (\frac{m_1}{m_1 + m_2})\varepsilon \tag{A.16}$$

In the LAB frame

$$E_1' = [\frac{m_1^2 + 2m_1 m_2 cos\theta + m_2^2}{(m_1 + m_2)^2}]E \tag{A.17}$$

$$E_2' = [\frac{2m_1 m_2(1 - cos\theta)}{(m_1 + m_2)^2}]E. \tag{A.18}$$

From the equations A.17 and A.18 we see that, in the LAB frame, the energy distribution before and after collision is different. The relation between the angles θ in the CM frame and ϕ and ψ in the LAB frame is as follows

$$\tan\phi = \frac{sin\theta}{cos\theta + m_1/m_2} \tag{A.19}$$

$$\tan\psi = \frac{sin\theta}{1 - cos\theta} = tan(\frac{\pi}{2} - \frac{\theta}{2}) \tag{A.20}$$

Considering the neutron elastic scattering on a target with a mass $m_2 =$ **A** and assuming that the mass of a neutron $m_1 = 1$, from the Eq.A.18 and A.20 we can calculate the energy distribution of a recoil nucleus E_2'

$$E_2' = (\frac{4A}{(1 + A)^2} cos^2\psi)E \tag{A.21}$$

In the case when $\mathbf{m_1 = m_2}$ (**neutron scatters on a proton**) equation A.19 yields

$$\tan\phi = \frac{sin\theta}{cos\theta + 1} = \tan(\theta/2). \tag{A.22}$$

Hence, the scattering angle of the first particle in the LAB frame is half of the scattering angle in the CM frame

$$\phi = \theta/2. \tag{A.23}$$

From the equations A.17 and A.23 we obtain the energy distribution between the two particles in the LAB frame, when their masses are equal

$$E_1' = (\frac{1 + cos\theta}{2})E = cos^2(\theta/2)E = cos^2(\phi)E. \tag{A.24}$$

$$E_2' = (\frac{1 - cos\theta}{2})E = sin^2(\theta/2)E = sin^2(\phi)E. \tag{A.25}$$

In the paper (Barshal and Kanner 1940) authors have shown that the energy distribution of recoil particles in the LAB frame is the same as the angular distribution of neutrons scattered in the CM frame.

Appendix B

Angular distribution of neutron energy in fusion reactions

In the LAB system, where tritium is initially at rest and deuterium ions (deuterons) are moving, a d-t reaction can be depicted as presented in figure B.1. The momentum conservation leads to the following equation

$$m_d\overrightarrow{v_d} = m_\alpha\overrightarrow{v_\alpha} + m_n\overrightarrow{v_n} \tag{B.1}$$

where m_d and v_d are the mass and the velocity of deuterium, m_α and v_α are the mass and the velocity of the alpha particle, and m_n and v_n are the mass and the velocity of the neutron. The cartesian components of the individual velocities can be written as

$$\overrightarrow{v_d} = \begin{pmatrix} v_d \\ 0 \end{pmatrix} \tag{B.2}$$

$$\overrightarrow{v_\alpha} = \begin{pmatrix} v_\alpha \cos\psi \\ -v_\alpha \sin\psi \end{pmatrix} \tag{B.3}$$

$$\overrightarrow{v_n} = \begin{pmatrix} v_n \cos\phi \\ v_n \sin\phi \end{pmatrix} \tag{B.4}$$

The relationship between the momentum and the kinetic energy

$$p = mv = (2Em)^{1/2} \tag{B.5}$$

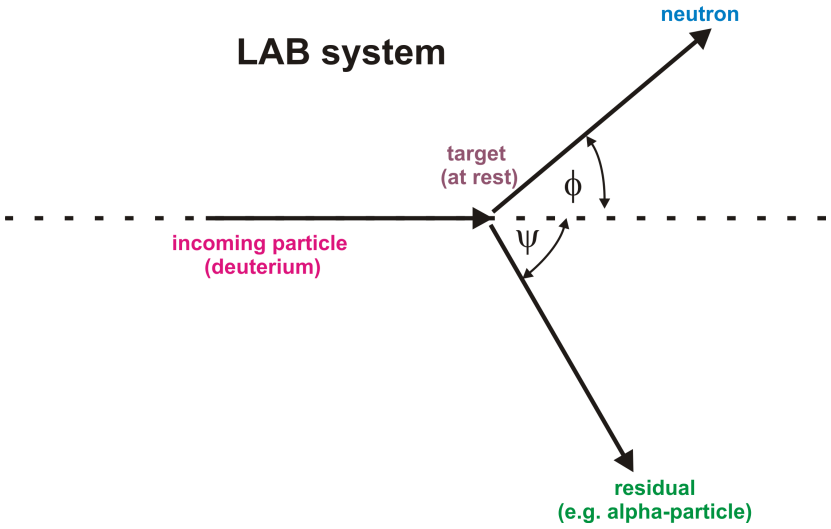

Figure B.1: *Kinematics od fusion reaction in the LAB system.*

substituted into the cartesian components from equations B.2, B.3 and B.4 leads to the equations

$$(2m_dE_d)^{1/2} = (2m_\alpha E_\alpha)^{1/2}\cos\psi + (2m_nE_n)^{1/2}\cos\phi, \tag{B.6}$$

$$0 = -(2m_\alpha E_\alpha)^{1/2}\sin\psi + (2m_nE_n)^{1/2}\sin\phi. \tag{B.7}$$

Squaring and adding the B.6 and B.7 we obtain

$$m_dE_d - 2(m_dE_dm_nE_n)^{1/2}\cos\phi + m_nE_n = m_\alpha E_\alpha. \tag{B.8}$$

The energy conservation for d-t reaction gives a following relationship

$$E - d + Q = E_\alpha + E_n. \tag{B.9}$$

Plugging the energy of the alpha particle from the equation B.9 to the equation B.8 we can calculate the energy of the emitted neutron as a function of the angle ϕ

$$En_{(}\phi) = (\frac{(m_dm_nE_d)^{1/2}\cos\phi + [m_dm_nE_d\cos^2\phi + (m_\alpha + m_n)(m_\alpha Q + m_\alpha E_d - m_dE_d)]^{1/2}}{m_\alpha + m_n})^2. \tag{B.10}$$

In the LAB frame, the neutron energy is dependent on the angle ϕ between the target and the neutron (see figure..).

In the case of d-d reaction, where the neutron and ^{3}H are released, the equation B.10 takes the form of

$$En_{(}\phi) = (\frac{(m_dm_nE_d)^{1/2}\cos\phi + [m_dm_nE_d\cos^2\phi + (m_t + m_n)(m_tQ + m_tE_d - m_dE_d)]^{1/2}}{m_t + m_n})^2. \tag{B.11}$$

Appendix C

Gamma-ray interactions with matter

The interaction of gamma-rays in matter is described mainly by four processes: the photoelectric absorption, Compton scattering, pair production and Rayleigh scattering. In the case of scintillators for neutron detection, gamma radiation sources are used only for photoelectron yield estimation, or calibration of neutron energy in electron equivalent units. Only two first phenomena are important when taking into account typical radioisotope sources (such as ^{241}Am, ^{137}Cs, ^{22}Na, ^{60}Co), therefore two later effects are not described in the thesis. Rayleigh scattering does not produce free electrons that ionize the medium. This interaction occurs mainly for low-energy X-rays (15-30 keV) and causes the electrons in the scattering atom to oscillate in phase.

C.1 Photoelectric absorption

In the photoelectron effect the incident gamma-ray undergoes an interaction with an atom and then completely disappears. This interaction leads to the formation of a photoelectron from one of the bounded electrons, with the kinetic energy of $h\nu$ minus the binding energy of the electron in its shell. Only the bound electrons undergo photoelectric absorption, and the probability of this interaction is the highest for the most tightly bound electrons with the lowest energy (located at the K shell of the atom). Photoelectric effect is predominant for low- energy gamma- and X-rays, and is enhanced in materials with a high atomic number [27]. Photoelectric absorption is the best process when we want to measure the energy of

the incident gamma-ray. The total electron kinetic energy is equal to the original gamma-ray energy and is always the same for monoenergetic gamma-rays. Therefore, for a series of photoelectric events, the differential distribution of electron kinetic energy would be a delta function (photopeak, or full-energy peak). However, the single peak is never a delta function, because of a finite energy resolution of the detector. Theretofore, we observe a Gaussian-like peak instead of an ideal delta-function.

C.2 Compton scattering

The result of a Compton scattering is the elastic collision between the incident photon and an unbounded electron. The incident photon, transferring a part of its energy to the kinetic energy of an electron, is deflected through the angle θ with respect to its original direction (in the LAB system). Since the energy transferred to the electron can cover any part of the initial photon energy, all scattering angles are possible [27]. The energy of the deflected photon can be expressed by the Compton formula

$$E_{phe} = E_{\gamma} - \frac{E_{\gamma}}{1 + mc^2(1 - cos\theta)}. \tag{C.1}$$

where E_{phe} is the energy of the photoelectron, E_{γ} is the energy of the incident photon, mc^2 is the rest-mass of the electron (511 keV).

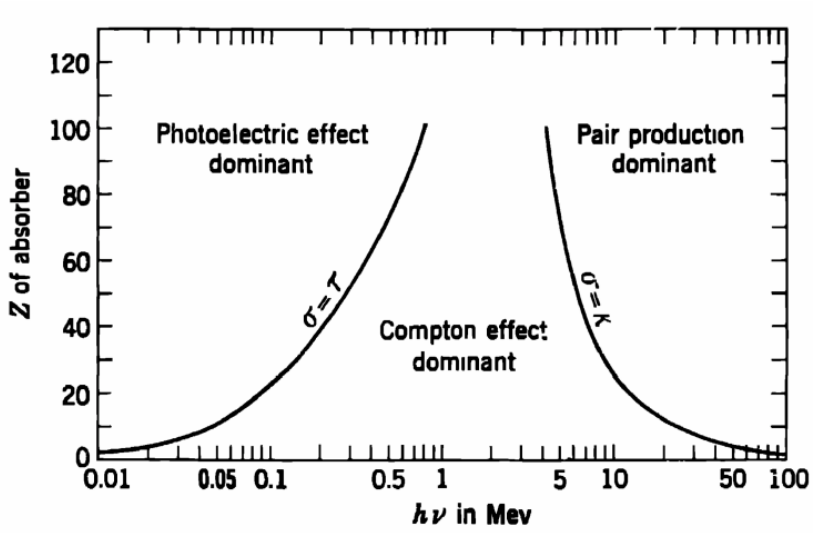

Figure C.1: *Relative importance of three major types of gamma-ray interaction. The solid lines indicate the values for which two neighboring effects are equally probable (reprint from [152]).*

The total probability of a Compton scattering per atom of the scintillating material depends on the number of scatter electron targets available, which increases linearly with atomic number [27]. The Compton scattering is a predominant effect for gamma-ray energies typical for radioisotope sources. Energy resolution is an important parameter in radiation spectroscopy, where the measurement of the energy distribution of incident radiation is of importance. This is the extent to which the detector can resolve slightly different energies and is defined as the *Full Width at Half Maximum* (FWHM) divided by the location of the peak centroid H_0, expressed as percentage [27]

$$\Delta E/E = \frac{FWHM}{H_0}. \tag{C.2}$$

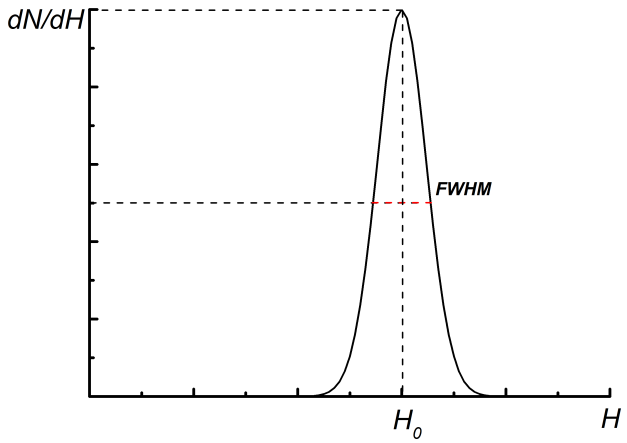

Figure C.2: *Definition of energy resolution of the detector.*

Bibliography

[1] http://www.nrc.gov/materials/sp nucmaterials.html, "**U.S. Nuclear Regulatory Comission web page**," (2013).

[2] D.Reilly *et al.*, *Passive Nondestructive Assay of Nuclear Materials* (United States Nuclear Regulatory Commission, 1991) p. 359.

[3] http://www.world-nuclear.org/info/Safety-and-Security/Radiation-and Health/Naturally-Occurring-Radioactive-Materials-NORM/, "**Naturally Occuring Radioactive Materials**," (2014).

[4] R. T. Kouzes *et al.*, *Nucl. Instr. Meth. A* **623**, 1035 (2010).

[5] R. T. Kouzes, *The 3-He Supply Problem*, Tech. Rep. (PNNL Technical Report 18388, 2009).

[6] R. Kouzes and J. H. Ely, *Status summary of ^{3}He and neutron detection alternatives for homeland security*, Tech. Rep. (Pacific Northwest National Laboratory, 2010).

[7] T. Feder, *Physics Today* **62**, 21 (2009).

[8] J. L. Lacy *et al.*, *Nucl. Instr. Meth. A* **652**, 359 (2011).

[9] http://www.crystals.saint gobain.com, "**Neuport Detection System**," (2011).

[10] E. Rutherford, Proceedings of the Royal Society of London A **97** (1920).

[11] H. Becker and W. Bothe, *Zeitschrift für Physik* **66**, 5 (1930).

[12] H. Becker and W. Bothe, *Zeitschrift für Physik* **76**, 7 (1932).

[13] I. Joliot-Curie and F. Joliot-Curie, *C. R. Acad Sci Gen.* **194**, 273 (1932).

[14] J. Chadwick, *Nature* **129**, 213 (1932).

[15] J. Chadwick, *Proc. Math. Phys. Eng. Sci.* **142**, 1 (1933).

[16] W. Heisenberg, *Zeitschrift für Physik* **77**, 1 (1932).

[17] W. Heisenberg, *Zeitschrift für Physik* **78**, 156 (1932).

[18] W. Heisenberg, *Zeitschrift für Physik* **80**, 587 (1933).

[19] D. Ivanenko, *Nature* **129**, 798 (1932).

[20] D. Ivanenko, *C. R. Acad Sci Gen.* **195**, 439 (1932).

[21] H.Yukawa, *Proc. Phys. Math. Soc. Japan* **17**, 48 (1935).

[22] P. J. Mohr *et al.*, *Rev. of Modern Physics* **84**, 1527 (2012).

[23] J.-L. Basdevant *et al.*, *Fundamentals in Nuclear Physics* (*Springer*, 2005).

[24] J. Konya and N. Nagy, *Nuclear and Radiochemistry* (*Elsevier*, 2012) pp. 74–75.

[25] http://physics.nist.gov/cuu/Constants/index.html, "**Fundamental Physical Constant**," (2012).

[26] J. Beringer *et al.*, *Phys. Rev. D* **86**, 010001 (2012).

[27] G. F. Knoll, *Radiation Detection and Measurement* (*John Wiley & Sons*, 2010) pp. 30–46.

[28] S. Tavernier, *Experimental Techniques in Nuclear and Particle Physics* (*Springer*, 2010) pp. 23–26.

[29] E. Skrzypczak and Z. Szefliński, *Wstęp do fizyki jądra atomowego i cząstek elementarnych (in Polish)* (*PWN*, 2012) pp. 23–25.

[30] http://atom.kaeri.re.kr/cgi bin/endfplot.pl, "**Cross Section Plotter**," (2000).

[31] A. R. Bohm and Y. Sato, *Phys. Rev. D* **71**, 085018 (2005).

[32] G. Breit and E. Wigner, *Phys. Rev.* **49**, 519 (1936).

[33] N. Carron, *An introduction to the Passage of Energetic Particles through Matter* (*Taylor & Francis*, 2007).

[34] T. Jevremovic, *Nuclear Principles in Engineering* (*Springer*, 2009) pp. 428–430.

[35] A. Kamal, *Nuclear Physics* (Springer, 2014) pp. 507–508.

[36] M. Hamel *et al.*, *Nucl. Instr. Meth. A* **in press** (2014).

[37] T.Gozani *et al.*, *Journal of Instrumentation* **7 C02042** (2012).

[38] V. Niewart, *Spectral Tailoring for Boron Neutron Capture Therapy* (*IOS Press*, 2007).

[39] P. Reeder, *Nucl. Instr. Meth. A* **353**, 134 (1994).

[40] P. Reeder, *Nucl. Instr. Meth. A* **340**, 371 (1994).

[41] A. Harms and G. McCormac, *Nucl. Instr. Meth. A* **118**, 583 (1974).

[42] T. Gozani, *Active Nondestructive Assay of Nuclear Materials: Principles and Applications* (National Technical Information Service Springfield, Virginia (1981)).

[43] O. Batenkov *et al.*, INDC (NDS) **146** (1983).

[44] J. Shultis and R. E. Faw, *Fundamentals of Nuclear Science and Engineering* (*CRC Press*, 2007).

[45] J. Chapman and S. Croft, *The Use of ^{252}Cf for Calibrating Safeguards Monitors*, Tech. Rep. (ORNL, Canberra).

[46] D. Bleuel *et al.*, *Nucl. Instr. Meth. A* **624**, 691 (2010).

[47] N. J. Roberts and L. Jones, *Radiat. Prot. Dosimetry* **126**, 83 (2007).

[48] M. Anderson and R. Neff, *Nucl. Instr. Meth. A* **99**, 231 (1972).

[49] http://www pub.iaea.org/MTCD/Publications/PDF/P1535_web.pdf, "**Neutron generator for analytical purposes**," (2012).

[50] G. Miley and K. Murali, *Inertial Electrostatic Confinement (IEC) Fusion, fundamentals and applications* (*Springer*, 2014).

[51] D. Oliver and G. Knoll, *IEEE Trans. on Nucl. Sci.* **15**, 122 (1968).

[52] W. Hansen and D. Richter, *Nucl. Instr. Meth. A* **476**, 198 (2002).

[53] N. Zaitseva *et al.*, *J. Cryst. Growth* **314**, 163 (2011).

[54] http://inradoptics.com/pdfs/Inrad_WP_Stilbene.pdf, "**Large stilbene crystal datasheet**," (2014).

[55] N. Z. Galunov *et al.*, *IEEE Trans. on Nucl. Sci.* **56**, 904 (2009).

[56] N. Galunov *et al.*, in *NSS-MIC Conference Record*, Vol. 4 (IEEE, 2007) pp. 2469–2475.

[57] J. Harvey and N. Hill, *Nucl. Instr. Meth. A* **162**, 507 (1979).

[58] H. Ross, *Liquid Scintillation Counting and Organic Scintillators* (CRC Press, 1991).

[59] E. Yates *et al.*, *Molecular Crystals* **4**, 165 (1968).

[60] http://www.eljentechnology.com/images/stories/Data Sheets/Liquid Scintillators/EJ309 data sheet.pdf, "**EJ-309 datasheet**," (2010).

[61] F. Brooks *et al.*, *IRE. Trans. Nucl. Sci.* **7**, 35 (1960).

[62] J. Birks, *The theory and practice of liquid scintillation counting* (*Pergamon Press, Oxford U.K.*, 1964).

[63] P. Blanc *et al.*, *IEEE Trans. on Nucl. Sci.* **61**, 1995 (2014).

[64] N. Zaitseva *et al.*, *Nucl. Instr. Meth. A* **668**, 88 (2012).

[65] N. P. Zaitseva *et al.*, "U.s. patent on plastic scintillator with psd," (2012).

[66] http://www.eljentechnology.com/images/stories/Data_Sheets/Plastic_Scintillators/ej299 33%20psd%20data%20sheet.pdf, "**EJ299-33 datasheet**," (2014).

[67] S. Pozzi, M. Bourne, and S. Clarke, *Nucl. Instr. Meth. A* **723**, 19 (2013).

[68] D. Cester *et al.*, *Nucl. Instr. Meth. A* **735**, 202 (2014).

[69] K. Jedrzejczak, *Pomiar strumienia neutronów w Narodowym Laboratorium Gran Sasso (in Polish)*, Ph.D. thesis, Instytut Problemów Jądrowych im. Andrzeja Sołtana (2011).

[70] S. Shalev *et al.*, *Nucl. Instr. Meth. A* **71**, 292 (1969).

[71] www.srim.org, "**Particle Interactions with Matter Calculator**," (2013).

[72] L. Boilinger and G. Thomas, *Nucl. Instr. Meth. A* **17**, 97 (1962).

[73] R. Murray, *Nucl. Instr.* **2**, 237 (1958).

[74] A. Syntfeld *et al.*, *IEEE Trans. on Nucl. Sci.* **52**, 3151 (2005).

[75] C. W. E. van Eijk *et al.*, *Nucl. Instr. Meth. A* **529**, 260 (2004).

[76] M. C. Browne *et al.*, in *23rd ESARDA Annual Meeting Symposium on Safeguards and Nuclear Material Management* (2001).

[77] S. Guizhen *et al.*, *Journ. of Non-Cryst. Solids* **80**, 594 (1986).

[78] http://www.crystals.saint-gobain.com/uploadedFiles/SG Crystals/Documents/Glass%20Scintillators.pdf, "**GS20 datasheet**," (2007).

[79] C. M. Dorenbos *et al.*, *Journ. of Luminescence* **82**, 299 (1999).

[80] P. Putaj, J. de Haas, K. Krmer, and P. Dorenbos, *IEEE Trans. on Nucl. Sci.* **57**, 1675 (2010).

[81] E. van Loef, J. Glodo, W. Higgins, and K. Shah, in *NSS-MIC Conference Record* (2004) pp. 265–268.

[82] J. Glodo *et al.*, *IEEE Trans. on Nucl. Sci.* **58**, 333 (2011).

[83] N. D. Olympia *et al.*, *Nucl. Instr. Meth. A* **714**, 121 (2013).

[84] M. Smith *et al.*, *IEEE Trans. on Nucl. Sci.* **60**, 855 (2013).

[85] C. Combes *et al.*, *Journ. of Luminescence* **82**, 299 (1999).

[86] A. Bessiere *et al.*, *Nucl. Instr. Meth. A* **537**, 242 (2005).

[87] K. Yang and P. Menge, *Nucl. Instr. Meth. A* (2014).

[88] A. Yoshikawa *et al.*, *IEEE Trans. on Nucl. Sci.* **56**, 3796 (2009).

[89] S. Kuze *et al.*, *Journ. of Solid State Chemistry* **177**, 3505 (2004).

[90] A. Yamazaki *et al.*, *Nucl. Instr. Meth. A* **652**, 435 (2011).

[91] T. Yanagida *et al.*, *Applied Phys. Express* **4**, 106401 (2011).

[92] Y. Yokota *et al.*, *Crystal Growth and Design* **11**, 4775 (2011).

[93] J. Iwanowska-Hanke *et al.*, "Flexible composite scintillator based on eu:licaf crystal grains," (2014), presentation at Symposium on Radiation Measurement and Applications (SORMA 2014) conference.

[94] T. Yanagida *et al.*, in *NSS-MIC Conference Record* (2010) pp. 182–184.

[95] S. Wakahara *et al.*, *Physica Status Solidi (C)* **9**, 2235 (2012).

[96] S. Suzuki *et al.*, *Optical Materials* **36**, 1959 (2014).

[97] J. Lakowicz, *Principles of fluorescence spectroscopy* (*Springer*, 2006).

[98] http://tukan.ncbj.gov.pl/?sLang=en, "**Tukan8k Analyzer**," (2010).

[99] M. Bertolaccini *et al.*, in *Nuclear Electronics Symposium, September 10–13, Versailles, France* (1968).

[100] M. Moszynski *et al.*, *IEEE Trans. on Nucl. Sci.* **44**, 1052 (1997).

[101] N. Hawkes *et al.*, *Nucl. Instr. Meth. A* **476**, 190 (2002).

[102] L.Swiderski *et al.*, *Rad. Meas.* **45**, 605 (2010).

[103] W. Leo, *Techniques for Nuclear and Particle Physics Experiments* (*Springer*, 1994).

[104] A. Jablonski, *Nature* **131**, 839 (1933).

[105] P. Atkins, *Chemia fizyczna (in Polish)* (*Wydawnictwa Naukowe PWN*, 2001).

[106] J. Simons, *Fotochemia i spektroskopia (in Polish)* (Wydawnictwa Naukowe PWN, 1976).

[107] L. Boilinger and G. Thomas, *Rev. Sci. Instrum* **32** (1961).

[108] O. Skeppstedt *et al.*, *Nucl. Instr. Meth. A* **421**, 531 (1999).

[109] S. Normand *et al.*, *Nucl. Instr. Meth. A* **484**, 342 (2002).

[110] M. Moszynski *et al.*, *Nucl. Instr. Meth. A* **350**, 226 (1994).

[111] M. Moszynski *et al.*, *IEEE Trans. on Nucl. Sci.* **55**, 1774 (2008).

[112] http://www.sparrowcorp.com/products/software, "**Kmax acquisition system**," (2015).

[113] T. Szczesniak, *Optimization fof Detectors for TIme-of-Flight Positron Emission Tomography*, Ph.D. thesis, National Centre for Nuclear Research (2012).

[114] P. A. Rodnyi, *Physical Processes in Inorganic Scintillators* (CRC Press, 1997).

[115] T. Szczesniak *et al.*, *IEEE Trans. on Nucl. Sci.* **53**, 1540 (2006).

[116] M. Moszynski *et al.*, *IEEE Trans. on Nucl. Sci.* **53**, 2484–2488 (2006).

[117] T. Szczesniak *et al.*, *IEEE Trans. on Nucl. Sci.* **57**, 3846 (2010).

[118] M. Moszynski *et al.*, *Nucl. Instr. Meth. A* **567**, 31 (2006).

[119] R. A. Cecil *et al.*, *Nucl. Instr. Meth. A* **161**, 439 (1979).

[120] M. Anghinolfi *et al.*, *Nucl. Instr. Meth. A* **165**, 217 (1979).

[121] V. Verbinski *et al.*, *Nucl. Instr. Meth. A* **65**, 8 (1968).

[122] J. Lee and C. Lee, *Nucl. Instr. Meth. A* **402**, 147 (1998).

[123] S. A. Pozzi *et al.*, *Nucl. Instr. Meth. A* **524**, 92 (2004).

[124] M. Gohil *et al.*, in *Proceedings of the DAE Symp. on Nucl. Phys. 56* (2011).

[125] Q. Y. Hu *et al.*, *IEEE Trans. on Nucl. Sci.* **52**, 473 (2005).

[126] A. Zimbal *et al.*, in *Proceedings of Science* (2006).

[127] M. Aspinall *et al.*, *Nucl. Instr. Meth. A* **583**, 432 (2007).

[128] A. Enqvist *et al.*, *Nucl. Instr. Meth. A* **715**, 79 (2013).

[129] L. Swiderski *et al.*, *IEEE Trans. on Nucl. Sci.* **55**, 3710 (2008).

[130] A. Nassalski *et al.*, *IEEE Trans. on Nucl. Sci.* **55**, 1069 (2008).

[131] http://www.eljentechnology.com/images/stories/Data_Sheets/Liquid_Scintillators/ej301%20data%20sheet.pdf, "**EJ301 detasheet**," (2013).

[132] http://www.crystals.saint gobain.com/Liquid_scintillators.aspx, "**BC501A datasheet**," (2014).

[133] http://www.crystals.saint gobain.com/Liquid_scintillators.aspx, "**BC501, BC501A, and BC-519 data sheet**," (2014).

[134] http://www.crystals.saint gobain.com/Liquid_scintillators.aspx, "*BC523A data sheet*," (2014).

[135] F. T. Kuchnir and F. J. Lynch, *IEEE Trans. on Nucl. Sci.* **15**, 107–113 (1968).

[136] D. Stromswold *et al.*, *Specifications for Radiation Portal Monitor Systems Revision 6.7 PIET-43741-TM-017*, Tech. Rep. (Pacific Northwest National Laboratory, Richland, Washington, 2003).

[137] "American national standard for evaluation and performance of radiation detection portal monitors for use in homeland security," .

[138] "Technical and functional specifications for border monitoring equipment," .

[139] R. Kouzes *et al.*, *Neutron Detector Gamma Insensitivity Criteria*, Tech. Rep. (Pacific Northwest National Laboratory, 2009).

[140] J. Bialkowski *et al.*, *Nucl. Instr. Meth. A* **275**, 322 (1989).

[141] M. Marseguerra *et al.*, *Progress in Nuclear Energy* **43**, 305 (2003).

[142] N. Kornilov *et al.*, *Nucl. Instr. Meth. A* **599**, 226 (2009).

[143] L. Stevanato *et al.*, *Nucl. Instr. Meth. A* **690**, 96 (2012).

[144] I. Pawelczak *et al.*, *Nucl. Instr. Meth. A* **711**, 21 (2013).

[145] D. Wolski *et al.*, *Nucl. Instr. Meth. A* **360**, 584 (1995).

[146] S. A. Pozzi *et al.*, *IEEE Trans. on Nucl. Sci.* **52**, 3141 (2005).

[147] H. P. Chou and C. Y. Horng, *Nucl. Instr. Meth. A* **328**, 522 (1993).

[148] G. H. V. Bertrand *et al.*, *Chem. Eur. J.* **20**, 1 (2014).

[149] P. Zhmurin *et al.*, *Rad. Meas.* **62**, 1 (2014).

[150] http://www.originlab.com/index.aspx?go=Products/OriginPro, "**OriginPro software webpage**," (2015).

[151] E. Sakai, *IEEE Trans. on Nucl. Sci.* **34**, 418 (1987).

[152] R. Evans and A. Noyau, *The atomic nucleus*, Vol. 787 (*McGraw-Hill*, 1955).

List of Figures

List of Tables